SCANNING TUNNELLING MICROSCOPY AND SPECTROSCOPY OF QUANTUM MATERIALS

Matthew James Neat

A Thesis Submitted for the Degree of PhD
at the
University of St Andrews

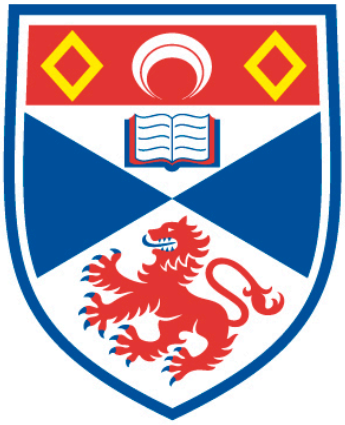

2017

Scanning Tunnelling Microscopy and Spectroscopy of Quantum Materials

Matthew James Neat

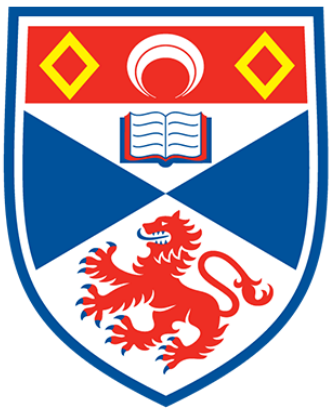

University of
St Andrews

This thesis is submitted for the degree of Doctor of Philosophy in Physics at the University of St Andrews

Submitted: 23rd November, 2017

Main Supervisor: Dr. Peter Wahl
Second Supervisor: Dr. Chris Stock

"It is the most shattering experience of a young man's life when one morning he awakes and quite reasonably says to himself, I will never play the Dane."

— Uncle Monty, *Withnail and I*

1. Candidate's declarations:

I, Matthew James Neat, hereby certify that this thesis, which is approximately 52,000 words in length, has been written by me, and that it is the record of work carried out by me, or principally by myself in collaboration with others as acknowledged, and that it has not been submitted in any previous application for a higher degree. I was admitted as a research student in September 2013 and as a candidate for the degree of Doctor of Philosophy in Physics completed by November 2017; the higher study for which this is a record was carried out in the University of St Andrews between 2014 and 2017.

Date ..... signature of candidate .....

2. Supervisor's declarations:

I hereby certify that the candidate has fulfilled the conditions of the Resolution and Regulations appropriate for the degree of Doctor of Philosophy in Physics in the University of St Andrews and that the candidate is qualified to submit this thesis in application for that degree.

Date ..... signature of supervisor .....

3. Permission for publication: (to be signed by both candidate and supervisor)

In submitting this thesis to the University of St Andrews I understand that I am giving permission for it to be made available for use in accordance with the regulations of the University Library for the time being in force, subject to any copyright vested in the work not being affected thereby. I also understand that the title and the abstract will be published, and that the title and the abstract will be published, and that a copy of the work may be made and supplied to any bona fide library or research worker, that my thesis will be electronically accessible for personal or research use unless exempt by award of an embargo as requested below, and that the library has the right to migrate my thesis into new electronic forms as required to ensure continued access to the thesis. I have obtained any third-party copyright permissions that may be required in order to allow such access and migration, or have requested the appropriate embargo below.

The following is an agreed request by candidate and supervisor regarding the publication of this thesis:

PRINTED COPY
Embargo on all of print copy for a period of 2 years on the following grounds: Publication would preclude future publication.

ELECTRONIC COPY
Embargo on all of electronic copy for a period of 2 years on the following grounds: Publication would preclude future publication.

ABSTRACT AND TITLE EMBARGOES
I do not require an embargo on the title.

Date ..... signature of candidate ..... signature of supervisor .....

Acknowledgements

I want to dedicate this thesis to my friends and family, who have helped me get through this PhD and put up with my persistent existential dread. I'd like to thank my supervisor Peter Wahl for giving me a chance when I left my original PhD project and I hope I've made it up to him with the work in this thesis. I want to thank Jean-Philippe Reid for helping me through my PhD; his coffee breaks, midweek pints and pep talks got me through this and stopped me dropping out completely right at the beginning. It means a lot.

Publications

1. **"Fermiology and superconductivity of topological surface states in $PdTe_2$"**,
   Accepted, Physical Review Letters, 2018.
   O. J. Clark, M. J. Neat, K. Okawa, L. Bawden, I. Marković, F. Mazzola, J. Feng, V. Sunko, J. M. Riley, J. Fujii, I. Vobornik, T. K. Kim, M. Hoesch, W. Meevasana, T. Sasagawa, P. Wahl, M. S. Bahramy, and P. D. C King.

2. **"Signatures of Inelastic Tunnelling in UPt_3"**,
   In Preparation, 2017.
   M. J. Neat, A. Huxley, J.-Ph. Reid, and P. Wahl.

3. **"Quasiparticle Interference from Topological Surface States in $PdTe_2$"**,
   In Preparation, 2017.
   M. J. Neat et al.

Abstract

Scanning tunnelling microscopy and spectroscopy (STM/STS) of heavy fermion materials and superconductors has enabled the high energy and momentum resolution probing of their electronic and many-body interactions. Heavy fermion superconductivity and its links to unconventional pairing mechanisms remains not fully understood; and the potential role for topology in governing the surface properties of these materials is an exciting new topic in condensed matter physics.

In this thesis I will present STM/STS investigations into four quantum materials with heavy fermion and/or superconducting properties. In UPt_3 the heavy fermion behaviour is investigated, resulting in the visualisation of the Kondo lattice. Signatures of inelastic tunnelling were seen, consistent with known phonon excitations; as well as a small gap-like structure above the Fermi level. No superconducting gap was detected at the surface of UPt_3 and quasiparticle interference (QPI) revealed light bands at the Fermi level. The spectroscopy of $PdTe_2$ is then investigated, revealing sharp peaks in conductance consistent with band extrema seen in ARPES; as well as conventional type-II BCS superconductivity. Strong QPI signatures were revealed to be consistent with scattering of quasiparticles from the topological surface states seen in ARPES, with a chiral spin texture dictating the q-space structure of the QPI imaging. The superconductivity at high magnetic field in FeSe was then investigated, revealing a two-band character gap structure with significant anisotropy. The superconducting gap persisted up to 14 T; suggesting that FeSe remains a superconductor up to even higher magnetic fields. Finally QPI measurements on SmB_6 were compared to a bulk tight binding model, which demonstrated that the surface band structure and QPI is well described by a bulk model and in particular f-states and their hybridisation. Evidence for topological properties are not obvious but in-gap conduction is seen, therefore providing some metallic surface states of some kind.

Contents

List of Figures

List of Tables

Chapter 1

Heavy Fermion Materials and Superconductivity

1.1 Superconductivity

Superconductivity was discovered by Heike Kamerlingh Onnes in 1911 in solid mercury wire, whilst investigating the low temperature resistivity of metals when they were submerged in liquid helium, which he himself had only managed to liquify for the first time a few years prior. He measured a sudden drop in resistivity to zero when the wire was taken to liquid helium temperatures around 4.2 K, and saw similar behaviour in a range of other metals. This phenomenon of zero resistivity was called superconductivity and the same materials were also observed to strongly screen magnetic fields in the Meissner effect as perfect diamagnets. Superconductors can be described as being either type-I or type-II, depending on the ratio of their magnetic penetration depths to their coherence lengths (λ/ξ). The magnetic penetration depth, λ, provides a length scale over which magnetic fields exponentially decay inside a superconductor, whilst ξ provides a characteristic size of the paired electrons. If the ratio is less than $1/\sqrt{2}$ then it is type-I and if greater, type-II. Type-I superconductors expel magnetic fields from their bulk as illustrated in the figure below, whereas type-II allow the penetration of quantised units of magnetic flux through pores of normal states in the otherwise superconducting material,

creating a structured lattice of Abrikosov vortices of supercurrent [1]. At a high enough magnetic field, superconductivity is destroyed as the Cooper pair electrons which form the superconductivity are torn apart.

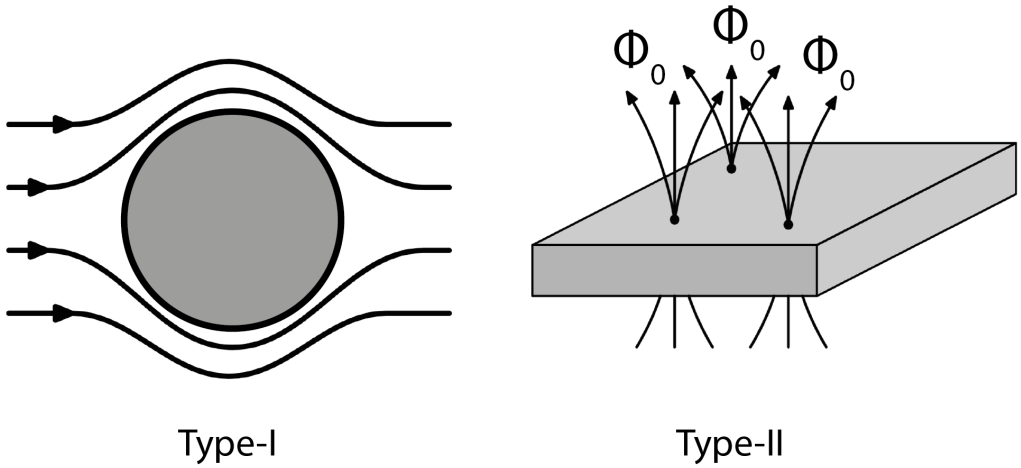

Figure 1.1: How type-I and type-II superconductors interact with external magnetic fields, with the classic Meissner effect in type-I and the Abrikosov vortices with quantised flux Φ_0 in type-II. Figures adapted from [1].

Zero electrical resistance allows the persistent flow of currents, utilised in powerful superconducting magnets that do not need a constant supply of electricity to maintain themselves due to minimal power loss. The same superconducting magnet technology is found across various industries, for example within MRI scanners and Maglev trains. Early and conventional superconductors became well described by BCS theory, proposed as its namesake would suggest by John Bardeen, Leon Neil Cooper and John Robert Schrieffer in 1957 [2]. The theory accounted for the zero resistance, magnetic screening and temperature scales associated with superconductors, which won them the Nobel Prize in physics in 1972. At the heart of BCS theory was an effective attractive interaction between electrons that is mediated by phonons, which allowed electrons to bind together into pairs, known as Cooper pairs. These electrons would pair up to have zero net-spin at the Fermi surface, allowing them to form a Bose-Einstein condensate [3]. Unfortunately, the BCS mechanism for superconductivity would only work at low temperatures, making technological use of them difficult. Later in the 1980s, a new class of superconductors called the cuprates were discovered, which were superconducting at temperatures as high

as 100 K and not well described by BCS theory. Taking inspiration from the discovery of superfluidity in ^{3}He, more complex pairing mechanisms were proposed for the newly discovered unconventional superconductors [1].

Other superconducting pairing mechanisms have since been discovered in a range of materials, such as d-wave pairing symmetry in the cuprates and suspected p-wave pairing symmetry in Sr_2RuO_4 and UPt_3, with particular reference to their Knight shift behaviour [4][5]. These pairing symmetries are called p or d-wave due to their geometric similarity to the symmetries of p and d orbitals in atomic physics, with : L = 0 (s-wave), L = 1 (p-wave) and L = 2 (d-wave). The consequences for the symmetry of their wavefunctions means that the odd-parity pairing symmetry, i.e p-wave, must have an even spin state and therefore form a spin-triplet Cooper pair, in order not to violate the Pauli exclusion principle and maintain the antisymmetry of the wave-function under electron exchange; whereas s-wave and d-wave form spin singlet pairs. p-wave superconductivity needs an order parameter that describes the three components of triplet pairing, therefore a vector order parameter, $\mathbf{d(k)}$ is used; where the magnitude of the energy gap, Δ, is then proportional to $|\mathbf{d(k)}|^2$ [6].

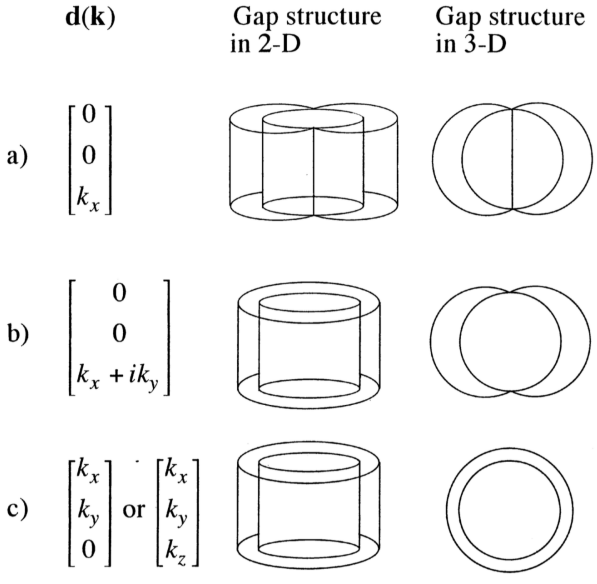

Figure 1.2: Energy gap structures for the three d-vectors listed for both 2D and 3D Fermi surfaces. There are line nodes for both cases in a), b) is fully gapped in 2D but has point nodes in 3D whereas c) is fully gapped in both cases. d-vectors b) and c) correspond to the A and B phases of superfluid He-3. Figure taken from [6].

Whilst d-wave superconductivity is well established, p-wave superconductivity has not yet been unambiguously pinned down. Probes for p-wave superconductivity need to be sensitive to either the odd-parity component or the spin-triplet character; and most experimental studies have focussed on the spin-triplet nature, like Knight shift experiments [6]. Superconducting gap structures as probed in Scanning Tunnelling Spectroscopy (STS) will reflect the presence of nodes, however noded superconductivity is present across many pairing symmetries and is therefore not enough to verify whether a superconductor has a particular order parameter. However topological consequences of p-wave order parameters, such as half-quantum vortices and Majorana fermions (discussed briefly in the UPt_3 chapter) do have signatures accessible in STS. In addition to unconventional pairing symmetries, superconductivity has been found to live in coexistence with ferromagnetic and antiferromagnetic order, being counter-intuitive with singlet s-wave pairing.

A huge triumph for condensed matter physics would be the discovery and manipulation of the process behind unconventional superconductivity, for technological applications. If superconductors were able to be used at room temperature, great leaps in technology such as lossless power transmission, powerful quantum computers and magnetically levitating trains would become cheaper and more widespread. As things stand, not many materials superconduct above liquid nitrogen temperatures; the first high-temperature superconductor discovered being $YBa_2Cu_3O_{7-\delta}$ with a T_C of 92 K [1], which Knight shift [7][8] and Josephson tunnelling measurements [9] suggested spin-singlet d-wave behaviour rather than p-wave.

1.2 Heavy Fermion Behaviour

Heavy fermion behaviour is ascribed to materials that have particularly high specific heat coefficients, typically greater than 400 mJ/mole K^2 and behave as if their electrons have a much greater mass than free electrons [10], hence the name heavy fermion. At the heart of heavy fermion compounds is Kondo physics, that is the screening of magnetic moments by conduction electrons. In the simple Kondo effect picture, a magnetic impu-

rity site with spin one-half is screened by conduction electrons with anti-parallel spin in an attempt to produce an overall non-magnetic state [11][12]. The extension is then is to what is known as a Kondo lattice, where each atomic site acts as a magnetic impurity. Something emulated well by atomic species with unpaired electrons in their f-shells such as actinides and rare-earth metals, which provide highly localised magnetic moments for the conduction electrons to interact with. Heavy fermion systems are strongly correlated, with large specific heat coefficients, large low-temperature magnetic susceptibility, low-temperature resistivity rises and unusual temperature dependences of the specific heat [13]. These Kondo systems can be described in a simple model where the conduction electrons are exchange coupled to localised spins on lattice sites, tuned by the exchange coupling, J, in what is known as the Kondo necklace model proposed by S. Doniach [14][15]. This Kondo necklace model is a logical progression of the simple Kondo effect of dilute magnetic impurities; where a dense lattice of these Kondo spin-sites can describe the magnetic and transport properties of heavy fermion compounds [16][17]. The Hamiltonian in Doniach's model is essentially an xy-model of nearest-neighbour spin-site interactions on a lattice via an exchange interaction of the form [18]:

$$H = J\sum_i \mathbf{S}_i \cdot \tau_i + W\sum_i (\tau_i^x \tau_{i+1}^x + \tau_i^y \tau_{i+1}^y), \tag{1.1}$$

where S_i are the Kondo-site spins, τ_i, the conduction electron spins and W representing the binding energies of the magnetic states with:

$$W_K \sim \frac{1}{N(0)} e^{-1/N(0)J}, \tag{1.2}$$

for the Kondo singlet solution, which is where the conduction electrons completely screen the magnetic spin, with N(0) the Fermi level density of states; and:

$$W_{AFM} \sim CJ^2 N(0), \tag{1.3}$$

for the Ruderman-Kittel-Kasuya-Yosida (RKKY) antiferromagnetic state, where C is a

scaling constant.

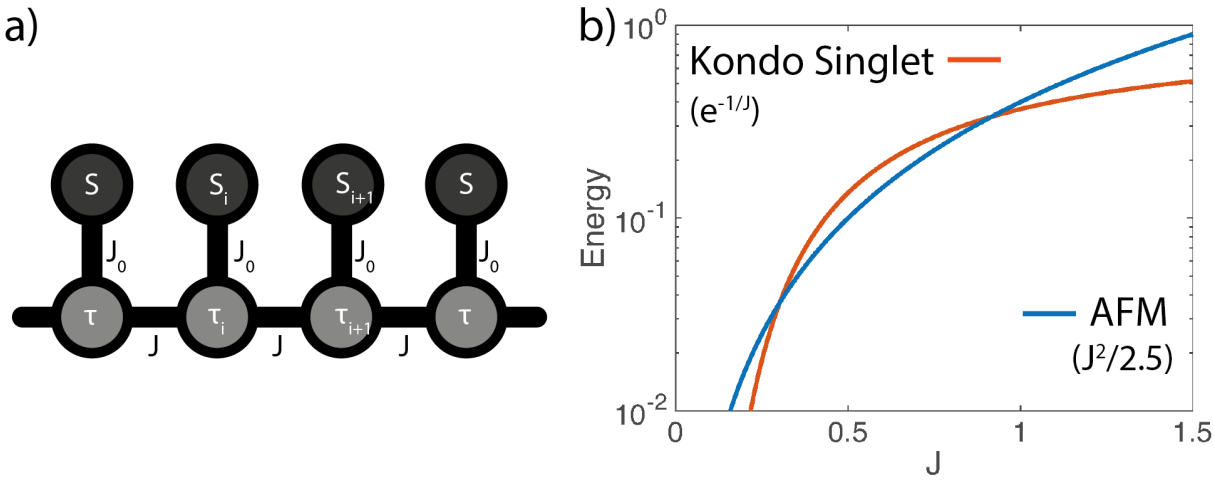

Figure 1.3: a) Schematic of the Kondo necklace model, with itinerant conduction electron sites in light grey, with spins τ, coupled to each other with the exchange interaction parameter J and lattice spin sites in black with spins S, coupled only to conduction electrons on the same site. Figure adapted from [19]. b) Effective phase diagram of the Kondo necklace model. Figures adapted from [14].

The model predicts that when the Kondo screening is stronger, i.e. that the Kondo temperature scale is greater, the system produces a Kondo singlet state; however when the Kondo screening is weaker, the system should form an antiferromagnetic ground state. The Kondo screening energy scale, often described as a temperature T_K, depends on the exchange interaction strength which then ultimately determines the ground state magnetic properties. This Kondo lattice model was very successful at describing the behaviour of many Ce-based compounds, such as the non-superconducting compounds $CeRu_2Si_2$ and $CeCu_6$, as well as the multi-gapped superconductor $CeCu_2Si_2$ [20][21]. The same Kondo physics developed by S. Doniach was able to also describe the asymmetry and line shapes of X-ray spectra and Kα lines in the photoemission of metals, due to the many electron interactions of the conduction electrons with the final deep hole state, showing Kondo-like behaviour [22]. AFM order has been observed in the heavy fermion superconductor, UPt_3 for example below 5 K [23], whereas other heavy fermion systems studied in this thesis, such as SmB_6 do not [24]. The Kondo-lattice produces a hybridisation effect between the delocalised conduction electrons and the localised spin-sites that produces a gap in the density of states, known as the hybridisation gap; which at low

temperatures can produce a metal to insulator transition if the Fermi level lies within this hybridisation gap in a half-filled single band material [17].

Heavy fermion materials have a characteristic spectroscopic line-shape, first described by U. Fano, which can apply to many systems in science and engineering unrelated to condensed matter physics. The Fano line shape, or Fano resonance, is so ubiquitous due to the fact that it originates from the interference of two scattering amplitudes; one which is wave-like from a bath of continuum states and the other from a localised discrete state. This was originally explained by U. Fano, who set out to describe the asymmetric behaviour of the $2s2p^1P$ resonance found in inelastic electron scattering of He [25]. For heavy fermion materials, it is the interference of scattering amplitudes from the continuum-like conduction band and the more localised magnetic states. The Fano line-shape has been measured in STS on many heavy fermion compounds, where spectra look similar to simple dilute Kondo impurities on material surfaces [26]. These resonances are often asymmetric because of the preferential coupling of one channel instead of the other [27]. Mathematically, this resonance has a simple form:

$$\sigma = \sigma_a \frac{(q+\epsilon)^2}{(1+\epsilon^2)}, \tag{1.4}$$

where σ_a is an amplitude term, q the Fano parameter and ϵ a dimensionless energy term, defined as:

$$\epsilon = \frac{(E - E_r)}{\Gamma}. \tag{1.5}$$

Here, E is energy, E_r the resonant energy of the system and Γ the half-width of the resonance [27]. It is wise to also normalise this functional form and move away from scattering cross-section notation (sigmas) to a generic form of:

$$f(\omega) = \frac{A}{(1+q)^2} \frac{(\omega - \omega_0 + q\Gamma)^2}{(\Gamma^2 + (\omega - \omega_0)^2)}, \tag{1.6}$$

where ω takes the place of energy. The Fano parameter q is interpreted as a ratio of the two amplitudes of the coupled discrete and continuum states. One channel is the direct tunnelling to the localised state and the other is tunnelling to the conduction band continuum and then into the localised state [27]. ω_0 is the energy of the many-body state and A is a scaling amplitude.

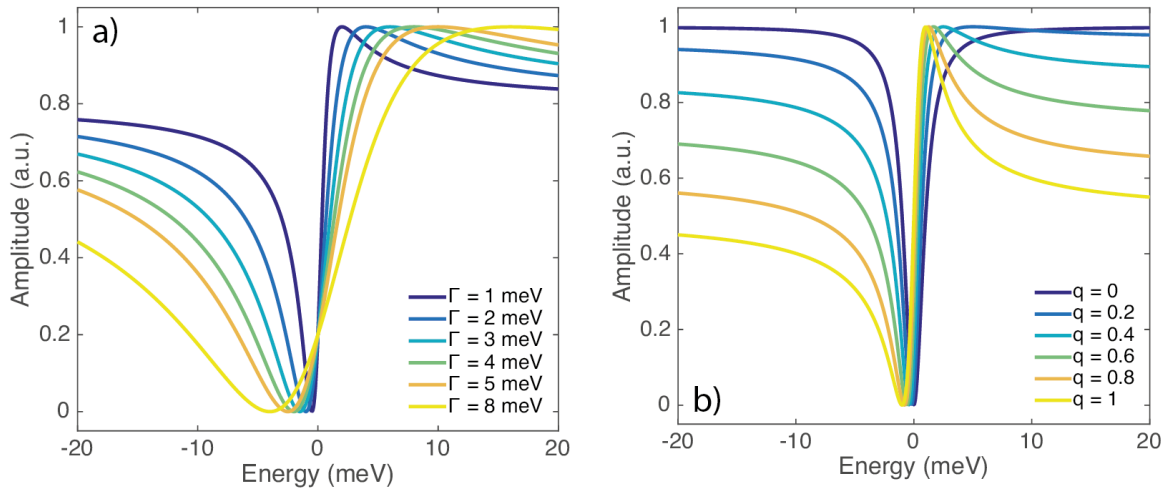

Figure 1.4: a) Figure demonstrating the effect of changing the Fano energy width, with a constant q = 0.5 and $\omega_0 = 0$. b) Figure demonstrating the effect of changing the asymmetry parameter q, with constant energy width $\Gamma = 1$ meV and $\omega_0 = 0$.

The functional form of the asymmetry parameter q is expressed in terms of the Green's functions describing the unperturbed conduction electrons, where q is simply the real part of this Green's function divided by the imaginary part [28]; which for many systems will produce negative q values that simply flip around the Fano resonance shape, since the formulation will then depend on where the impurity Kondo state sits with respect to the conduction band. The Fano asymmetry has been formulated in other theoretical works to be of the form [29]:

$$q = \frac{t_2}{\pi \rho_0 V t_1} + \Lambda(\epsilon), \tag{1.7}$$

where t_1 and t_2 are the matrix elements for tunnelling into the bulk states and Kondo resonance respectively and Λ is slowly varying function that accounts for admixing of the continuum states. The asymmetry is also inversely proportional to the density of states

at the Fermi level (ρ_0) and the hybridisation strength, V [29]. The Fano width itself, Γ, is proportional to the hybridisation strength and Fermi level density of states [30], therefore would be expected to vary with the atomic lattice.

Chapter 2

Scanning Tunnelling Microscopy and Spectroscopy

2.1 Introduction

Scanning Tunnelling Microscopy (STM) was first developed by Gerd Binnig and Heinrich Rohrer at IBM in 1981 [31], as a new microscopy technique that had groundbreaking spatial resolution which allowed the visualisation of the atoms on the surface of a material. They later won the Nobel Prize in Physics in 1986 for the technique that soon allowed the probing of surface electronic states with atomic resolution. Fundamentally, Scanning Tunnelling Microscopy works by utilising the phenomenon of the quantum tunnelling of electrons across the vacuum gap, from the surface of a material to a metallic needle, or tip as it is often referred to, whilst it is held within angstroms of a surface. The tunnelling electrons produce a very small electrical current, which scales exponentially with the tip-sample separation. The exponential displacement sensitivity gives STM the resolution necessary to resolve atomic corrugations when the tip is rastered across the material to produce a topographic image. Scanning tunnelling microscopes need to be vibrationally isolated from the environment in order to be stable enough to probe the surface electron density for both topographic imaging and spectroscopy.

2.2 Theory

2.2.1 Quantum Tunnelling (Square Potential Barrier)

The simple model of quantum tunnelling through a square-potential barrier can be used to demonstrate the principal behind STM by starting with the one-dimensional time-independent Schrödinger equation:

$$\frac{-\hbar^2}{2m}\frac{\partial^2\psi(x)}{\partial x^2} + V(x)\psi(x) = E\psi(x), \tag{2.1}$$

where $\psi(x)$ is the electron wave function; m the mass of the electron; $V(x)$ the square potential barrier and E the kinetic energy of the electron. A top hat potential barrier of width b and height V_0 and zero everywhere else is then used, drawn in the figure below:

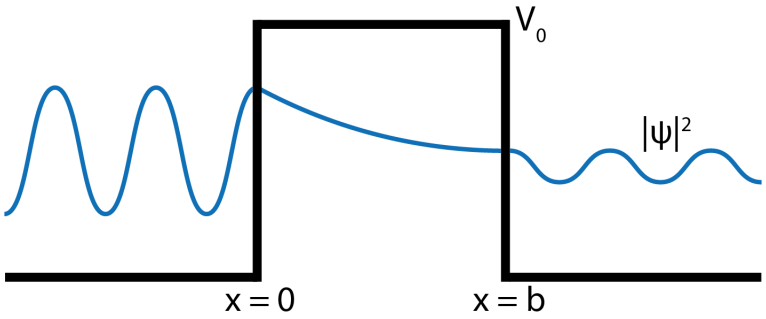

Figure 2.1: Diagram of the square potential barrier and the amplitude of the wave-function throughout the system.

The transmission ratio of electrons tunnelling through the barrier, T, can be calculated as:

$$T = \frac{\text{Transmitted electron flux}}{\text{Incident electron flux}}, \tag{2.2}$$

For a wide barrier, i.e. $e^{-2|k_1|b} << 1$, the transmission ratio, or tunnelling probability of a particle through the barrier, can be approximated as [32]:

$$T \approx \left(\frac{16E(V_0 - E)}{V_0^2}\right)e^{-2|k_1|b}. \tag{2.3}$$

From this expression it can be seen that the tunnelling probability scales exponentially with the width of the barrier (which will be the tip-sample separation), in addition to kinetic energy and barrier height. The square-potential barrier model is however not enough to describe the full energy dependence of the tunnelling current, but it does identify the displacement sensitivity of Scanning Tunnelling Microscopy. The tunnelling electrons will produce a small electrical current, which can be measured to infer the tip-sample separation and map out the topography of the sample surface. When operating an STM there two basic modes of operation: the first mode, called constant height mode, is where the tip is held at a constant height above the surface and the tip is rastered laterally with a bias, V_s, applied between the tip and sample. The current is measured as it is rastered to produce a map of the tunnelling current. The second mode of operation, called constant current mode, is where a constant tunnelling current, I_s, is maintained through a feedback mechanism, where the height of the tip is automatically adjusted as it is rastered across the surface. The changes in the tip height, achieved by piezo-actuators, are recorded to produce a topographic map of the surface. The constant height mode is the quickest mode of operation since the feedback controls which maintain a constant current in the other mode take time to adjust, however it is only suitable for very flat surfaces due to the much greater risk of crashing.

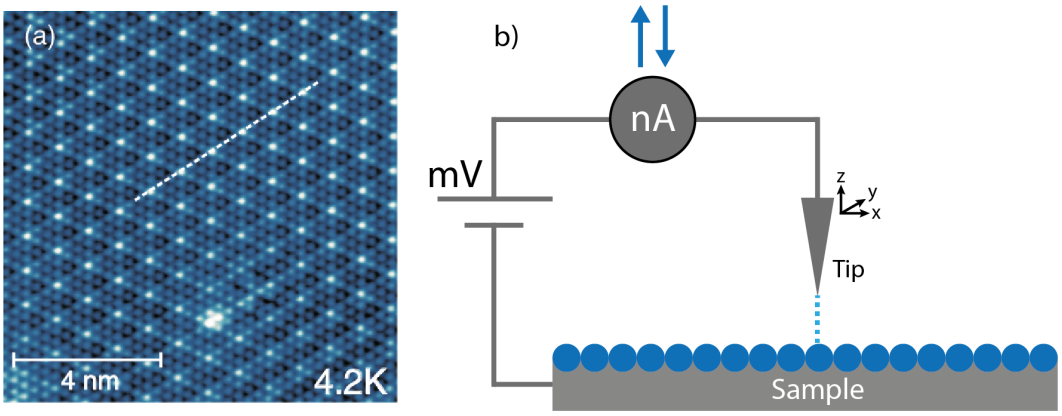

Figure 2.2: a) STM topograph of $NbSe_2$ measured at T = 4.2 K; using V_s = 100 mV, I_s = 0.5 nA, taken from [33]. Surface atomic corrugation of $NbSe_2$ and its charge density wave are visible as modulations in surface electron density. b) Schematic of a typical STM.

2.2.2 Scanning Tunneling Spectroscopy (STS)

The tunnelling current in STM not only has a strong spatial dependence, but also a very useful energy dependence; where the current depends on the available states in the tip and the sample. The tunnelling current can be described initially by Fermi's golden rule which gives a transition rate, T, as:

$$T_{i\to f} = \frac{2\pi}{\hbar} |\langle f| H |i\rangle|^2 \rho_f, \tag{2.4}$$

where i and f represent initial and final states; ρ_f the density of states in the final state and a Hamiltonian, H, to change the system from one state to the other. With further treatment in work by J. Bardeen within a many-particle model, it was then used to explain planar tunnelling junctions [34]. The theory was then expanded by J. Tersoff and D.R. Hamann [35] to describe STM/STS to reveal the connection to the local density of states and the tunnelling current in the Tersoff-Hamann model [35][36]. For an elastic tunnelling process, the net electron current is expressed as forward tunnelling minus any backward tunnelling [36]:

$$I = I_{t\to s} - I_{s\to t}, \tag{2.5}$$

$$I = \frac{4\pi e}{\hbar} \int_{-\infty}^{+\infty} |M|^2 \rho_s(E_s)\rho_t(E_t)\{f(E_t,T)[1-f(E_s,T)] - f(E_S,T)[1-f(E_t,T)]\} d\epsilon, \tag{2.6}$$

where M is the matrix element describing the quantum tunnelling process and includes the spatial dependence; ρ_i, the density of states of the tip and the sample accordingly and the Fermi distribution, $f(E_i, T)$. The tip and the sample are held at different energies by applying a bias voltage, V, across them. Taking this into account, the equation becomes:

$$I = \frac{4\pi e}{\hbar} \int_{-\infty}^{+\infty} |M|^2 \rho_s(\epsilon)\rho_t(\epsilon + eV)[f(\epsilon,T) - f(\epsilon + eV)] d\epsilon. \tag{2.7}$$

The tips used in STM are chosen as to have a flat density of states in order to not interfere with spectroscopy. The tip in the mK STM used in this thesis is made from a Pt-Ir alloy. Assuming that the density of states of the tip is perfectly flat, i.e. $\rho_t(E_t) = \rho_t(0)$; as well as assuming energy independent matrix elements; equation (2.7) can be reduced to:

$$I = \frac{4\pi e|M|^2\rho_t(0)}{\hbar}\int_{-\infty}^{+\infty}\rho_s(\epsilon)[f(\epsilon,T) - f(\epsilon+eV)]d\epsilon. \tag{2.8}$$

In the zero-temperature limit, a suitable approximation for the mK temperatures used in this thesis; the Fermi distributions become step functions, being only non-zero in the range from zero to eV. Further simplifying to:

$$I = \frac{4\pi e|M|^2\rho_t(0)}{\hbar}\int_{0}^{eV}\rho_s(\epsilon)d\epsilon. \tag{2.9}$$

The STM tunnelling current is proportional to the integrated local density of states (IDOS) and to measure the local density of states directly, the derivative of the current, the differential conductance G, is measured which is proportional to the local density of states (LDOS):

$$G = \frac{dI}{dV} \propto \rho_s(\epsilon). \tag{2.10}$$

The differential conductance is measured directly using an AC lock-in amplifier by applying a modulation signal on top of the DC bias, expressed mathematically as a two-term Taylor expansion [37]:

$$I(V + V_L\sin(wt)) \approx I(V) + \frac{dI}{dV}|_V.V_L\sin(\omega t), \tag{2.11}$$

where ω is the modulation frequency and V_L is the AC modulation amplitude. The differential conductance signal is then easily extracted from the modulated output signal by knowing the reference modulation signal and the DC I(V) output.

Superconductors

For a BCS superconductor, the energy dispersion, $E_{\mathbf{k}}$, is expressed as [1]:

$$E_{\mathbf{k}} = \sqrt{(\xi_{\mathbf{k}} - \epsilon_F)^2 + |\Delta|^2}, \tag{2.12}$$

where $\xi_{\mathbf{k}}$ is the energy of the electrons; ϵ_F the Fermi energy and Δ the superconducting gap. This produces a density of states in energy ($E = \xi - \epsilon_F$) of the form:

$$\frac{N(E)}{N(0)} = \frac{E}{\sqrt{E^2 - |\Delta|^2}}, \tag{2.13}$$

where $N(0)$ is the density of states of the normal state. The density of states produces an energy gap with no states within $\pm\ \Delta$, with sharp coherence peaks at the edges.

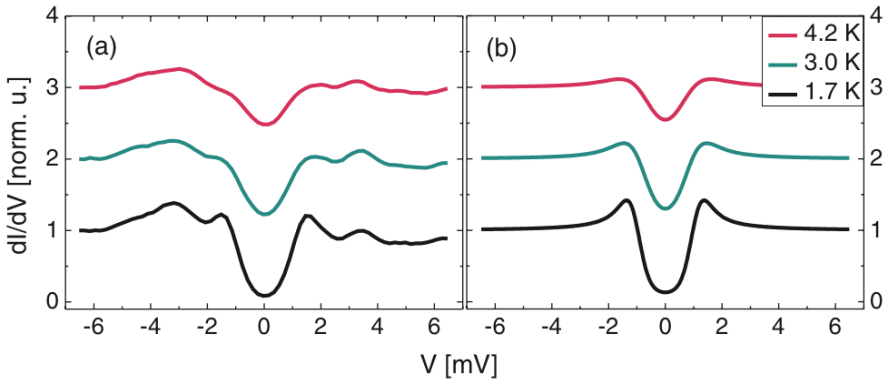

Figure 2.3: a) measured and b) simulated spectra of superconducting $NbSe_2$ at various temperatures. Figures taken from [33].

Figure 2.3 above shows an example of STS measurements on the superconductor $NbSe_2$ [33]. The energy gap and coherence peaks are clearly observed, albeit with some thermal and quasiparticle broadening.

2.2.3 Scattering and Broadening

Following from the equation for the tunnelling current in the zero-temperature limit, the finite-temperature tunnelling current can be expressed by the following equation:

$$I(V) \propto \int_{-\infty}^{\infty} \rho_s(E)\rho_t(0)\left[f_s(E,T) - f_t(E+eV,T)\right] dE. \tag{2.14}$$

Where f_s and f_t represent the Fermi distributions for both the sample and the tip. At non-zero temperature, these functions account for the thermal broadening of the bias-dependent tunnelling current. In addition, where an AC lock-in amplifier is used to measure this tunnelling current, the AC method introduces its own broadening as a convolution over a semicircle, expressed as:

$$\frac{dI}{dV}(V)_{fit} = \int_{-\sqrt{2}V_L}^{+\sqrt{2}V_L} dE \frac{dI}{dV}(V+E)\sqrt{2V_L^2 - E^2}, \tag{2.15}$$

where V_L is the lock-in modulation amplitude. Another source of broadening of spectroscopic features is due to scattering of quasiparticle electrons in the sample with finite lifetimes, which is commonly used in descriptions of superconductivity spectroscopy and fitted with the Dynes function [38]:

$$\frac{N(E)}{N(0)} = \left| \mathrm{Re}\left\{ \frac{(E - i\Gamma)}{\sqrt{(E-i\Gamma)^2 - \Delta^2}} \right\} \right|, \tag{2.16}$$

where Γ is the Dynes broadening parameter, expressed as an energy scale.

2.2.4 Inelastic Tunnelling

In STS, when the sample material has a strong vibrational response, the tunnelling process can excite vibrational modes resulting in inelastic tunnelling. When the bias voltage coincides with the energy of the vibrational excitation, a kink appears in the differential conductance due to an extra tunnelling channel opening up in the current; which then

manifests itself as a peak in the derivative of the differential conductance [36]. Inelastic tunnelling has proven a great tool for probing surface adsorbates, such as organic molecules on metallic surfaces. It was first used to identify carbon monoxide and oxygen molecule adsorbates on an Ag(110) surface through their vibrational modes in work by J. R. Hahn et al [39]. Later demonstrated in work by P. Wahl et al, where the sharp and symmetric telltale steps in conductance were present in STS of CO molecules on a Cu(100) surface, attributed to the vibrational excitations in CO on the order of 50 mV [40]; symmetric steps which are of particular importance later in this thesis. Similarly, inelastic tunnelling via bosonic spin fluctuations, such as in LiFeAs, can provide an explanation for the classic dip-hump features present in LiFeAs and other high temperature superconductors [41].

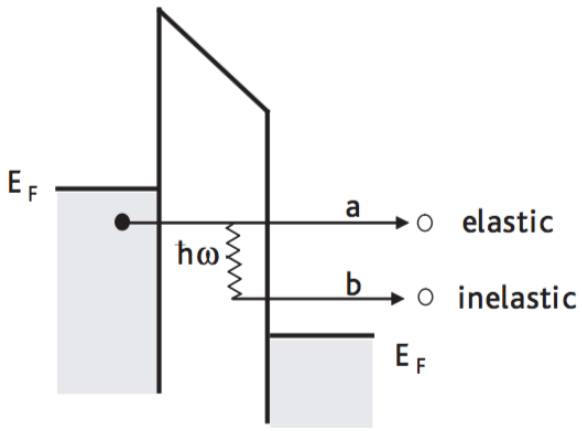

(a) Energy diagram for inelastic tunnelling.

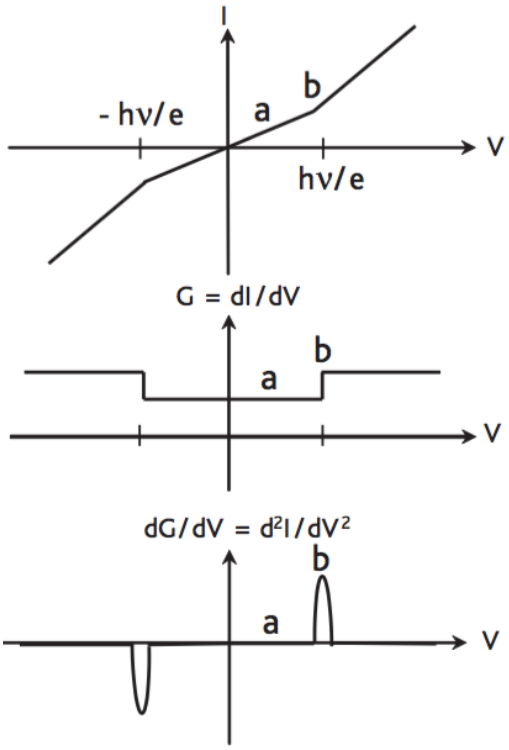

(b) Inelastic tunnelling in STS.

Figure 2.4: Energy and spectroscopic diagrams of inelastic tunnelling effects, taken from [42]. In a) the Fermi energy of the tip (right) is pushed down with the application of a bias voltage, relative to that of the sample (left); when the bias voltage is large enough such that the width is greater than that of the vibrational mode (frequency ω), a new inelastic tunnelling opens up [36]. b) represents the effects of inelastic tunnelling in the tunnelling current and its derivatives, by adding a new conduction channel that kicks in at $\hbar\omega$.

The effect of finite temperature on the width of the inelastic features can be estimated by assuming that both electrodes behave as a normal metal and convoluting the two electrodes' Fermi functions, to produce:

$$\frac{d^2I}{dV^2} \propto e^x \frac{(x-2)e^x + x + 2}{(e^x - 1)^3}, \tag{2.17}$$

where x is defined as:

$$x = \frac{eV - \hbar\omega}{k_B T}. \tag{2.18}$$

Which leads to a thermal broadening line width at half-maximum in the derivative of the differential conductance of [36]:

$$\Delta(eV - \hbar\omega) \simeq 5.4 k_B T. \tag{2.19}$$

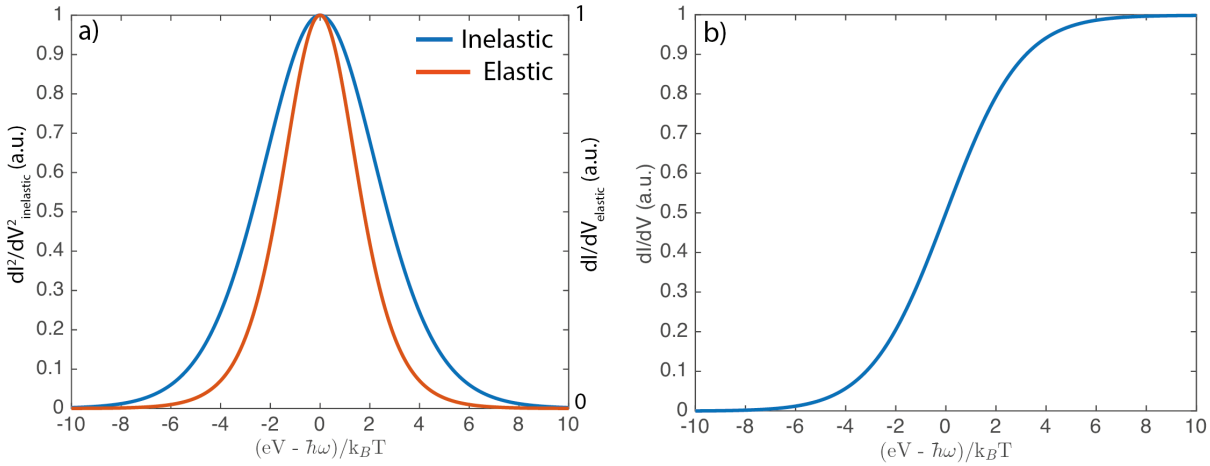

Figure 2.5: Figures showing the effects of thermal broadening on the inelastic tunnelling spectra of a simple system with a vibrating mode of frequency ω at temperature T [36]. The thermal broadening in the second derivative of the inelastic tunnelling current is comparable to the first derivative of the Fermi function in the elastic tunnelling current.

The thermal broadening from inelastic tunnelling is much greater than that from elastic tunnelling, which has a broadening of the order $\simeq 3.53\ k_B T$. So at a given temperature, inelastic features will appear disproportionately broadening compared to background elastic phenomena.

2.3 Quasiparticle Interference

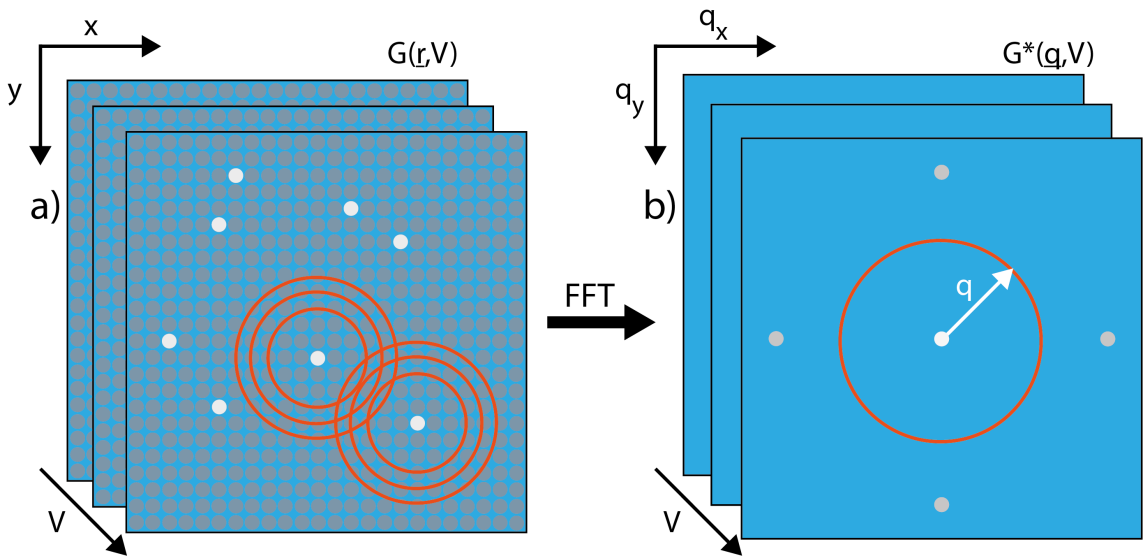

Figure 2.6: Schematic diagram of quasiparticle interference (QPI), with the atomic lattice in grey, defects in white and density of state modulations in orange.

Quasiparticle interference (QPI) is a phenomenon that occurs when electron quasiparticles elastically scatter off each other and off defects, to produce modulations in the local density of states (LDOS). Quasiparticles whose momenta and energy are governed by the underlying band structure, scatter with a scattering vector length that is given by:

$$\overrightarrow{q} = \overrightarrow{k_2} - \overrightarrow{k_1}, \tag{2.20}$$

provided that spin is conserved in the scattering process. The scattering of these quasiparticle states form a standing wave of electron-quasiparticle density with a wavelength of $\lambda = 2\pi/\mathrm{q}$, which produces enhanced density of states at the maxima of these standing waves which is measured as enhanced conductance in STS. Taking the Fourier transform of these modulations produces a q-space structure which reflects the scattering vectors, with intensities governed largely by the density of states at the initial and final k-space state. For an ordinary metal, the scattering, in a similar vein as tunnelling currents, follows a time-independent Fermi's golden rule-like form [43]:

$$A_{i-f} \propto \frac{2\pi}{\hbar}|V(q)|^2 n_i(E_i, k_i) n_f(E_f, k_f), \tag{2.21}$$

where A is the q-space scattering amplitude, V(q) the q-space scattering potential and n_i and n_f the initial and final state density of states respectively. Since in STS the surface modulations are recorded at each bias voltage, the combination of q-space and bias provides momentum and energy space information about the material, with resolution in both that far surpasses conventional ARPES techniques. QPI was famously applied to the cuprate superconductors, such as seminal work by J.E Hoffman and K. McElroy et al on $Bi_2Sr_2CaCu_2O_{8+\delta}$ [44][45] to explain the incommensurate conductance modulations and phenomena in the cuprates. QPI measurements can be compared with Angular Resolved Photoemission Spectroscopy (ARPES) measurements by recognising that to first approximation, STM measures tunnelling current as the real-space single particle spectral function, $A(\overrightarrow{r}, \omega)$, also known as the Local Density of States (LDOS); whilst ARPES measures the momentum space version of this, $A(\overrightarrow{k}, \omega)$ [46]. Quasiparticle interference is sometimes known as the Joint Density of States (JDOS) and reveals itself as scattering between local densities of states, mathematically expressed as the autocorrelation of the momentum-space spectral function as [46]:

$$JDOS(\overrightarrow{q}, \omega) = \int A(\overrightarrow{k} + \overrightarrow{q}, \omega) A(\overrightarrow{k}, \omega) d^2k. \tag{2.22}$$

It follows that the Fourier transform of the spectroscopic maps measured in STM/QPI are then comparable to the autocorrelation of ARPES data; demonstrated successfully in the QPI and ARPES investigations of $Bi_2Sr_2CaCu_2O_{8+\delta}$ [46][47][48][49].

Chapter 3

Instrumentation

3.1 Vibration Isolation

3.1.1 Introduction

Scanning Tunnelling Microscopy is vulnerable to vibrations, in particular those in the sub-100 Hz regime. Therefore vibration isolation is crucial to the operation of an STM to achieve atomic resolution. Typical topographical corrugation amplitudes for STM images are of the order of 10 pm; therefore vibrations must be contained to within 1 pm or lower to successfully visualise this corrugation [36]. A simple model for considering the vibrations that can affect STM and the attenuation of which, is that of a damped simple harmonic oscillator; and for a convenient example: a mass hanging from a spring [36]. The following derivation is adapted from C. J. Chen [36]: a mass, M, hanging from a spring of stiffness, k, that is itself attached to a frame, experiences a restoring force to its displacement of the form:

$$F_1 = -k(x - X), \tag{3.1}$$

where x is the displacement of the mass and X is the displacement of the frame. This system also experiences a damping force of the form:

$$F_2 = -c(\dot{x} - \dot{X}), \tag{3.2}$$

where c is a proportionality constant for the damping force. Newton's equation for this one-dimensional model is thus:

$$F_T = F_1 + F_2 = M\ddot{x}, \tag{3.3}$$

neglecting the acceleration of the frame, which is a reasonable assumption considering that the frame is effectively the laboratory, which is far heavier than the STM.

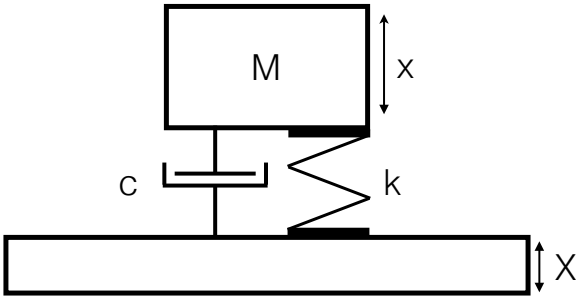

Figure 3.1: Schematic diagram of a single stage vibration isolation system, with spring stiffness k and damping term c.

By introducing a damping coefficient, γ, defined as:

$$\gamma = \frac{c}{2M}, \tag{3.4}$$

and an expression for the natural frequency, ω_0, as:

$$\omega_0 = 2\pi f_0 = \sqrt{\frac{k}{M}}; \tag{3.5}$$

Newton's equations for the system are reduced to:

$$\ddot{x} + 2\gamma\dot{x} + \omega^2 x = f(t) = 2\gamma\dot{X} + \omega^2 X, \tag{3.6}$$

where $f(t)$ represents the force transmitted from the frame to the mass. In the case where there is no force transmitted to the mass, i.e. that $f(t) = 0$, the general solution is that of damped harmonic oscillation of the form:

$$x(t) = Ae^{-\gamma t}\cos(\omega_d t + \phi), \tag{3.7}$$

where ϕ is some arbitrary phase and ω_d, is the true oscillation frequency of the mass, which is defined as:

$$\omega_d = \sqrt{\omega_0^2 - \gamma^2}. \tag{3.8}$$

It can be noted in the case where the damping coefficient matches the natural frequency of the system, the mass undergoes critically damped motion, where after displacement, the system will exponentially decay to rest without oscillation; the perfect damping. And for situations where the damping coefficient is greater than the natural frequency of the system, the damping is so great that the mass simply creeps back to its equilibrium position after disturbance. One can quantify a dimensionless number to describe the 'quality' of an oscillator, which loosely gives the number of oscillations an oscillator will experience before coming to rest, which is common across many engineering disciplines, and defined as:

$$Q \equiv \frac{\omega_0}{2\gamma}. \tag{3.9}$$

The general solution for an external force applied to an oscillator is a superposition of the earlier Newton's equation and the response of the system:

$$x(t) = \frac{1}{\omega_d}\int_0^t f(\tau)e^{-\gamma(t-\tau)}\sin[\omega_d(t-\tau)]d\tau. \tag{3.10}$$

For a sinusoidal vibration of the frame with frequency ω, the response of the mass will also be a sinusoidal vibration, which behaves according to the response function:

$$\frac{x_0}{X_0} = \frac{\omega_0^2 + 2i\gamma\omega}{\omega_0^2 - \omega^2 + 2i\gamma\omega}. \tag{3.11}$$

The ratio of amplitudes of the frame and the mass is known as the transfer function, which is given by the modulus of the response function above:

$$K(\omega) = \left|\frac{x_0}{X_0}\right| = \sqrt{\frac{\omega_0^4 + 4\gamma^2\omega^2}{(\omega_0^2 - \omega^2)^2 + 4\gamma^2\omega^2}}. \tag{3.12}$$

This transfer function can be related to decibels, a unit more commonly used in engineering as opposed to physics by [36]:

$$Z = 20\log_{10} K(\omega)(dB). \tag{3.13}$$

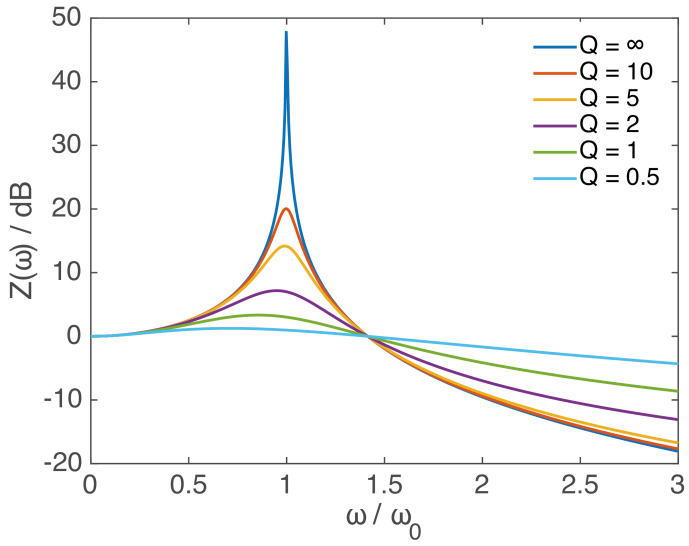

Figure 3.2: Resonance curves of a 1D damped harmonic oscillator as a function of driving frequency at various Q-factors, expressed in decibels.

It can be noted from equation 3.12 and figure 3.2 that higher damping reduces the amplitude of resonance effects, but is however relatively poor at reducing high-frequency oscillations. Therefore when considering vibration isolation, one has to compromise between these two effects, and a typical compromise is one of $Q = 3 - 10$ [36]. It is clear however, that reducing the natural frequency of the system will help the most to reduce

vibrational effects, which can be achieved by increasing the mass of the system (for example performing experiment on a concrete block), and choosing a smaller spring-stiffness coefficient. To reduce the noise transferred to the STM tip itself, the STM unit must be attached to the system as rigidly as possible, in order to give the STM unit a high resonant frequency. In a similar model, the transfer function between the STM unit and the vibration isolation system obeys the relationship:

$$K(f) = \left(\frac{f_I}{f_S}\right)^2, \tag{3.14}$$

where f_I is the resonant frequency of the vibration-isolation system and f_S is the resonant frequency of the STM unit [36]. Typical pneumatic vibration isolation systems have natural frequencies in the 1-2 Hz regime, which for a rigid STM head with, for example a 1 kHz resonant frequency, would provide a transfer function value of $\simeq 10^{-6}$ between the STM head and isolation system. Additional vibration isolation can be achieved by adding a second stage the system. A second set of springs, with a damping mechanism, can improve performance. In general, the efficiency of two-stage systems is greater than that of a single stage system; however a second system inherently has a second resonant frequency and considerations must be made to whether the extra design complication is worth the minor performance enhancement.

3.1.2 Ultra-Low Vibration Laboratory

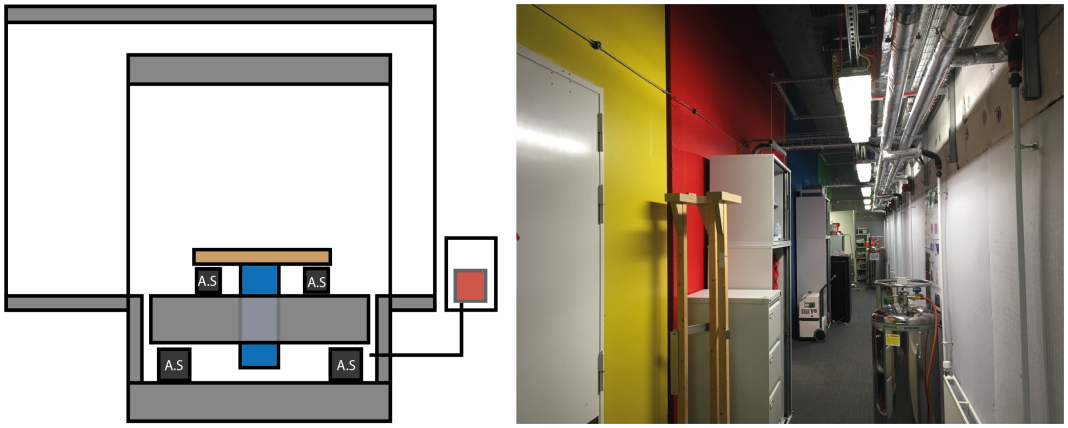

Figure 3.3: a) Schematic cross-section of the Ultra-Low Vibration (ULV) Laboratory measurement boxes with the air springs labelled A. S, the cryostat containing the STM in blue and the pumps represented in red. b) Photograph inside the ULV corridor showing the four individually isolated measurement rooms.

The room within which the STM is operated, is double-walled from the outside environment with acoustic insulation to reduce the effect of outside noise. The STM itself, which is contained within an Oxford Instruments Dilution Refrigerator, is vibrationally isolated from the environment with a two-stage system. The cryostat itself is attached to a lead-filled table fitted with three Newport I-2000 air-springs; and the table itself sits upon a concrete block supported by four Bilz air-springs. As discussed previously, this two-stage system coupled with a rigidly attached STM head minimises the external vibrational noise reaching the STM tip to maximise image quality. The building when designed was specified to the architectural VC-M standard of vibration levels less than 10 nms^{-1} in third-octave intervals above 8 Hz. Acoustically, the laboratory in continuous operation is designed to have sound pressure levels below 40 dB in third-octave bands at 31.5 Hz and higher, with rare events not exceeding 50 dB (a maximum of 1%). The measurement rooms themselves are specified to provide acoustic attenuation of 40 dB or better in the audible range.

3.1.3 Sources of Noise

Apart from background noise from the environment, a significant contribution to the noise experienced in a dilution refrigerator STM system is that from the various pumps that run the cooling and circulation systems. The system uses three pumps which produce a lot of noise and heat; these pumps are located in an external pump shed behind the measurement room and connected only by their gas lines. The next significant source of noise in the system is from the turbulence created in the 1 K pot cooling stage. The 1 K Pot in dilution refrigerators works by taking liquid He-4 from the main bath of the cryostat to a separate pot where it is pumped upon. As its name suggests, this pot of pumped liquid helium can reach temperatures down to 1 K, in this particular system it tends to reach around 1.8 K. The liquid helium from the main bath is at a temperature of 4.2 K and flows into this approximately 1 K pot. Liquid helium undergoes a liquid-superfluid transition below a temperature of 2.18 K and when helium from the main bath flows into the 1 K pot, it undergoes a sudden phase transition into the superfluid phase producing turbulence. This turbulence causes vibration and disturbance that can be felt at the STM head itself and produces distortions and streaks of noise in STM images. In work by P. Gorla et al on eliminating this noise, it was found that the 1 K pot noise peaked at 11 kHz; a noise spectrum that was successfully reduced by thermalising the helium from the main bath before it flowed into the 1 K pot by introduction of a capillary system [50]. Another technique demonstrated by S. Pirro et al involved suspending the measurement device from the mixing chamber in their dilution refrigerator with a damped spring device, however this would be very unsuitable for STM [51]. The turbulence from the 1 K pot was heavily reduced in the system used in this work by simply opening the 1 K pot needle valve, letting in more liquid helium which naturally rests at 4.2 K, to raise the average temperature of the 1 K pot past the Lambda point. Due to poor thermal coupling between the 1 K pot thermometer and the 1 K pot itself, it proved ineffective to use the thermometer as a heater; but instead found the needle valve technique more than sufficient. The 1 K pot thermometer in optimal conditions would sit around 2.7 K, with minimal effect on the mixing chamber temperature, when operating in either mK

or 2 K mode.

3.1.4 Vibration Measurements

To measure the vibration spectra of the experimental environment, a Geospace Technologies GS-11D geophone was used in conjunction with a Stanford Research Systems SR560 Low-Noise Preamplifier and SR770 FFT Network Analyser. The geophone operates via a simple mechanism consisting of a fixed cylindrical permanent magnet core, surrounded by spring-suspended coils. When the coils oscillate due to environmental noise, their relative motion with respect to the magnet generate an electromotive force [36]. This electromotive force is the output voltage of the geophone, and its signal oscillations match the frequencies with which the geophone is stimulated. The geophone was positioned on the floating concrete block, with the output signal passing through the preamplifier and onto an FFT network analyser. The geophone used is specified to have an output of 9.223 V/in/s and a natural frequency of 0.97 Hz in the vertical direction.

3.1.5 Narrowband Vibration Spectrum

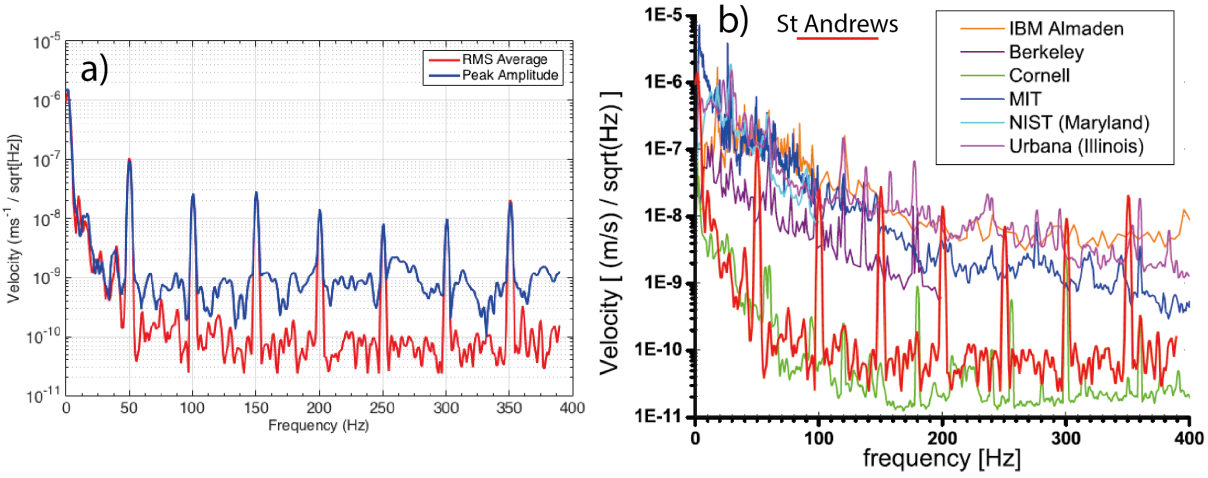

Figure 3.4: a) Narrowband vibration spectrum of one of the experimental rooms with the one-stage floating concrete block activated. FFT Network Analyser sampling time of 1.024 s, line width of 977 mHz with a span of 390 Hz. A pre-amplification setting of 500 times amplification was used. RMS and peak amplitude values are taken as an average over 20 samples. b) Comparison of vibration spectra of other low-vibration STM laboratories in the US. Plot derived from Jenny Hoffman's thesis [43].

The peaks in figure 3.4a at 50, 100, 150 Hz etc are simply the 50 Hz noise from the AC mains supply and its resonances and can be ignored with respect to mechanical vibrations. It can be seen in figure 3.4b that the performance of the one-stage isolation system used performs well in comparison to the other similar laboratories in the US. With the exception of Cornell, the environmental noise profile surpasses these laboratories. The mains electricity grid in the US runs at 60 Hz as opposed to 50 Hz in the UK, therefore the mains noise and associated resonance appear at 60, 120, 180 Hz etc instead.

3.1.6 Third-Octave Analysis

In many cases, high spectral resolution neither necessary nor useful for assessing acoustic noise levels in architectural and laboratory situations. Using a broadband analysis allows good reproducibility of results and ignores the finer details associated with individual resonances. One particular broadband analysis is one called Third-Octave Analysis, which subdivides the frequency spectrum into discrete bins of varying bandwidth, Δf. These bins effectively filter the signal into bins with constant relative bandwidth. The bandwidth is proportional to the centre-frequency of the bin, which therefore increases as the centre-frequency increases. The relationship between the upper (f_u) and lower (f_l) cut-off frequencies for each bin and the bin's centre-frequency (f_c) is given by:

$$f_c = \sqrt{f_l f_u}. \tag{3.15}$$

For the third-octave bandwidth, the upper and lower frequency cut-offs are related by:

$$f_u = \sqrt[3]{2} f_l, \tag{3.16}$$

which results in:

$$f_l = \frac{1}{\sqrt[6]{2}} f_c, \tag{3.17}$$

and

$$f_u = \sqrt[6]{2} f_c, \tag{3.18}$$

and thus:

$$\Delta f = (\sqrt[6]{2} - \frac{1}{\sqrt[6]{2}}) f_c \approx 0.23 f_c. \tag{3.19}$$

The third-octave bands are named as such because three adjacent filters (bins) form an octave band filter. The limiting frequencies are internationally standardised with regulations EN 60651 and 60652 [52].

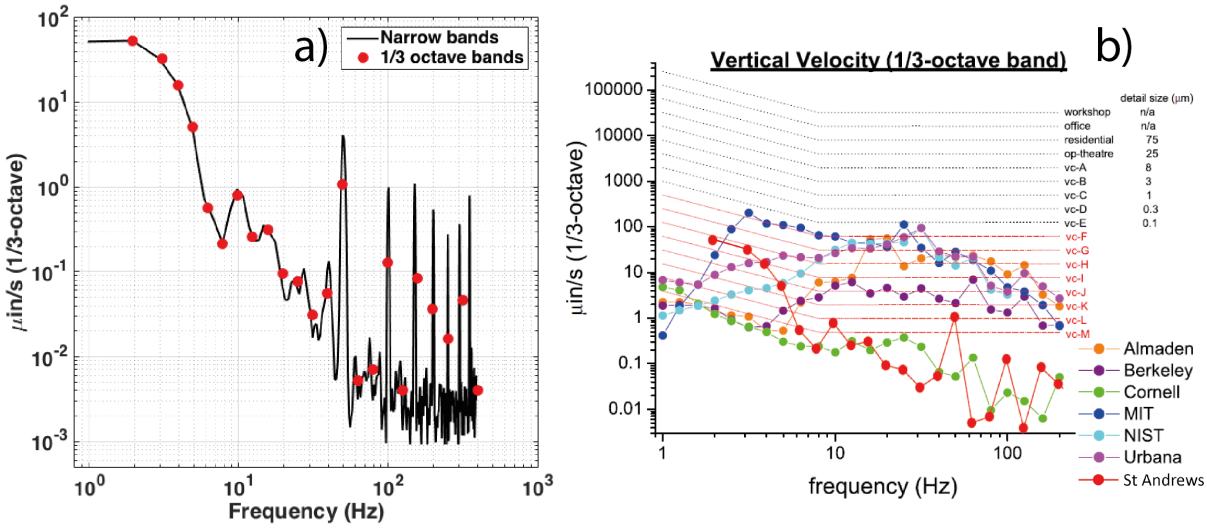

Figure 3.5: a) Third-octave analysis of the narrowband RMS vibration data on top of the original narrowband analysis. b) Third-octave analysis of the RMS vibration data compared with other laboratories in the US. Plot derived from Jenny Hoffman's thesis [43].

The vibration spectrum of the ULV is comparable to that of the highest performing STM environment in the US, matching the performance of Cornell at mid-ranged frequencies but lacking somewhat at the lower limit. The laboratory also performs on a very similar standard to the new low-vibration at the University of British Columbia Laboratory for Atomic Imaging Research (LAIR), with whom there was collaboration on comparing the isolation performance of both the ULV and the LAIR facility [53][54]. During spectro-

scopic measurements, only the floating concrete floor air spring system was used without the addition of the vibration table; this provided sufficient vibration isolation on its own evidently from the quality of data, especially topographies, in this work. The use of single-stage isolation systems has been found by other laboratories to perform just as well as more complex multi-stage systems [55].

3.2 Dilution Refrigerator

3.2.1 Introduction

In order to access the interesting quantum behaviour of materials, like superconductivity, extremely low temperatures are required. Earlier cryogenic techniques to achieve low temperatures, such as liquid nitrogen with its boiling point of 77 K and liquid ^{4}He with a boiling point of 4.2 K, were too warm to investigate many unconventional superconductors. Pumping on liquid ^{4}He, a common workhouse cryostat technique in low-temperature laboratories, can achieve, depending on pumping performance, down to around 1 K [56]. But to achieve the extremely low temperatures at which quantum phase transitions take place, or to probe quantum phenomena such as superconductivity or magnetic ordering; a dilution refrigerator is required, as to eliminate thermal fluctuations. A dilution refrigerator makes use of the cooling effect that is produced when a mixture of liquid ^{3}He and ^{4}He is circulated and pumped upon. Below $\sim$1 K, a mixture of the two liquids separates into a two-phase state: one rich in ^{3}He and one poor, with the ^{4}He acting as a background solvent. ^{3}He from the richer concentrated phase diffuses across the phase boundary into the ^{3}He poor phase, which costs energy due to their differing chemical potentials. As is expected of diffusion, eventually the two phases would evolve to form one phase again with a moderate ^{3}He concentration. To maintain this cooling process, the ^{3}He poor phase is pumped upon to maintain the concentration gradient to keep the process going. It can be seen from the phase diagram that in theory there would be no temperature floor to this process, since the two-phase region is maintained down to zero temperature. There

is however a minimum operational temperature simply from the thermal energy of the surrounding environment and the instrument itself [57]. An Oxford Instruments Kelvinox dilution refrigerator, used in this thesis, can achieve a base temperature of 10 mK.

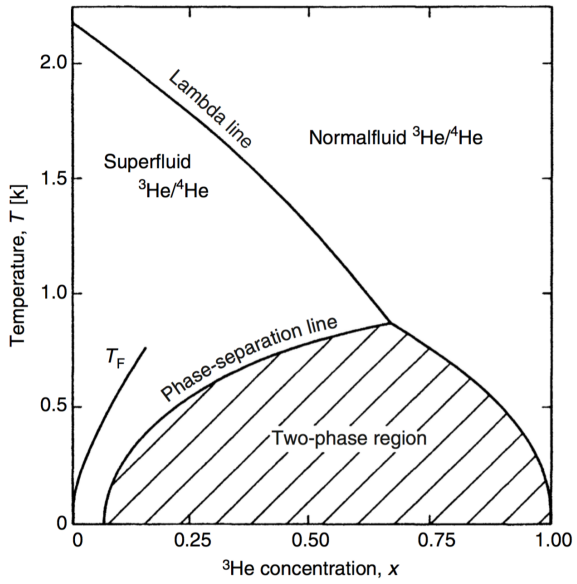

Figure 3.6: Phase diagram of liquid ^{3}He-^{4}He mixtures at saturated vapour pressure. Figure taken from [56]

The phase diagram of the liquid ^{3}He and ^{4}He mixture is shown in figure 3.6, which demonstrates that the two-phase region of the two differently concentrated mixtures exists all the way to 0 K. The line labelled T_F is the concentration dependence of the Fermi temperature of ^{3}He liquid, for where the liquid starts to behave quantum mechanically; since the cooling process is essentially from two quantum liquids. Figure 3.7a above shows the cooling power of typical cryostats that utilise either a ^{3}He cooling mechanism or a dilution refrigerator. At higher temperatures the less sophisticated ^{3}He technique has greater cooling power, but this quickly drops to zero around 300 mK. It is at this point that the dilution refrigerator outperforms the other cryostat and provides significant cooling power all the way to under 50 mK. In order to technically realise this cooling process, the dilution refrigerator has a number of cooling stages, each colder and deeper into the cryostat than the other.

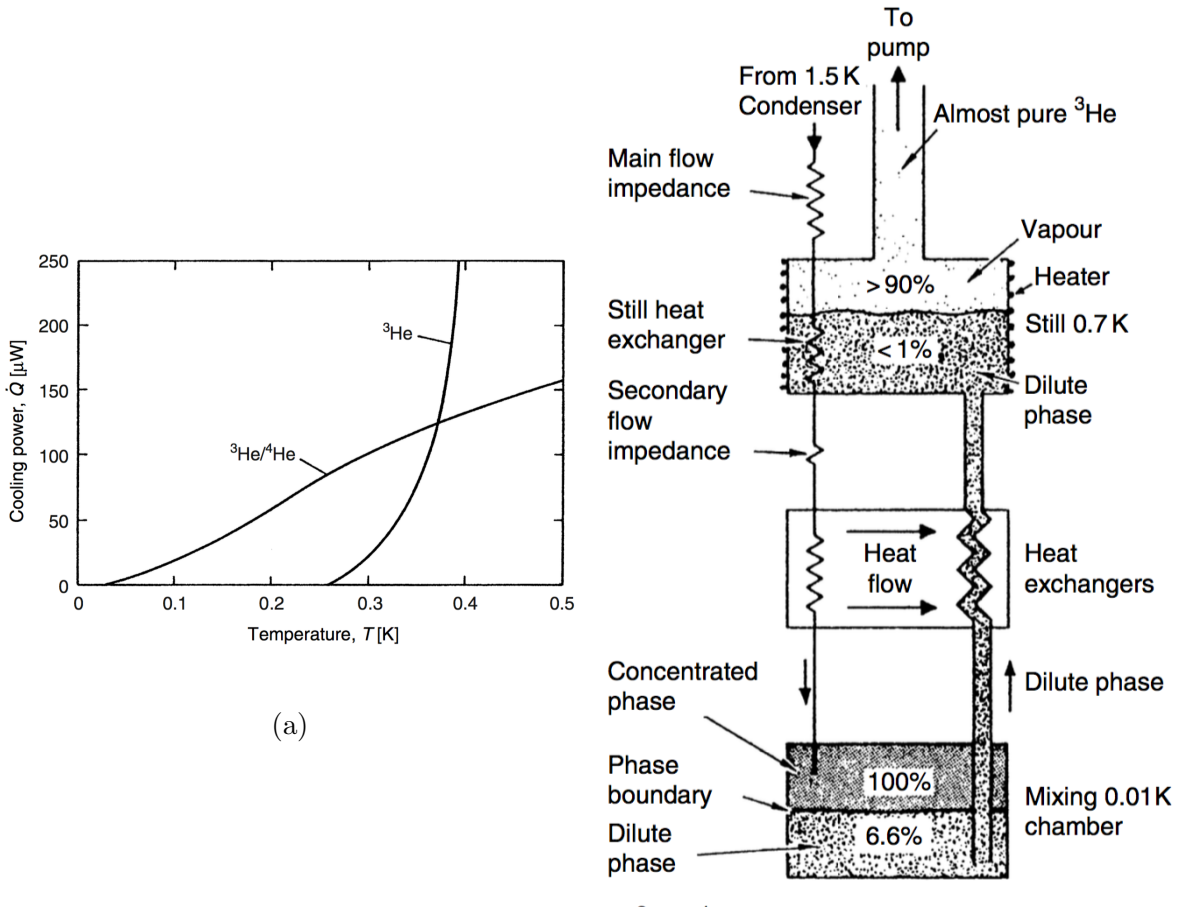

Figure 3.7: a) Cooling power of a ^{3}He evaporation cryostat alongside that of a ^{3}He-^{4}He dilution refrigerator, assuming identical pumps with gas circulation rates of 5 l s^{-1}. b) Schematic of a dilution refrigerator, within a conventional liquid helium cryostat. Figures taken from [56].

When the mixture begins circulating through the dilution refrigerator, it is first filtered of any dirt through a nitrogen and helium cold trap, which consist of steel-enclosed charcoal that are cooled down to liquid nitrogen and then a liquid ^{4}He temperatures respectively. The mixture then enters the refrigerator where it condenses at the 1 K pot, although in a separate system with a heat exchanger. Once the liquid condenses it flows to the bottom of the refrigerator to the mixing chamber where it is allowed to sit and phase separate into its ^{3}He rich and dilute phases. To maintain the concentration gradient needed for cooling, this chamber is pumped upon by a standard rotary pump with a booster pump in series. As the ^{3}He dilute component of mixture is pumped away it comes up through the

refrigerator to the still, which is a fairly large reservoir to enable the pumping action to provide additional cooling further up the refrigerator; which via another heat exchanger helps to cool the incoming mixture as it cycles through. The still is designed wide and shallow to provide as large a ratio of ^{3}He to ^{4}He in the vapour phase as possible to provide a sufficient circulation rate for cooling down in the mixing chamber [56]. This still reaches typically 700 mK whereas the mixing chamber itself, where the STM or often transport apparatus is positioned near to, reaches 10 mK. As the dilute mixture is pumped away from the still, it gets filtered in the before mentioned cold traps and cycles through continuously. A typical Oxford Instruments dilution refrigerator (Kelvinox 400HA) has a cooling power of 400 μW at 100 mK.

3.3 Millikelvin STM

The microscope used for the data in this thesis is a millikelvin STM, based on a modified Oxford Instruments Kelvinox dilution refrigerator that allows line-of-sight sample transfer, with a sapphire STM head attached below the mixing chamber. The dilution refrigerator insert itself is enclosed within an Oxford Instruments 14 T superconducting magnet and cryostat. The choice of sapphire for the STM head produces great mechanical stiffness and thermal conductivity at low temperatures [33]. The instrumental set up has been pre-characterised when it was located at the Max Planck Institute for Solid State Research in Stuttgart (MPI-FKF), and was been measured to reach a base temperature of below 10 mK and an effective electronic temperature of $\sim$100 mK [58]. The dilution refrigerator used is a wet system, where liquid helium is used for cooling and this helium is not used in a closed cycle system, where boil-off is collected in a recovery line to be re-liquified by the university. This choice of system has the disadvantage of requiring manual refills of liquid helium and nitrogen in order to operate, but the absence of a built in compressor and recycling systems provides optimal vibration and therefore spectroscopic conditions. Both closed-cycle and pulse tube refrigerator designs produce too much noise for microscopy purposes and produce spectroscopy with much poorer resolu-

tion and topographies with significant acoustic interference [59][60]. Although much work is going into reducing the noise of dry and closed-cycle systems, that would eventually increase measurement time by removing the need to manually transfer liquid cryogens at regular intervals.

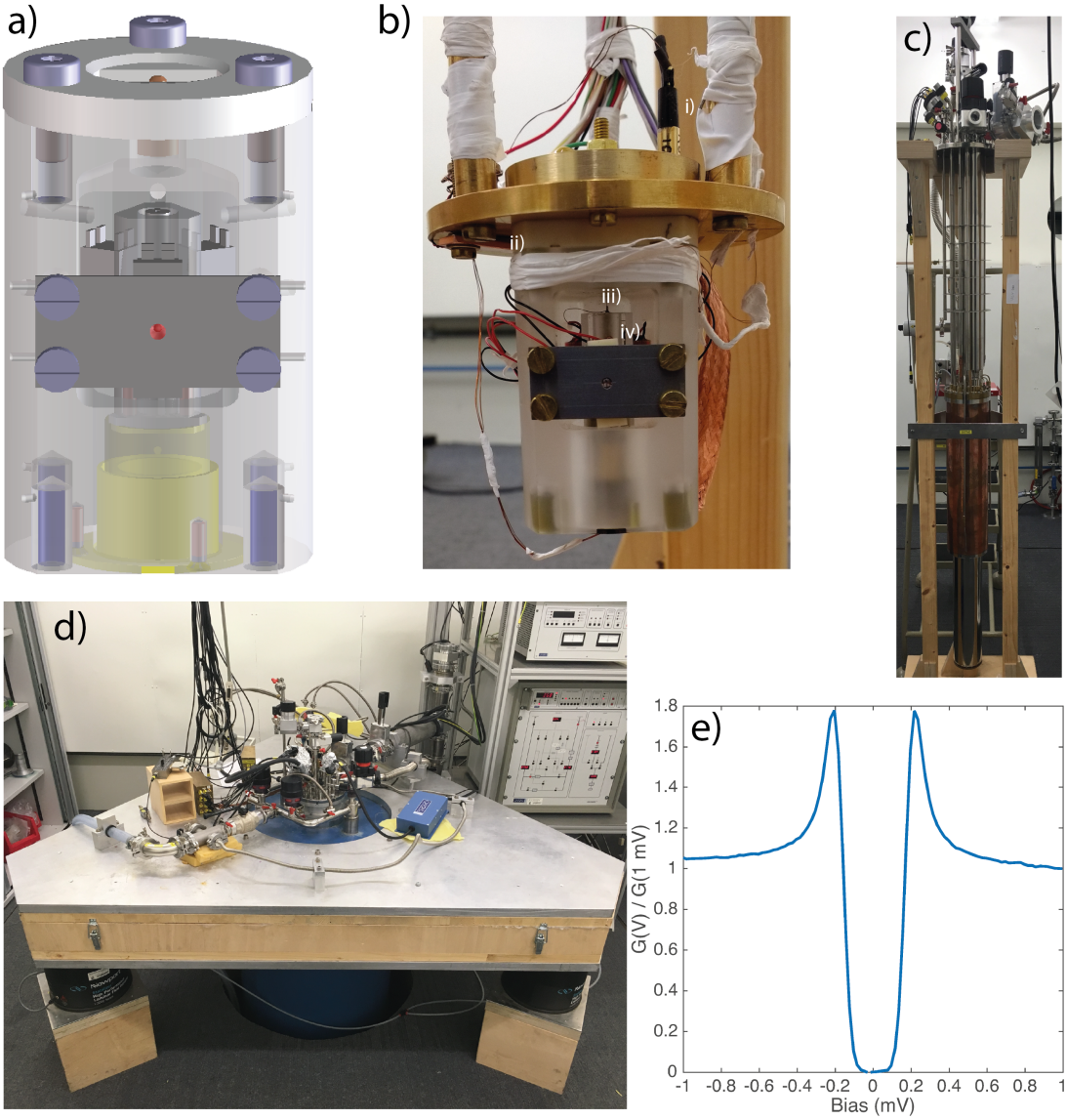

Figure 3.8: a) 3D design image of the STM head and b) a photograph of the STM head used here whilst outside the dilution refrigerator for maintenance, with i) temperature sensor, ii) Hall probe, iii) STM tip and piezo and iv) coarse approach walker. c) Dilution refrigerator insert containing the STM. d) Experimental set up showing the cryostat (blue) attached to the vibration table and various connecting pipes. e) High-resolution superconducting gap spectrum of Sn_4As_3, a non-centrosymmetric superconductor with a $T_c \sim 1.2$ K [61], recorded on this STM at 50 mK in zero-field, using $V_s = 8$ mV, $I_s = 0.4$ nA and $V_L = 25$ μV.

The STM tip is manipulated using piezo-actuators, that are controlled by a Digital Signal Processor (DSP) with the open-source gxsm program [62], to control the position of the STM tip and spectroscopy settings. Samples are transferred to the STM through line-of-sight access with a long manipulator, passing through radiation shields that reduce RF noise and separated chambers to limit thermal coupling to warmer stages. The cryostat containing the microscope is mounted to a table which rests on three air springs to dampen vibrations. This table itself sits on a large concrete block which floats on much larger air springs in the centre of the room; twice decoupling the microscope from vibrations from the environment. In order for the vibration stages to move freely, custom designed flexible bellows are used to maintain high vacuum whilst moving with the air springs. The three pumps needed to operate the dilution refrigerator are positioned in an external pump shed behind the laboratory to reduce exposure to noise the microscope would experience. Spectroscopic measurements are performed using a standard lock-in technique using a Stanford Instruments SR830 amplifier with a frequency of 437 Hz and the tunnelling current itself is amplified using a Femto DLPCA-200 amplifier. A Hall probe is positioned close to the STM head which is controlled by another SR830 amplifier to provide readings of the magnetic field as close as possible to the sample and take into account any residual field in the superconducting magnet for field sensitive measurements. The electronics for recording spectroscopy were calibrated to have a vertical offset of -2.5 mV in the dI/dV channel, which is accounted for in this thesis.

Chapter 4

Scanning Tunnelling Microscopy and Spectroscopy of UPt_3

4.1 Background

4.1.1 Superconductivity

UPt_3 is an unconventional heavy fermion superconductor, with effective electron masses of the order of hundreds of free electron masses and the superconductivity itself being a candidate for p-wave pairing [23]. p-wave in the sense that the symmetry of the superconducting gap resembles that of an electronic p-orbital, implying spin-triplet pairing; as opposed to the simple spherical symmetry of s-wave. Many experiments have alluded to the p-wave character of the superconductivity in UPt_3, including recent Magneto-Kerr microscopy work by E. R. Schemm et al [63] and Knight shift studies by H. Tou et al, which saw a constant Knight shift as a function of temperature as UPt_3 passed through its superconducting transition(s) [5], suggesting the existence of S = 1 Cooper pairs. What could be considered the sister p-wave compound of UPt_3 is Sr_2RuO_4, which likewise has demonstrated a constant Knight shift through its superconducting transition in work by K. Ishida et al [4].

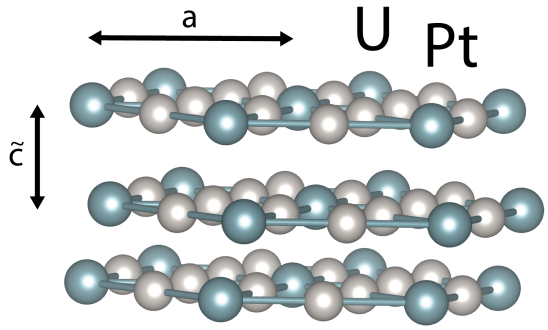

(a) Crystal structure of UPt_3.

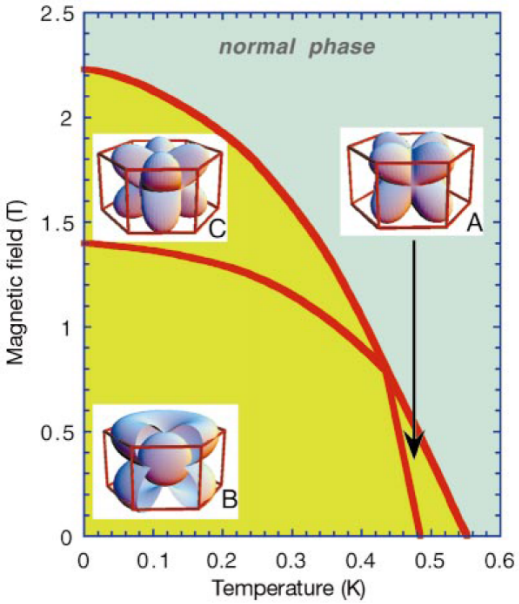

(b) Phase diagram of UPt_3.

Figure 4.1: a) Crystal structure and b) low temperature phase diagram of UPt_3 for magnetic fields applied out of the basal plane. Second-order phase transitions separate three different superconducting phases, labelled A, B and C [64].

UPt_3 forms a triangular lattice, where the uranium atoms form a close-packed hexagonal structure with the platinum atoms bisecting their planar bonds; with lattice parameters of a = 5.764 Å and $\tilde{c}$ = 4.899 Å, such that $\tilde{c}/a = 0.845$. This distance scale $\tilde{c}$ represents the distance between neighbouring planes instead of a unit cell height [23]. UPt_3 has three distinct superconducting phases, each of which is associated with a different superconducting gap symmetry. The transition temperature in zero-field is split into two second order transitions at 480 mK and 530 mK, with a tetra-critical point around 450 mK owing to a higher magnetic field superconducting state. Specific heat measurements have revealed this splitting in the critical temperature as two peaks in the transition in work by J. P. Brison et al [65]; as well as neutron scattering experiments revealing changes in the symmetry of the superconducting flux-line lattice (FLL) across the three phases in work by A. Huxley et al [64]. The changes in the superconducting order parameter symmetry across the superconducting phases have also been been observed in thermal conductivity measurements, which saw a jump in the derivative of the thermal conductivity with respect to temperature, as the system went between its A and C superconducting phases

[66]. The exact p-wave nature of the superconductivity in UPt_3 has yet be confirmed conclusively, however thermal conductivity measurements did reveal field-temperature scaling relations consistent with the presence of line nodes in the gap structure [67]. p-wave spin-triplet superconductors like UPt_3 have been predicted to exhibit phenomena such as magnetic skyrmions ($2\Phi_0$ magnetic flux, spin-textured quasiparticles) [68] as well as half-quantum vortices; both of which could be probed with Scanning Tunnelling Microscopy when a magnetic field is applied. Half-quantum vortices would reveal themselves as a lattice of paired vortices, or as twice the number of expected vortices, in a formation largely the same as standard Abrikosov vortices in type-II superconductors; in addition to a density of states spectrum that has been predicted to exhibit doubled coherence peaks compared to that of an ordinary superconductor [69]. As a consequence of p-wave superconductivity with half-quantum vortices, UPt_3 should support Majorana fermions: zero-energy quasiparticles that are their own antiparticles. A Majorana Fermionic state would obey non-Abelian statistics, an important phenomenon for describing the quantum Hall state and the operation of quantum computers [70]. Alexei Kitaev was the first to propose the idea of storing quantum information in Majorana fermions, requiring only the proximity of a three-dimensional p-wave superconductor to a quantum wire [71]. A pair of widely separated Majorana fermions bound to half-quantum vortices would also be expected to have a very long coherence time, something essential for quantum computation [72][73]. The superconductivity in UPt_3 is also suspected to be topological in nature [74] and something even more exotic as Möbius topological superconductivity [75]. The robustness of topological states produces the long coherence times required for practical quantum information devices. However, the superconductivity in UPt_3 is known to be nodal and as a consequence low-energy excitations are inherent, which are expected to prevent the occurrence of macroscopic quantum phenomena such as the manipulation of qubits [76]; however experiments on a d-wave superconducting Josephson junction, which is nodal by nature, exhibited macroscopic quantum properties [77]. As a consequence nodal p-wave superconductors such as UPt_3 may still be compatible with quantum computation.

4.1.2 Antiferromagnetism

Below $T_N \simeq 5$ K, UPt_3 makes a transition into antiferromagnetic order, with small staggered moments of the order of 0.01 μ_B/U atom [23].

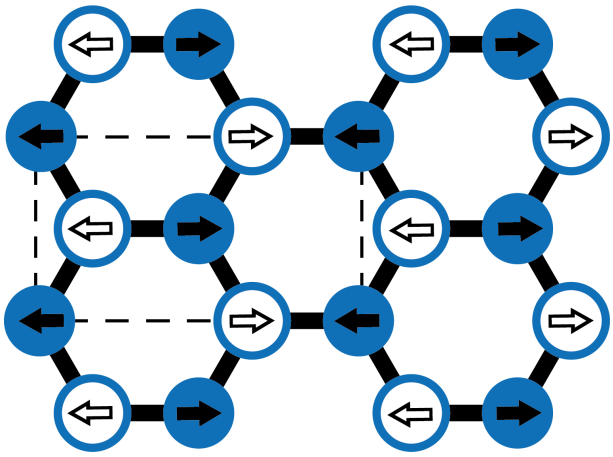

Figure 4.2: 1-Q Antiferromagnetic structure of UPt_3, with the arrows representing the spins on each U site and the solid blue circle representing a U atom at z = 3/4 c in the magnetic unit cell and hollow blue circles representing the U atoms at z = 1/4 c. This antiferromagnetic order has a doubled orthorhombic unit cell, indicated by the dashed rectangle. The solid blue U atoms make up the surface U layer as a triangular lattice. Figure adapted from [78].

Neutron diffraction experiments demonstrated that the antiferromagnetic order is robust in magnetic fields applied along the basal plane up to 3.2 T, by probing the intensity of the magnetic Bragg peaks at Q = (0.5, 1, 0) and Q = (-1.5, 1.5, 0) as function of the magnetic field [79]. These Q vectors are chosen because of the selection rules guiding neutron scattering, in which the $\underline{\mathbf{Q}}$-vector of the incoming neutron cannot be parallel to the magnetic ordering vector $\underline{\mathbf{M}}$; thus the most simple vector describing the magnetic order ($\pm$0.5, 0, 0) is inaccessible with neutron scattering. The AFM order is robust to higher fields than the superconductivity, which has H_{c2} only around 2.2 T [64], a fact which could be significant for the role of spin fluctuations. This antiferromagnetic order is suppressed and ultimately destroyed when a critical hydrostatic pressure is applied of $p_c = (5.4 \pm 2.9)$ kbar. In addition, the destruction of the antiferromagnetic order in UPt_3 follows the suppression of the splitting in specific-heat anomalies, i.e. the suppression of the multiple superconducting phases at temperatures below 0.5 K [78].

For magnetic fields applied out of plane, elastic neutron scattering measurements by Bruls et al noted only a small drop in the Néel temperature from $T_N = 5.5$ K in zero-field down to 4.1 K in 10 T applied field [80][81]. Neutron scattering data in high magnetic fields was eventually reanalysed in work by J. Moreno et al [82], which found that whilst neutron scattering data is consistent with the previously mentioned single-Q order (with three equivalent domain structures), as well as a more complex triple-Q order; the intensities of the neutron signals could be explained by a model where AFM domain walls are pinned to defects such as stacking faults; stacking faults have been detected in even the best single crystals available and are therefore likely seen in all the AFM experiments on UPt_3. A triple-Q AFM order would lead to frustrated magnetism, with a similar structure to that seen in UNi_4B, where competition between Kondo and AFM exchange effects govern its magnetic structure. A competition which would likely be as important in a triple-Q UPt_3 [82][83]. Strong pinning of superconducting vortices at domain walls was observed in work by A. Amann et al [84], especially the superconducting B-phase, which exhibited no detectable creep; suggesting a strong pinning mechanism in the low temperature phase of UPt_3 [84]. Such domain walls have been observed directly in Transmission Electron Microscopy measurements by P. A. Midgley et al, as well as a macroscopic incommensurate structural modulation [85]. However the necessary in-plane spin rotations suggested by J. Moreno et al are inconsistent with the second-order phase transition for the AFM order, as well as other neutron scattering experiments [79].

4.1.3 Heavy Fermion Character

The heavy fermion character of UPt_3 has long been established, ever since the first specific heat measurements by Frings et al [86] where on polycrystalline samples, the specific heat over temperature (C / T) showed an upturn below 10 K, with a zero-temperature intercept γ of about 420 mJ/mole K^2. Further specific heat work by G. R. Stewart et al revealed the existence of a $T^3 \ln T$ term in the specific heat which is also known as the spin-fluctuation term; as well as transitions into superconductivity at 0.54 K through resistivity, AC susceptibility and specific heat [87]. The heavy fermion behaviour of UPt_3 comes about

through the hybridisation of the itinerant Pt 5d electrons and the highly-localised U 5f electrons which behave as a standard Kondo lattice [23]. At the time it made UPt_3 the third ever heavy-fermion superconductor and the first one with the spin-fluctuation term in specific heat [13]. A few years later, quantum oscillations experiments, specifically using the de Haas-van Alphen (dHvA) effect, demonstrated heavy quasiparticles on the order of tens of free electron masses in work by L. Taillefer et al [88]. The dHvA results were consistent with a model of a five band Fermi surface and later expanded upon from work by G. J. McMullan et al [89], which concluded that all three uranium f-electrons are delocalised in UPt_3 with effectives masses in some quasiparticle bands of the order a hundred free electron masses [89]. Since UPt_3 is a strongly correlated heavy fermion compound, it is expected that the density of states as seen in STS should exhibit a Fano resonance line-shape.

4.2 Topography

The UPt_3 samples were provided by Andrew Huxley, which were grown in ultra-high vacuum (UHV) with the Czochralski process under batch number U47H1A1 and were cleaved in-situ at cryogenic temperatures ($\sim$4.2 K) in high-vacuum. A sample from the same batch recently had its T_c measured to be $\sim$550 mK in resistivity measurements by Chris O'Neill at the University of Edinburgh, confirming the sample quality and presence of the superconductivity. The cleaved surface of UPt_3 revealed itself as regions of non-cleaved rubble and patches of atomically flat surfaces. Previous preliminary work at the MPI-FKF in Stuttgart produced a cleaved surface, with the hexagonal lattice visible in the Fourier transform, but with a greater concentration of defects that made the atomic lattice difficult to see. High-quality surfaces were cleaved here when the prepared UPt_3 sample was allowed to cool inside and on top of the cleaving stage for up to 3 hours before cleaving.

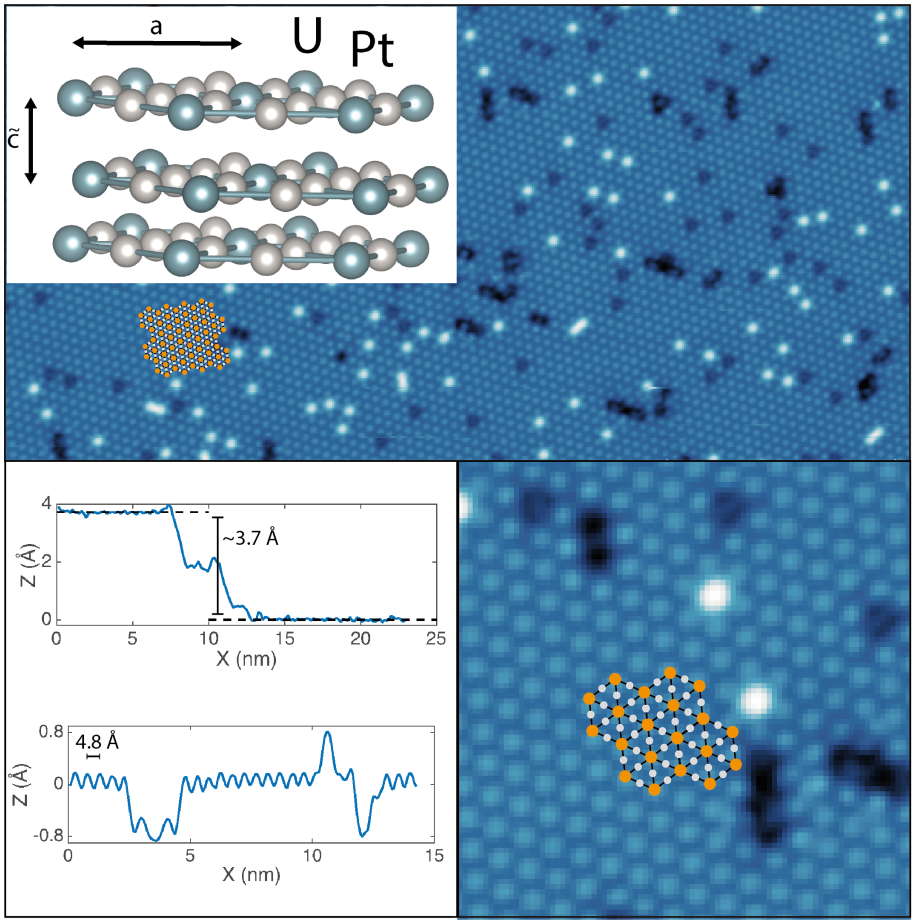

Figure 4.3: Crystal structure of UPt_3 alongside a topographic image of UPt_3 taken at 25 mK with an image size of 40 nm by 20 nm, using $V_s = 50$ mV and $I_s = 0.1$ nA. In the lower-right quadrant the same topography is enlarged. In addition line-cuts have been extracted to show a step-edge and the atomic corrugation with defects.

It can be seen in the topography in figure 4.3 that the surface contains many defects. The darker patches are those areas with vacancies of missing uranium atoms and bright spots of superficial atoms, most likely uranium atoms since UPt_3 has no natural cleavage plane. These bright defects also match the uranium sites in particular and appear the same size as the unaffected uranium atoms, where the platinum atoms in UPt_3 are packed in a much tighter arrangement as seen in the crystal structure in figure 4.1. The defects on the surface typically make up ∼10% of the atomic sites, providing an ideal platform for QPI and may itself be related to crystal quality and therefore RRR.

4.3 Normal State Spectroscopy

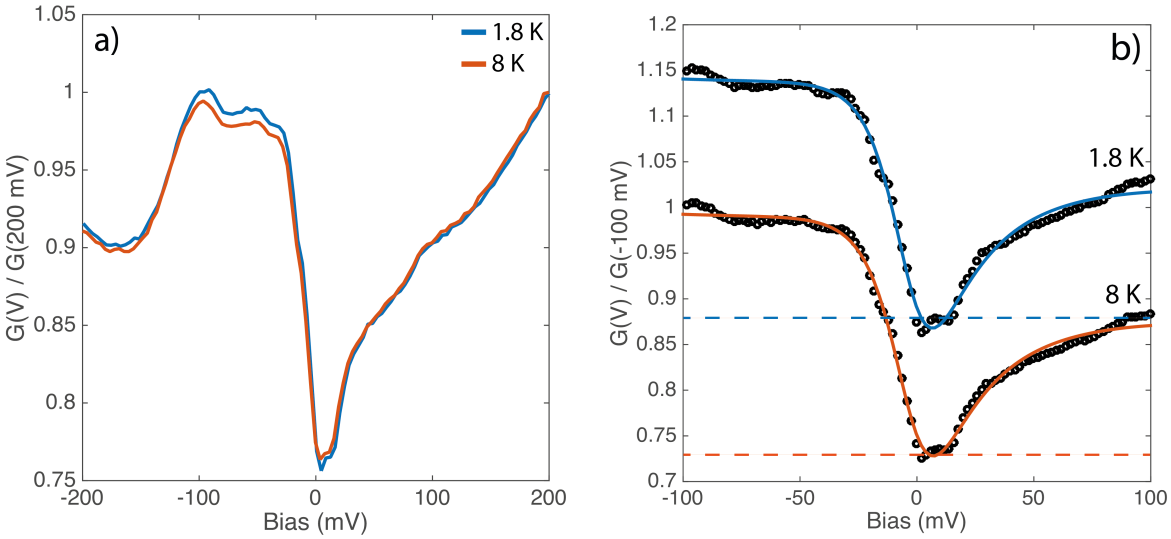

Figure 4.4: a) 8 K and 1.8 K average spectra of UPt_3 taken as averages over $(3\ nm)^2$ area and 64 spectra. Both data sets used $V_s = 200$ mV, $I_s = 0.2$ nA and $V_L = 4$ mV. Spectra are normalised to their conductance values at 200 mV. b) 8 K and 1.8 K average spectra of UPt_3 taken as averages over $(3\ nm)^2$ area and 64 spectra. Both data sets used $V_s = 100$ mV, $I_s = 0.1$ nA and $V_L = 2.5$ mV. Spectra are normalised to their conductance values at -100 mV and the 1.8 K data is offset by 0.15; in addition the minima of the 8 K spectra is indicated with a dash orange line with the 0.15 relative conductance offset above it in blue. A least-squares fitting of the standard Fano resonance formula plus an extra linear and offset term is imposed over the data (solid lines). The fit produced a resonance-width $\Gamma = 20.9$ mV and a Fano parameter $q = -0.414$ for the 8 K data and $\Gamma = 20.4$ mV and $q = -0.412$ for the 1.8 K data.

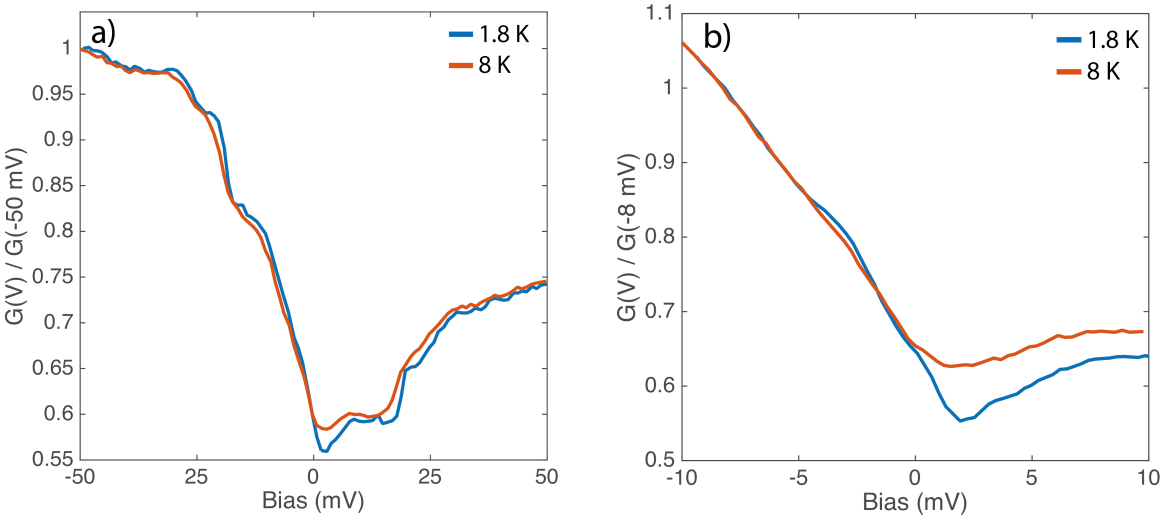

Figure 4.5: a) 8 K and 1.8 K average spectra of UPt_3 taken as averages over $(3\ nm)^2$ area and 64 spectra. Both data sets used $V_s = 50$ mV, $I_s = 0.1$ nA and $V_L = 1$ mV. Spectra are normalised to their conductance values at -50 mV. b) 8 K and 1.8 K average spectra of UPt_3 taken as averages over $(3\ nm)^2$ area and 64 spectra. Both data sets used $V_s = 10$ mV, $I_s = 0.1$ nA and $V_L = 0.5$ mV. Spectra are normalised to their conductance values at -8 mV.

The wider range spectra in the normal state follow a basic Fano resonance line-shape as an asymmetric V-shaped curve in the ±100 mV region, with the addition of a peak at -100 mV (figure 4.4); where upon closer inspection at small energies there are the signatures of two symmetric steps in conductance at ±20 mV (figure 4.5). The minima of the spectra occur approximately 2 mV above the Fermi level in a small dip below 10 mV. After cooling down to 1.8 K, spectral features become much more well defined thanks to reduced thermal broadening. The peak at -100 mV is much sharper, as well as the symmetric steps in conductance at ±20 mV. In addition, a small gap-like feature begins to appear at the DoS minimum 2 mV above the Fermi level. Comparing the spectra at 1.8 K and 8 K by directly overlaying them, it is clear that reducing the temperature sharpens spectral features where here the lock-in modulation and therefore lock-in broadening is the same for both sets of spectra.

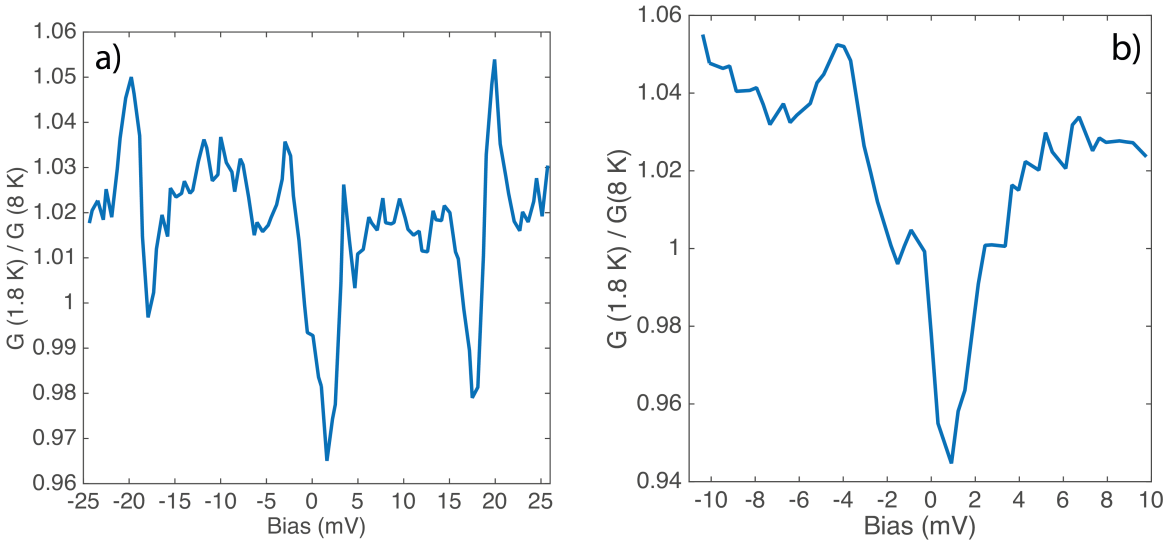

Figure 4.6: a) 1.8 K average spectrum as a fraction of the 8 K spectrum of UPt_3 taken as averages over $(3\ \text{nm})^2$ area and 64 spectra. Both data sets used $V_s = 25$ mV, $I_s = 0.1$ nA and $V_L = 0.5$ mV. b) 1.8 K average spectrum as a fraction of the 8 K spectrum of UPt_3 taken as averages over $(3\ \text{nm})^2$ area and 64 spectra. Both data sets used $V_s = 10$ mV, $I_s = 0.1$ nA and $V_L = 0.5$ mV.

Another way of visualising this change in spectral features is to plot the 1.8 K spectra normalised to the 8 K spectrum. The 8 K data can be considered to be background-like to highlight any changes that occur as the temperature is lowered. It can be seen therefore in figure 4.6 that the symmetric steps at ±20 mV have drastically increased sharpness and that the gap-like feature at 2 mV is more convincingly opening up at lower temperatures from their increased depths once normalised.

4.4 Superconducting State

4.4.1 Superconducting State Spectroscopy

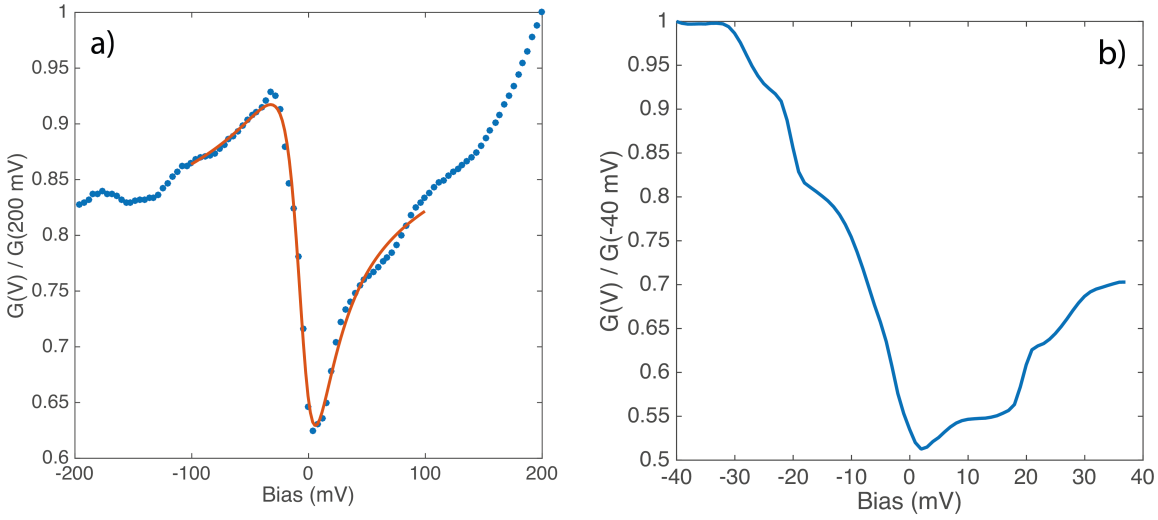

Figure 4.7: a) 25 mK spectrum of UPt_3 obtained from an average over an area of $(4\ nm)^2$ and 256 spectra, using $V_s = 200$ mV, $I_s = 0.2$ nA and $V_L = 5$ mV. A least-squares fitting between ± 100 mV of the standard Fano resonance formula plus an extra linear and offset term is superimposed over the data (orange). The fit produced a resonance-width $\Gamma =$ 17.9 mV and a Fano parameter $q =$ -0.61. b) 25 mK spectrum of UPt_3 obtained from an average over an area of $(17.3\ nm)^2$ and 96^2 spectra, using $V_s = 40$ mV, $I_s = 0.2$ nA and $V_L = 2$ mV.

Cooling down to 25 mK to access the superconducting state of UPt_3 revealed no observable change in the wider range spectra, apart from increased sharpness of features, especially the steps at ± 20 mV and perhaps now a more obvious pair at ± 30 mV; as well as the gap-like feature just above the Fermi level.

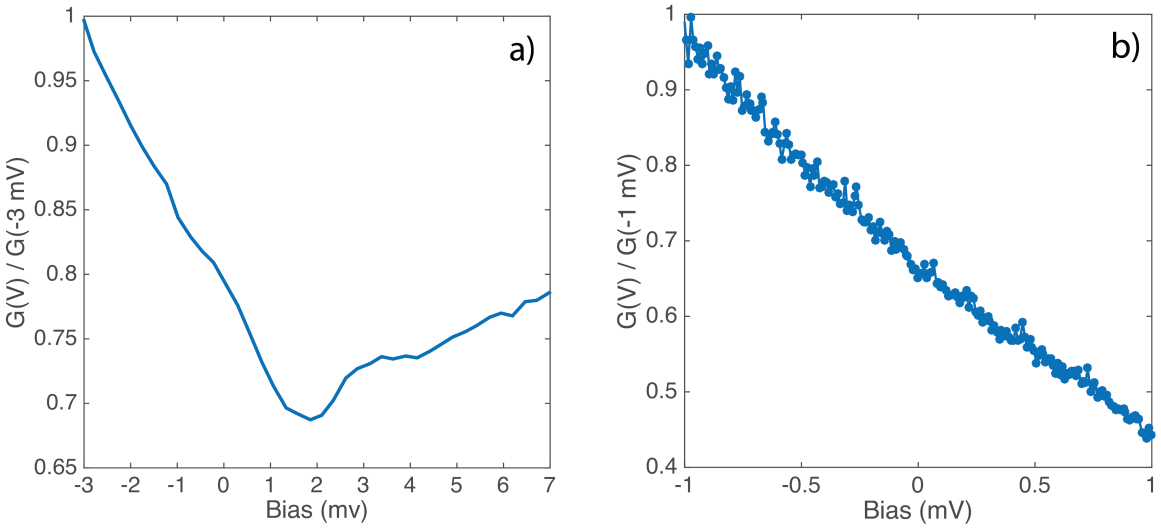

Figure 4.8: a) 25 mK spectrum of UPt_3 obtained from an average over an area of $(4\ \text{nm})^2$ and 64 spectra, using $V_s = 10$ mV, $I_s = 0.1$ nA and $V_L = 0.5$ mV. b) 25 mK spectrum of UPt_3, taken as an average of 7 high-resolution point spectra, using $V_s = 4$ mV, $I_s = 0.5$ nA and $V_L = 25\ \mu$V.

Unexpectedly the superconducting gap was never detected in this investigation of UPt_3 nor were any vortices observed. Figure 4.8 shows the result of averaged high-resolution spectra in zero-field and at 25 mK. Similar heavy fermion superconductors, such as $CeCoIn_5$ had its weak superconducting gap measured with STS in work by M. P. Allan et al [90], however with a much higher critical temperature of $T_c \simeq 2.3$ K. The microscope itself was characterised upon initial construction in an instrumentation paper by U. R. Singh et al [58], demonstrating an effective electronic temperature of 140 mK, well below the superconducting transition temperatures of UPt_3. In addition, recent measurements on a non-centrosymmetric superconductor, with a T_c of the same order of magnitude ($T_c \sim 1.2$ K) [61], revealed that the instrument has sufficient resolution for such such low temperature superconductors (see figure 3.8). Even though UPt_3 is widely believed to be a p-wave superconductor, especially with established experiments such as the Knight shift in work by H. Tou et al [5], assuming a BCS-like relation between the critical temperature and the size of the superconducting gap of $\Delta \simeq 1.76 k_B T_c$, one would have expected a superconducting gap of the order of 80 μeV; whereas the electronic temperature would suggest an energy resolution, $k_B T_e \simeq 12\ \mu$eV, confirming that the superconducting gap

should have been easily detected. UPt_3 is similar in this case to URu_2Si_2, where a full superconducting gap has likewise not been detected in STS studies when the sample is cleaved in situ, however signatures of it has been detected using a superconducting aluminium tip when cleaved in air and at room temperature [91]. Within the hidden order (HO) phase and gap, there were weak signatures of another gap-like structure opening up below 1.7 K in work by E. H. Vasco et al, revealed by dividing the zero-field spectra by the 4 T spectra to normalise to the normal state. A BCS fitting of this gap structure produced a gap size of 0.23 meV and a critical temperature of $T_c \sim 1.7$ K and accurately followed the standard BCS Δ(T) dependence. However the decrease in conductance for this gap was minimal at the surface due to a suppression mechanism that is not yet fully understood [92].

However, if UPt_3 were indeed a p-wave superconductor, it is expected that the superconductivity would be suppressed at the surface. A quasi-classical study of the surface effects in unconventionally paired superfluids, one of which was the p-wave pairing in ^{3}He, demonstrated how the order parameter would be suppressed and reorientated at the surface in work by V. Ambegaokar et al [93][94]; which for a p-wave superconductor would be its superconducting gap $\Delta(\underline{\mathbf{k}})$, via the vector order parameter $|\mathbf{d(k)}|^2$. In particular, work by L. J. Buchholtz et al explored ways to identify p-wave superconductors and in particular via the tunnelling density of states. It was revealed that the component of the order parameter for a p-wave superconductor perpendicular to the surface would be suppressed to zero, whereas the parallel components are slightly enhanced. This depression of the perpendicular component is believed to act as a potential well for quasiparticle excitations, which would lead to an interesting gap structure [95]. Whereas for an ordinary s-wave superconductor, there is no suppression of the order parameter at the surface. This suppression of the superconducting gap, if it were p-wave, could help explain why no superconducting gap was detected at the surface of UPt_3. Another, and less exciting, explanation for the lack of superconducting gap in this investigation could be that the defect ridden surface caused too much scattering for the STS to comfortably detect the weakened gap.

4.4.2 Heavy Fermion Behaviour and the Fano Lattice

Heavy fermion, as a descriptive name for some materials, was created to describe Kondo lattices that have specific heat coefficients typically greater than 400 mJ/mole K^2 [10]. Heavy fermion materials include similar compounds to UPt_3, such as $CeCu_2Si_2$ which has a coefficient on the order of ∼1100 mJ/mole K^2, which is even greater than that of UPt_3 with a coefficient of ∼420 mJ/mole K^2 [10]. Heavy fermion materials behave as local moment systems at high temperatures, something that did not make these materials obvious candidates for superconductivity [10]. However, superconductivity has been seen in many heavy fermion compounds such as $CeCu_2Si_2$, UBe_{13} and URu_2Si_2 in addition to UPt_3, as well as the more recent discovery in $CeCoIn_5$ [90].

In recent work by A. R. Schmidt et al, STM/STS was used to image what is called the Fano lattice and the transition to 'hidden order' at low temperatures in the heavy fermion superconductor URu_2Si_2 [96]. In URu_2Si_2, at around 55 K the light d-electron bands from the Ru atoms begin to screen the magnetic moment of the U-based f-electrons [96]. These uranium f-electron sites provide a periodic array of Kondo sites, where in URu_2Si_2, the screening behaviour kicks in below ∼55 K, then at far lower temperatures the heavy fermion behaviour appears, with electron masses ∼25 m_e [96]. There is a transition to antiferromagnetism at $T_N \sim 17.5$ K and into superconductivity at $T_c \sim 1.5$ K. At the same time as the AFM transition at 17.5 K, a partial energy gap opens up from the Fano lattice, with no associated density wave signatures. What is observed in quasiparticle interference is the rapid splitting of a light k-space band into two heavy bands [96]. This phase is called a hidden order phase since the state emerges from the Fano lattice and is associated with changes in the uranium site hybridisation, instead of a conventional density wave [96].

This URu_2Si_2 investigation visualised the Fano lattice, with the key parameters such as the energy of the many-body state, the hybridisation strength and the asymmetry parameter between the two tunnelling channels, varying with the atomic lattice; but it was the first to see the light-band splitting. The many-body state was on average between

3-4 meV and greatest on the uranium sites and minimum on the silicon sites. Similarly the hybridisation strength, Γ, was greatest on silicon sites and weakest on the uranium sites; in addition to the tunnelling channel probability ratio varying atomically [96]. The same hidden order and Kondo lattice was visualised by P. Aynajian et al in another study on URu_2Si_2 which saw the atomic variation of the asymmetry parameter q, which was maximum between uranium atom sites, indicating higher tunnelling probability at these inter-atomic sites to the Kondo resonance [97]. Similarly in this investigation of UPt_3, which was already known to be a heavy fermion compound, the Fano lattice was observed by fitting the Fano resonance line-shape in addition to a simple linear background to each pixel in a spectroscopic map, in the same way as the averaged spectrum in figure 4.9 below.

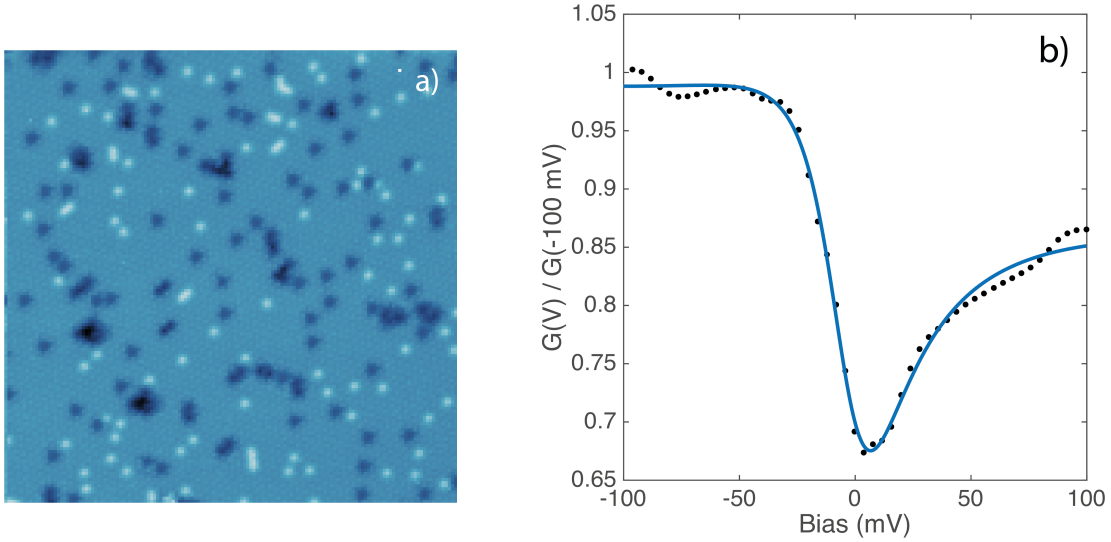

Figure 4.9: Spectroscopic map taken at 25 mK over a $(26\ \text{nm})^2$ area with 146^2 pixels, using $V_s = 100$ mV, $I_s = 0.1$ nA and $V_L = 5$ mV. The topography output of the spectroscopic map is shown in sub-figure a) and the average spectrum from this map is displayed in b) with a Fano resonance fit which produced a resonance-width of 21.3 mV and Fano-parameter q = -0.438.

It can be seen in figure 4.9 that the average spectra displays the asymmetric nature of the Fano resonance and the local topographic area under investigation. The energy scale of this Fano resonance, with a fitted width, Γ, of the order 20 mV is reasonably consistent with the band-width of the U 5f-band, measured in high-resolution ARPES experiments by T. Ito et al, which measured a bandwidth of ∼50 meV [98]. However the energy

resolution of the ARPES experimental setup was also of the order of ∼50 meV, so the real value could potentially be smaller than this and therefore closer to the Fano-width seen in STS. Extracting the value of the Fano parameter q, a measure of the asymmetry in the spectrum, reveals the clearest indication of the Fano lattice:

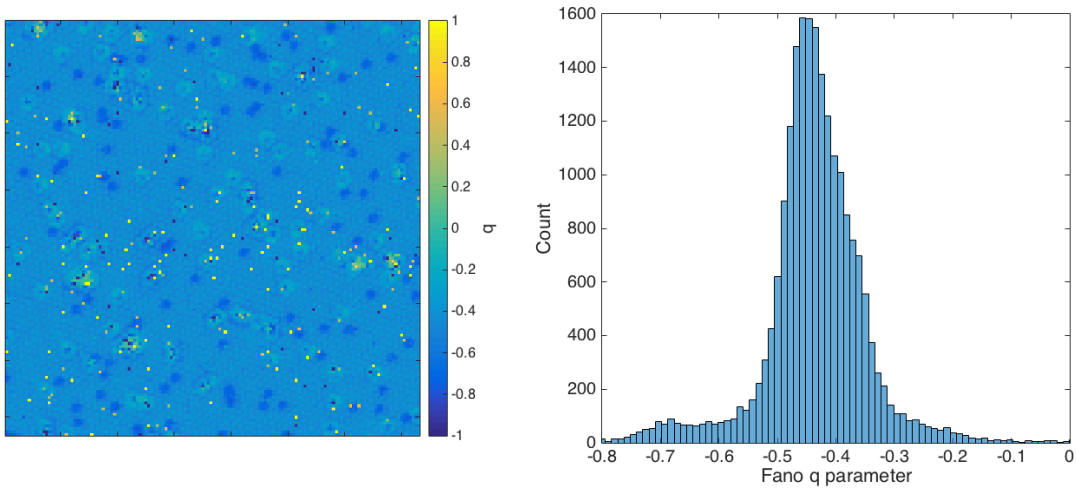

(a) (b)

Figure 4.10: a) Map of the fitted Fano parameter q and b) the histogram of those fitted values at 25 mK.

The median value of the Fano parameter q was -0.44, which is the ratio of probabilities of tunnelling into some localised state, most likely the uranium f-electrons, compared to the delocalised conduction band. The value of q varies with the atomic lattice, where it is greater (more positive, but smaller in magnitude) on the uranium sites and the opposite between uranium sites. Which is consistent with the idea that the Fano resonance comes about due to the interference between tunnelling to the conduction band and a channel to the heavy f-electron states then to the conduction band. One would expect the probability of tunnelling into the localised f-electron states to be greatest where the f-electron state is actually localised, i.e. on the uranium sites. Whilst naturally the tunnelling would decrease away from the sites, which in a lattice is the space in between. This demonstrates that the heavy fermion behaviour of UPt_3 is indeed associated with the uranium 5f-electrons, so much so to produce the telltale heavy fermion Fano lattice. A curiosity however is that where there are vacancy defects in the uranium lattice, as seen in the

topography in figure 4.9, there are enhanced q values (more positive) and also where there are superficial uranium atoms sticking above the background lattice, there is a reduced q-parameter. However, due to a slight lack of spatial resolution in the map, the Fano lattice is less clear in the spatial variation of the Fano resonance width Γ.

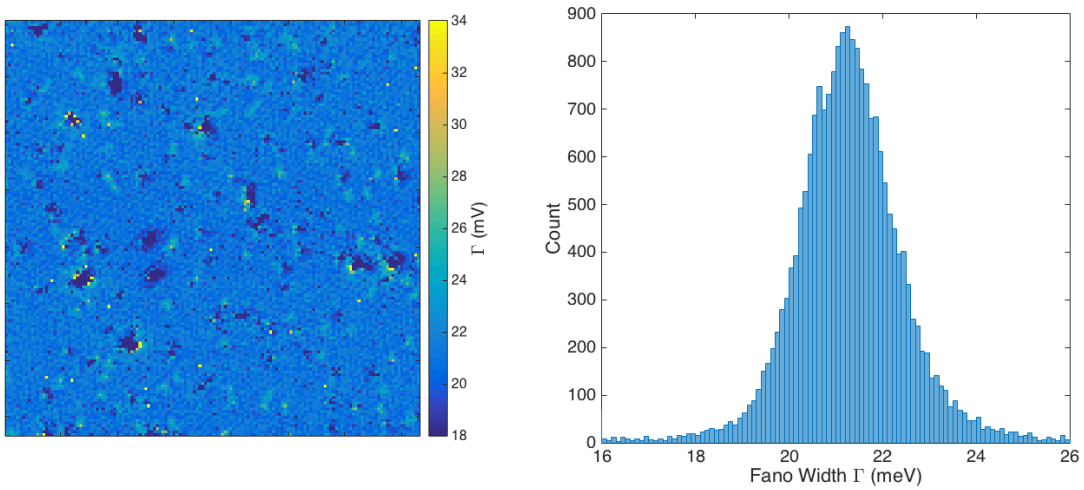

(a) (b)

Figure 4.11: a) Map of the fitted Fano width Γ values and b) the histogram of those fitted values at 25 mK.

The median fitted value of the Fano width Γ was 21.25 meV, which would correspond to a crude temperature scale ($k_B T^*$) of approximately 250 K; much higher than the ARPES derived Kondo temperature $T_K \sim 10$ K [99]. It is just about noticeable that the Fano width is greater on the uranium lattice and less in between. This Fano width is proportional to the hybridisation strength in the system, which would hint that the hybridisation is strongest on the uranium 5f-electron sites. In terms of the defects, the Fano width is greater on the superficial uranium atoms above the lattice and less in the vacancies. Which would make more sense if the hybridisation process were tied to the uranium 5f-electrons. This Fano width on the order of ∼20 mV is similar in scale to the 50 meV bandwidth of the uranium 5f states observed in high-resolution ARPES in work by T. Ito et al [98]. The two energy scales being so similar backs up the idea that the hybridisation with the uranium 5f electrons contributes to the Fano resonance.

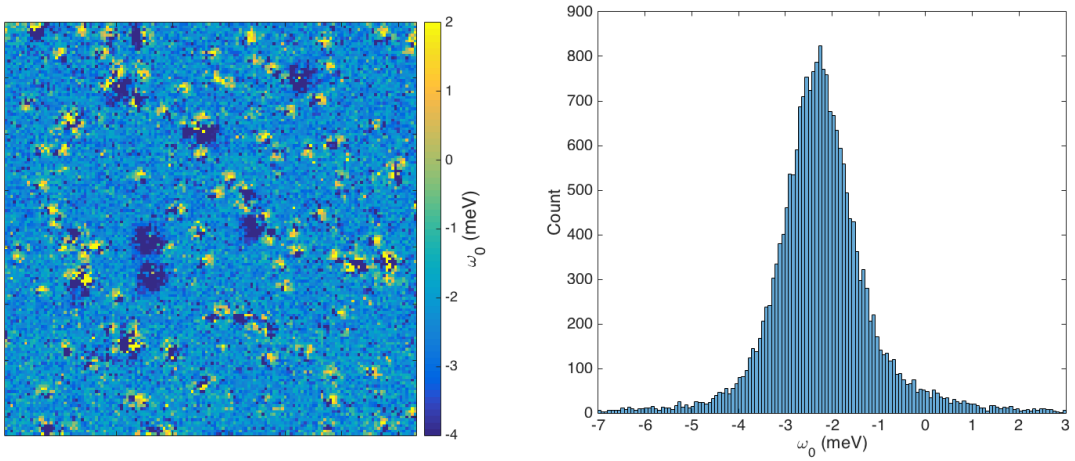

(a) (b)

Figure 4.12: a) Map of the fitted many-body state energy values, ω_0 and b) the histogram of the fitted values at 25 mK.

Last of all is the fitting of the many-body state energy, ω_0, which one suspects due to the lack of spatial resolution, does not reveal the Fano lattice. The median fitted value of this energy scale is -2.28 meV with there at least being variations on the defects of the lattice: This energy-scale reveals itself to be greater on superficial uranium atoms and lower on the vacancies. It would expected that if this were repeated with much greater spatial resolution, the Fano lattice would once again reveal itself, such as in URu_2Si_2 [96].

4.4.3 Magnetic Field Dependence

Since UPt_3 is known to be antiferromagnetic below 5 K, applying a magnetic field enables the probing of any AFM signatures that appear in the STS density of states or any other magnetic properties.

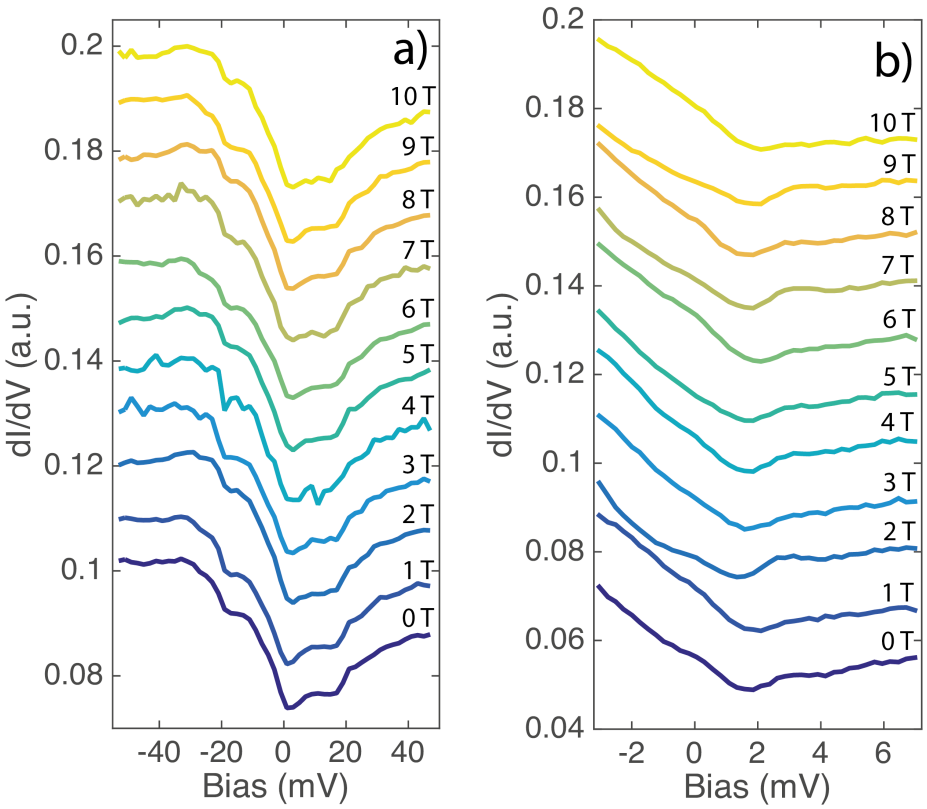

Figure 4.13: a) Field dependence of UPt_3 spectral features at 25 mK, using $V_s = 50$ mV, $I_s = 0.1$ nA and $V_L = 2$ mV. b) Field dependence of UPt_3 spectral features at 25 mK, using $V_s = 10$ mV, $I_s = 0.1$ nA and $V_L = 0.5$ mV. Both plots have their spectra offset vertically for clarity.

It can be seen in figure 4.13 that there is no noticeable influence of the magnetic field on the spectra in UPt_3. Although there is a slight introduction of noise in a couple of the spectra, especially the wider ranged spectra around 5 T due to increased turbulence from the helium boil-off from field ramping, which on occasion would not settle down quite a while after the field was left in persistent mode. Owing to its AFM order, there are spin-fluctuations in UPt_3 associated with an energy scale of 10 meV; observed in spin-polarised inelastic neutron scattering experiments by G. Aeppli et al [100] as well as Raman spectroscopy in work by H. Brenten et al [101]. One might expect that since there are the spin-fluctuations from the AFM order on the scale of 10 meV, that there could be a mean-field like gap of this scale. Whilst there does appear to be a gap-like feature between $\pm$ 10 mV in the spectra, there is neither any effect from the out-of-plane magnetic

field nor from temperature, since the feature appears at all three of the temperatures measured; surviving especially up to 8 K, comfortably above T_N. The fact that there is no influence from the magnetic field and that the spectral feature is unchanged above the AFM transition temperature heavily implies that either the signature of this AFM/spin-fluctuations is so weak that it was never distinguished in the first place and/or it is very robust with respect to out-of-plane applied field. Likewise the small pseudo-gap feature sat at 2 mV was unaffected by the applied magnetic field, ruling out its origin from anything magnetic or spin-fluctuation related.

4.4.4 Inelastic Tunnelling

It can be seen in many previous figures, figure 4.8 in particular, that there is a sharp upturn in conductance at 20 mV with a symmetric partner at -20 mV; and to a lesser extent, pairs of jumps at ±30 mV. These sudden jumps in conductance are symptomatic of inelastic tunnelling with a bosonic mode. Another way of visualising these jumps is to take the second-derivative of the current with respect to bias voltage, shown below:

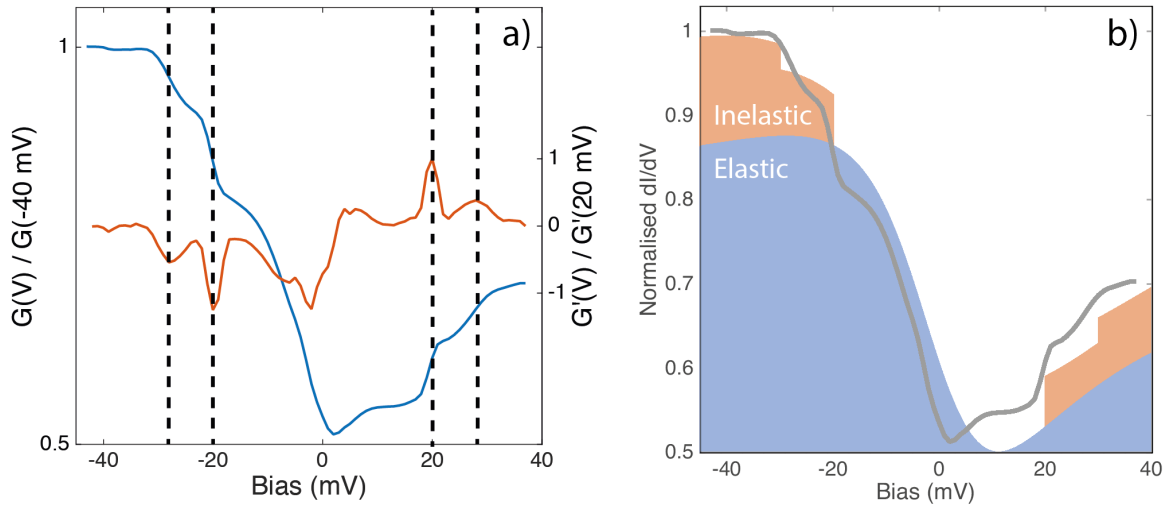

Figure 4.14: a) The same spectrum as shown in figure 4.8 a), alongside its derivative. The second-derivative of the current in orange reveals two well-defined peaks at ±20 mV and smaller ones at ±30 mV. b) Convolution model of the inelastic tunnelling through a 20 mV and 30 mV excitation with the background elastic conductance in blue and the inelastic contribution in orange. Underlying Fano resonance modelled on spectrum in figure 4.7a), with q = -0.62 and Γ = 17.9 mV. Left curve is imposed over the modelled spectrum for comparison.

These inelastic features were observed at all three temperatures measured: 25 mK, 2 K and 8 K; where the only difference spectroscopically was the increased sharpness of the jump at lower temperatures, as expected from thermal broadening. A way of modelling the inelastic tunnelling contributions is by considering the effect of a conduction pathway that only opens up at the excitation energy, $\hbar\omega$ [102][103]; this can be thought of as an excitation spectrum, $\chi(\omega)$, with delta functions at $\pm$20, 30 mV imposed over the Fano resonance background, $\rho(\omega)$, in a similar way to the modelling of the inelastic effects of spin fluctuations in the iron-based superconductor LiFeAs [41]:

$$G(V) = \begin{cases} G_{el.}(V) + A(V)_{inel.} \int_0^{eV} \mathrm{Im}\{\chi(\omega)\}\rho(eV-\omega)d\omega, & V > 0 \\ G_{el.}(V) + A(V)_{inel.} \int_0^{-eV} \mathrm{Im}\{\chi(\omega)\}\rho(eV+\omega)d\omega, & V < 0 \end{cases}$$

where $A_{inel.}$ is a scaling coefficient for the amplitude of the inelastic tunnelling contribution of an excitation at energy, $\hbar\omega$. This model is taken at zero-temperature without any thermal broadening effects on either the elastic or inelastic conductance. It can be seen in figure 4.14 that this produces the observed jumps in conductance seen in STS. For the figure shown, an inelastic contribution amplitude was set to 10% for the 20 mV excitation and 5% for the 30 mV excitation to match the jumps measured in spectroscopy. The fact that this model fits the spectroscopic data so well supports the inelastic tunnelling explanation of the conductance jumps in UPt_3 and therefore the role of bosonic modes.

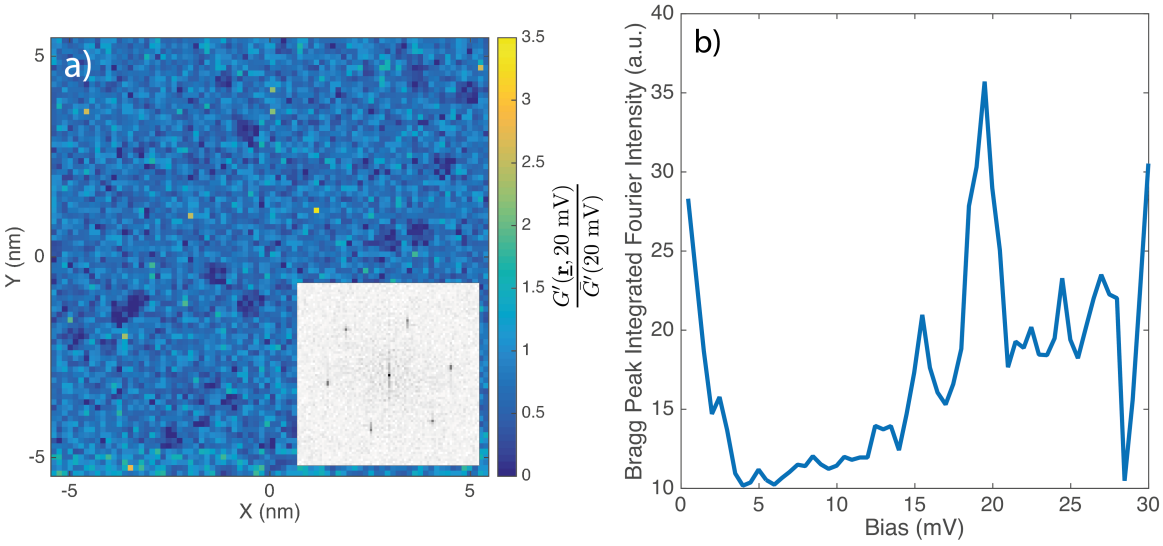

Figure 4.15: a) Spatial variation of the 20 mV peak in G', normalised to the mean peak intensity with an inset of its Fourier transform. Obtained using $V_s = 30$ mV, $I_s = 0.2$ nA and $V_L = 0.5$ mV. b) Integrated Fourier intensity of the Bragg peaks in the G' Fourier transformed maps as a function of spectroscopic bias.

When imaging the intensity of the second derivative of the current, in particular the peak at +20 mV, it can be seen that the intensity of the peak, so therefore a higher step up in conductance, appears to vary with the atomic lattice with maximum intensity on the uranium sites and minima in between them. Suggesting a link between the strength of the inelastic tunnelling and thus any electron-boson coupling and the uranium atoms. The intensity of the Bragg peaks in the second derivative G' map as a function of spectroscopic bias reveals that atomic corrugation in G' is most intense at 0 and 20 mV and broadly invisible between.

4.4.5 Phonon Signatures

Polarised Raman scattering experiments performed on single-crystals of UPt_3 by S. L. Cooper et al detected four of the five Raman-allowed phonons in a temperature range between 5 and 340 K [104]. The phonons did not appear to demonstrate any anomalous behaviour as many previous investigations had suggested; spin fluctuations were also detected using quasi-elastic scattering which showed a q-independent spin-fluctuation

relaxation rate [104]. In particular, a very strong signal was seen at 150 cm^{-1}, which from the geometry used in the experiment was identified as the A_{1g} breathing mode of Pt atoms, which propagates in the basal plane of UPt_3. This breathing mode phonon may be the same optical phonon mode seen in optical reflectivity measurements by F. Marabelli et al [105][106].

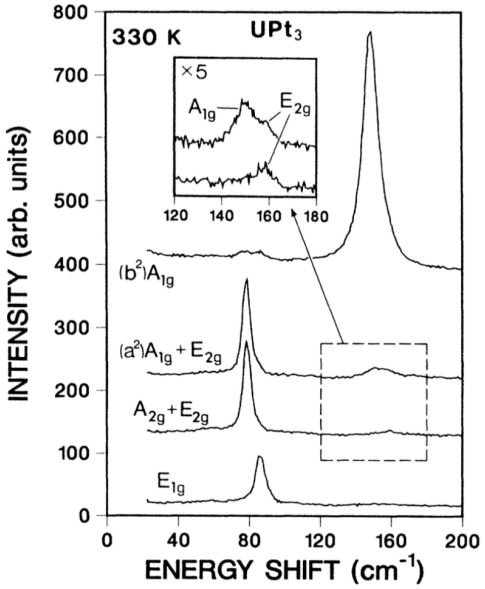

(a) Phonon spectra of UPt_3 at 330 K.

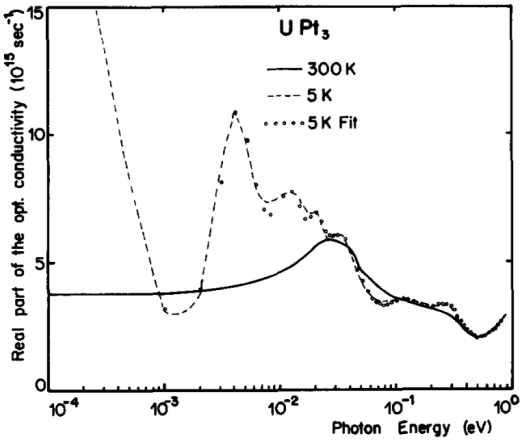

(b) Real part of the optical reflectivity of UPt_3 at 5 and at 300 K.

Figure 4.16: Figures taken from S. L. Cooper et al (left) [104] and F. Marabelli et al (right) [105] showing the presence of excitations at 20 mV, appearing as a 150 cm^{-1} in the polarised light spectra (Ramen) and as a peak in the real optical reflectivity. In addition the optical reflectivity measurements suggest a gap-like structure below 4 meV.

The A_{1g} Pt breathing mode phonon observed in both Raman scattering and optical reflectivity provides an explanation for the strong inelastic tunnelling signatures seen in the STS measurements in UPt_3. This phonon could provide an additional conductance channel at 20 mV, producing the sharp upturn seen in spectroscopy. The fact that these inelastic signatures appear as low as 25 mK and up to 8 K and in applied magnetic fields up to 10 T, demonstrate that these signatures have no relation to superconductivity or antiferromagnetism, since these effects have cut off temperatures defined by a critical superconducting temperature $T_c \approx 0.5$ K and Néel temperature $T_N \approx 5$ K and an upper critical field of approximately 2.2 T. UPt_3 has previously been associated with strong electron-phonon coupling and in particular strain coupling to itinerant electrons [107]; in

addition to the discovery of the strong pressure dependence, but largely pressure robust Fermi surface, of the (100) soft phonon mode in the conventionally superconducting and charge density wave (CDW) exhibiting atomic uranium [108]. The lattice dynamics of atomic α-uranium have been previously measured with inelastic neutron scattering [109] and more recently in Raman scattering [110]. Strong electron-phonon coupling as well as any potential surface effects of this A_{1g} phonon may strongly couple to the tunnelling electrons, providing an interesting link between the importance of the soft phonon mode in atomic uranium and its superconductivity and CDW order; and the unconventional superconductivity in UPt_3. Sr_2RuO_4, the sister p-wave candidate to UPt_3 was recently observed to have kink signatures associated with coupling to collective modes such as phonons [111], potentially linking strong phonon interactions in these strongly correlated compounds, their unconventional superconductivity and their p-wave candidacy.

According to BCS theory, the critical temperature T_c of a superconductor is proportional to the electron-phonon coupling by the simplified equation:

$$k_B T_c \simeq 1.13 E_D e^{-\frac{1}{N(0)V}}, \tag{4.1}$$

where E_D is the Debye cut-off energy, N(0) the electronic density of states at the Fermi level and V is the electron-phonon coupling potential [2][112]. One might expect that increased electron-phonon coupling would increase the superconducting critical temperature; but even though UPt_3 has already been established as an unconventional superconductor because of its Knight shift and AFM order, the high electron-phonon coupling it exhibits in elastic measurements and inferred from the strong phonon signatures seen in this work would appear to contradict the BCS relation. Where strong electron-phonon coupling is concomitant with a very low superconducting transition temperature(s) ($\sim$500 mK).

4.4.6 Pseudogap

At small bias voltages, a gap-like feature was observed centred just below 2 mV and of 4 mV width which persisted up to 10 T of applied field and visible at the two lower temperatures used in this investigation of 25 mK and 1.8 K. This observed gap-like structure is similar to the gap-like signatures seen in low energy and temperature optical reflectivity measurements by F. Marabelli et al [105][106], where heavy quasiparticles with effectives masses of the order of 250 free-electron masses were found at the Fermi energy in a band of 4 meV width. It was proposed that a second f-like band is observed 4 meV below the Fermi energy, producing a gap or pseudogap between both bands for an f-f inter-band transition [105]. Through these optical reflectivity measurements, they observe a peak at 4 meV as seen in figure 4.16 and a gap-like structure below [105].

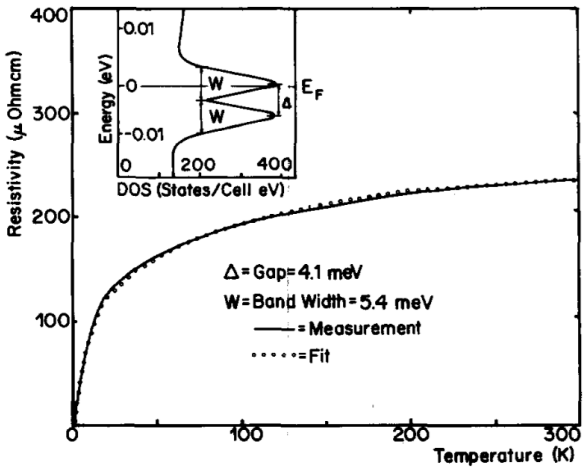

Figure 4.17: Resistivity of UPt_3 from [113], fitted with the Lorentz oscillator model by [106]. Insert shows the proposed band structure near the Fermi level for this f-f transition. Figure taken from [105].

Based on the idea that the pseudogap is formed from an f-f inter-band transition, a Lorentz oscillator model is utilised by Marabelli et al [106] to model the resistivity data previously measured by A. de Visser et al [113]. The fitting was very accurate at describing the temperature dependence of the resistivity, suggesting a pseudogap of 4.1 meV with a bandwidth of 5.4 meV [105]. The inset of figure 4.17 is a schematic of the f-f inter-band transition model as well as the main figure displaying the fitted resistivity data. This band structure has been calculated by N. Grewe in a Kondo resonance

model [114] and also by Brandow in a hybridisation model [115]. Under these models, the gap-like structure's robustness with temperature would potentially reveal its origin; with the Kondo-resonance model disappearing above a characteristic Kondo-temerature, T_K, and the hybridisation, as well as other models, remaining robust to higher temperatures. However, it is hard to gauge the temperature rigidity of such a small meV-scale feature in optical reflectivity and other low-energy techniques such as STS due to thermal broadening through the Fermi distribution; as well as quasiparticle scattering across this pseudogap [105]. High-resolution ARPES measurements by A. J. Arko et al determined UPt_3 to have a Kondo temperature on the order of $T_K \sim 10$ K, but also suggested that the single-impurity model that would produce a narrow singlet state close to the Fermi level was inconsistent with the ARPES data in UPt_3 [99].

In the measured STS data on UPt_3, the gap-like feature at 2 mV, as well as being robust with field and thus ruling out any potential magnetic origins, appears at 25 mK and 1.8 K and is no longer distinguishable at 8 K. However, like with optical reflectivity, STM spectroscopy is heavily influenced by thermal broadening through the Fermi distributions, it is difficult to conclude whether the feature disappears between 1.8 K and 8 K, which would suggest a Kondo-like temperature between these points; or whether the feature becomes simply washed out through thermal broadening. Since ARPES suggested a Kondo temperature on the order of $T_K \sim 10$ K, it is possible that the pseudogap feature from the f-f inter-band transition in Marabelli's optical reflectivity and STS in this work, could be explained by a Kondo-resonance as suggested by N. Grewe [114].

Alternatively, work by P. Wölfe et al suggests that when tunnelling into clean strongly correlated heavy fermion compounds, such as UPt_3, a Fano line-shape should appear with a characteristic width of $\sim 2T_K$ [26]. However since the spectroscopic feature at +2 mV is so weak, despite the predicted energy scale $2T_K \sim 2$ mV being quite agreeable; the much wider and stronger Fano resonance shape spanning ± 100 mV and with a typical width of the order 20 mV is a much more believable candidate for the Fano heavy fermion behaviour in UPt_3. This gap like signature seen in STS is also unlikely to be a gap associated with the AFM order, where $T_N \simeq 5$ K would produce a gap of the order of

~1 meV width, far less than the 4 meV spanning gap structure observed.

4.4.7 Quasiparticle Interference

In addition to simply investigating the line-shape at each pixel in a map, such as to see the Fano lattice, the conductance data at each bias-layer was used to probe the quasiparticle response to see if any significant quasiparticle interference (QPI) signals are visible; which could shed light on the materials underlying band structure. Due to tip and STM instabilities from debris being moved around the sample surface or from changes in helium recovery line pressure, the spectroscopic data was affected, limiting QPI q-space resolution. A QPI map is analysed and presented below:

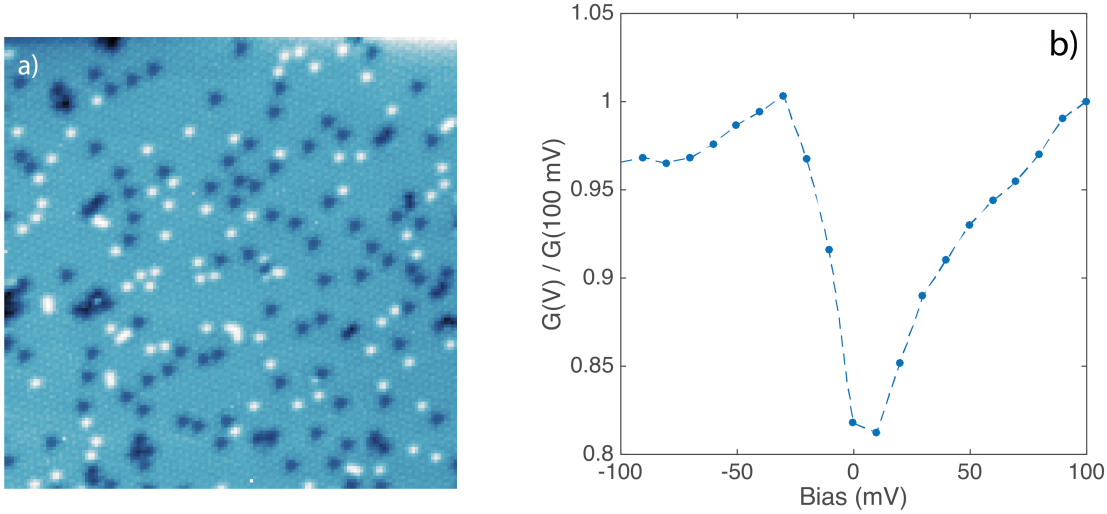

Figure 4.18: a) Topograph and b) averaged spectrum output of the QPI map, obtained over a $(25\ \text{nm})^2$ area, with $V_s = 100$ mV, $I_s = 0.1$ nA and $V_L = 5$ mV. There were 21 bias layers and 140 by 140 pixels resolution.

It can be seen in figure 4.18 that the topography output displays atomic resolution and the averaged spectrum over this wide ± 100 mV range follows the generic Fano shape discussed earlier.

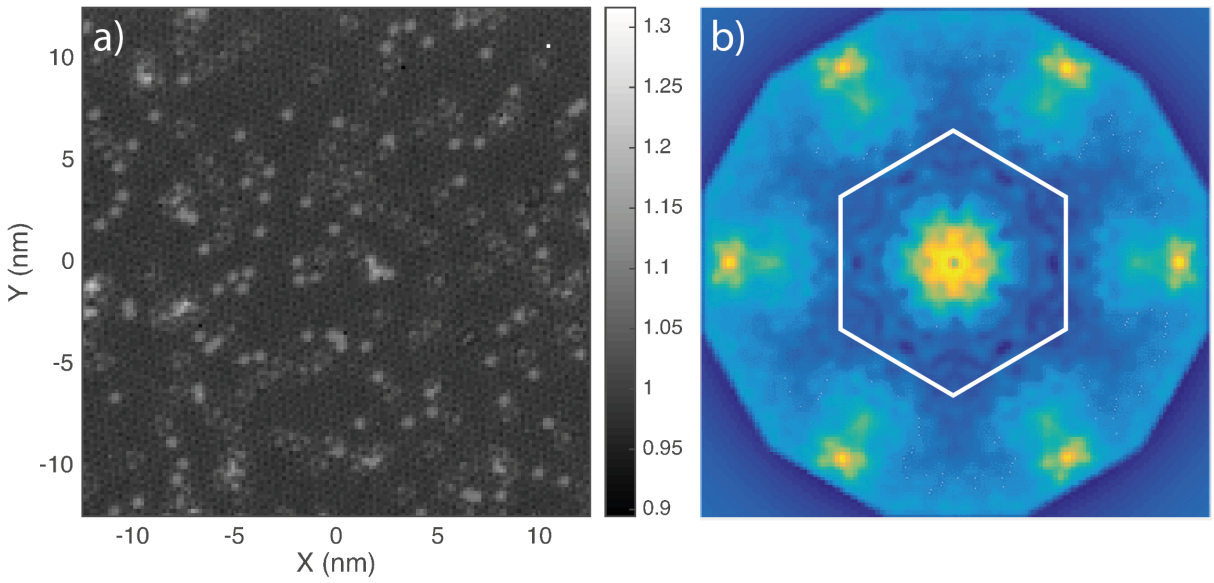

Figure 4.19: a) The QPI response of UPt_3 at zero-bias shown as firstly the conductance map and b) its symmetrised and flattened Fourier transform with the first Brillouin Zone shown as a hexagon.

From looking at the conductance layers, such as the zero-bias layer in the figure above, the QPI signal was not strong enough to be visible in the real space image. However, Fourier transforming these conductance layers and then to improve the signal-to-noise, the data is symmetrised. Symmetrising is achieved by folding the Fourier transformed image along each of its high-symmetry directions, which for a triangular lattice are the direction toward the atomic spots and thirty degrees away from this. For visual clarity, an identical Lorentzian is then subtracted from each of the FFT images to flatten the output, to help bring out any defining features. So whereas the zero-bias conductance map did not reveal much of a QPI response, the FFT of this layer displays some promising features as well as the reciprocal lattice Bragg points. A simplified two-dimensional model Fermi surface of UPt_3 is then shown in figure 4.20 as well as its autocorrelation to simulate QPI, by adapting the dominant in-plane Fermi surface orbit from dHvA experiments by G. J. McMullan et al, the quantum oscillations of magnetisation [89]. The Fermi surface is first designed to be of a simple 6-fold symmetric form of:

$$k = k_F + k_1 \cos 6\theta \tag{4.2}$$

The phase is adjusted so that maxima in the Fermi surface wave-vector point along Γ-M. The area of this Fermi surface is then:

$$A = \pi(k_F^2 + \frac{k_1^2}{2}) \tag{4.3}$$

To aesthetically match the commonly theorised Fermi surfaces of UPt_3, featured in the same dHvA work, k_1 is chosen to be 20% of k_F, leading to a Fermi surface area of:

$$A = \pi k_F^2(1 + \frac{1}{50}) \tag{4.4}$$

$$A \simeq \pi k_F^2 \tag{4.5}$$

with only a 2% error in the Fermi surface area. The dHvA magnetisation oscillations showed a dominant frequency, F, at ∼6 kT [89] for magnetic fields applied parallel to the c-axis. The Fermi surface area is related to the quantum oscillation frequency by the standard formula [116]:

$$F = \frac{\hbar}{2\pi e}A, \tag{4.6}$$

which for a frequency of 6 kT corresponds to a Fermi surface area of $\simeq 0.573$ Å^{-2}. Using the approximation for the idealised Fermi surface, the Fermi wave-vector is therefore approximately $k_F \simeq 0.427$ Å^{-1}. The wave-vector for the model Fermi surface is then fixed at this value and plotted below with its autocorrelation:

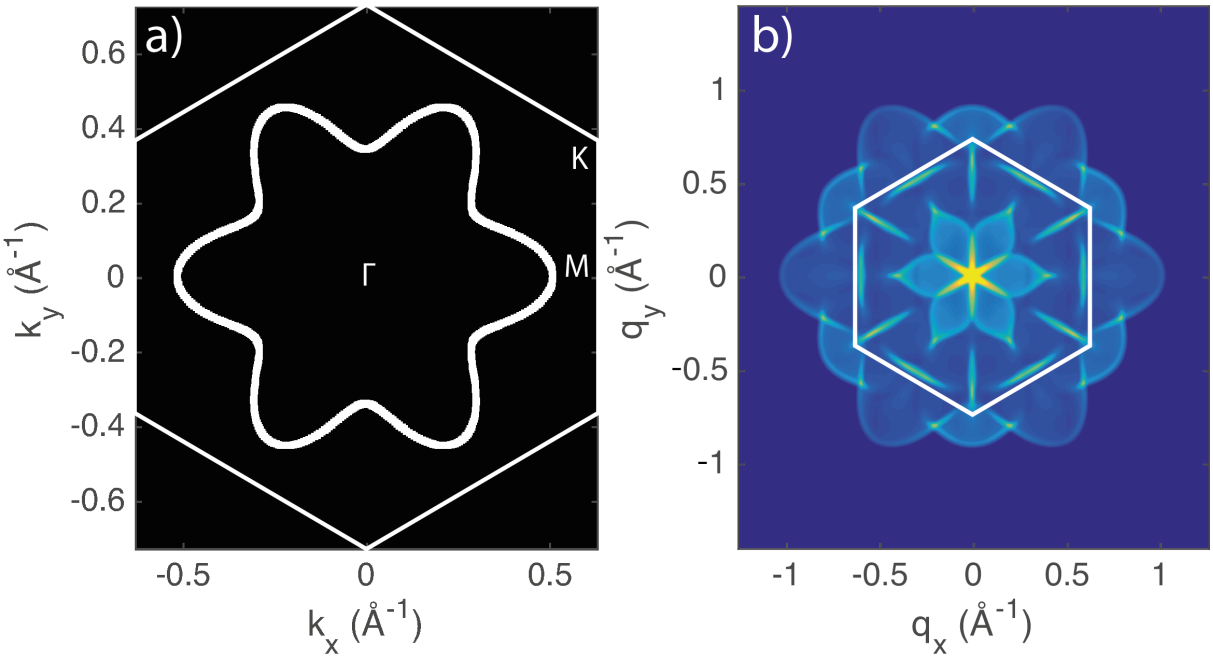

Figure 4.20: a) Idealised Fermi surface of UPt_3 and its autocorrelation b). Fermi surface area derived from dHvA experiments with the magnetic field along the c-axis [89].

Comparing the autocorrelation in the figure above with the zero-bias QPI in figure 4.19, there is some similarity in the q-space structure inside the first BZ. The bright star-shape in the centre, elements of the petal structure and the flat edges along the BZ limits can be reasonably recognised in the zero-bias QPI, suggesting that this quasiparticle response is not merely an artefact of the image processing, but quasiparticle scattering off a 6-fold symmetric Fermi surface band.

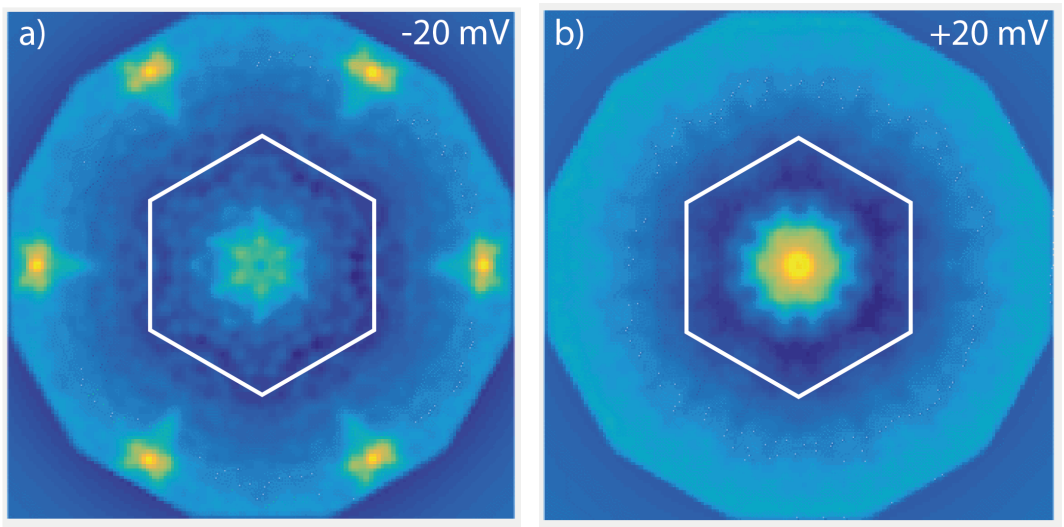

Figure 4.21: Symmetrised and flattened QPI images at the inelastic steps at a) -20 mV and b) +20 mV.

The inelastic tunnelling phonon signatures discussed earlier, with their steps at ±20 mV did not produce anything unusual in the QPI, except that the atomic Bragg points were not visible in the +20 mV image, but were visible at -20 mV.

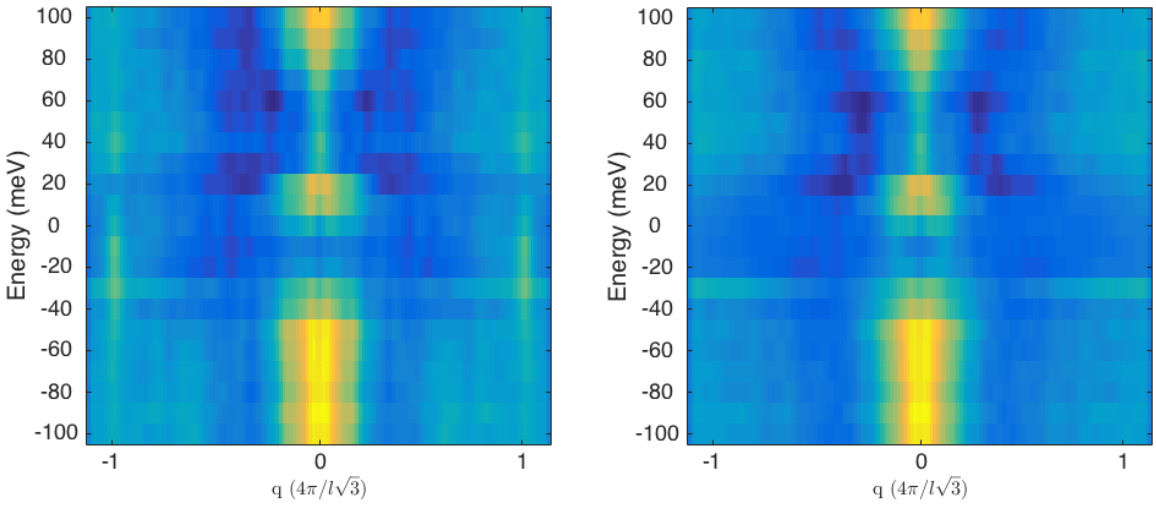

(a) Γ-M (b) Γ-K

Figure 4.22: QPI dispersion obtained as line-cuts along the two high-symmetry directions: Γ-M and Γ-K.

Taking cuts through the QPI images at each bias-layer along both of the high-symmetry directions allows one to visualise the dispersion of the underlying band structure. In figure 4.22 the atomic Bragg spots can be seen along the Γ-M direction as expected, but with varying intensity as a function of bias. In addition, an issue with displaying this data in this fashion is that the raw conductance at each bias follows the overall Fano line-shape, and therefore falls to a fairly deep minimum at zero-bias; therefore the Fourier intensity is likewise affected, introducing unwanted contrast across bias voltages as opposed to what is really wanted in q-space. The dispersion was then extracted by manually tracking the peaks at each bias layer:

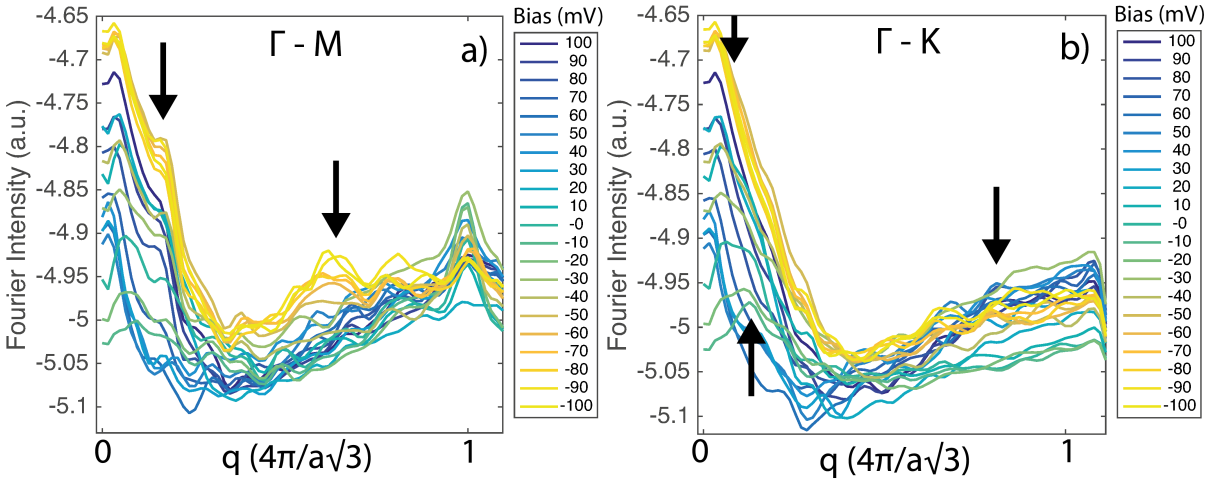

Figure 4.23: Extracted line-cuts at each bias-layer along both high-symmetry directions. The signatures indicated with arrows are the q-vectors found to disperse most consistently. Profiles are from the logarithmic and Lorentz subtracted QPI images, producing the negative amplitudes here.

There are a couple of visible peaks in the q-space cuts; in each of the two high-symmetry directions, the two q-vectors which most consistently tracked with bias are indicated with black arrows.

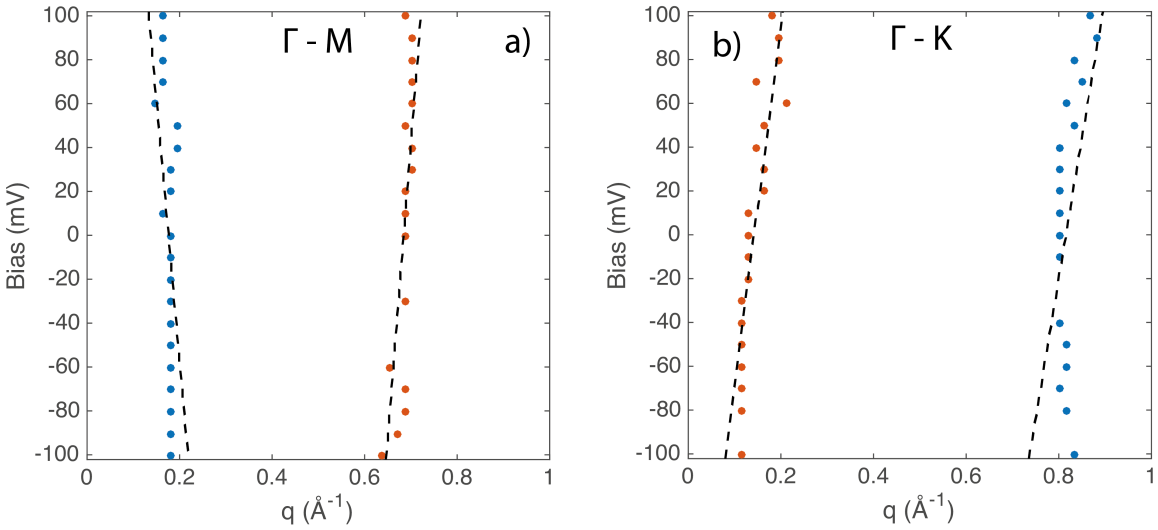

(a) Γ-M (b) Γ-K

Figure 4.24: Dispersion of the two selected q-vectors along both high-symmetry directions, plotted alongside a linear fit.

Plotting the q-vector location of the peak as it appears to change with bias produces the much simpler dispersion plots above. Along the Γ-M direction the first q-vector appears

hole-like, however its linear fit is probably the least convincing compared to the other three q-vectors tracked. It is possible to estimate the effective masses of these q-vectors or underlying bands, by considering a simple model where the quasiparticle scattering vector q s simply twice the k-vector of the underlying band structure:

$$q \approx 2k. \tag{4.7}$$

Then, simply using the traditional effective mass formula with a slight rearrangement, the effective mass in terms of this scattering vector q is given by:

$$m^* \approx \frac{\hbar^2 q_F}{4\frac{\partial E}{\partial q}|_{q_F}}, \tag{4.8}$$

where q_F is the length of the q-vector as it crosses the Fermi level. Likewise, the band edge can be approximated in a parabolic model by evaluating:

$$E_{\text{edge}} \approx -\frac{q_F}{2}\frac{\partial E}{\partial q}\bigg|_{q_F} \tag{4.9}$$

Applying this model to the four 'bands' extracted above, the effective masses at their Fermi q-vectors are displayed in the table below:

	$q_F/\text{Å}^{-1}$	m^*/m_e	Band Edge (meV)
$q_{1,M}$	0.1759	-0.1414	208.5
$q_{2,M}$	0.6844	0.4849	-920.0
$q_{1,K}$	0.1422	0.1653	-116.5
$q_{2,K}$	0.8155	1.2127	-522.4

Table 4.1: Extracted q-vectors at the Fermi level and an approximation of the effective masses for the dispersing vectors.

The extracted effective masses produced are unexpectedly small for such a material that is so well known for its heavy fermion character. The meaning by the minus sign on the first q-vector simply indicates it is a hole-like band as opposed to electron-like. High-resolution ARPES measurements, as briefly mentioned early in the work by T. Ito et al, observed the uranium 5f states in a narrow band close to the Fermi level with a

bandwidth on the order of the experimental resolution of ∼50 meV [98]. These ARPES measurements saw deeper Pt 5d bands in good agreement with calculations, with typical band edges around -500 meV for their hole-like bands around the Γ high-symmetry point. Also observed were flat non-dispersive bands close to the Fermi level at roughly -50, -250 and -400 meV; attributed as satellite structures produced by strong electron correlation effects and renormalisation of the uranium 5f electrons. Previous de Haas-van Alphen measurements (dHvA) by G. J. McMullan et al [89] saw much greater effective masses on the order of tens to hundreds of free electron masses; as well as discussing the itinerant model calculations, which whilst they were smaller than the dHvA measured masses, were still far heavier than the masses estimated in QPI. Taking into account only the bands with orbits in the basal plane (therefore the oscillations of those would be seen in STS-QPI), which are labelled in G. J. McMullan et al's work as η, α_4', α_4 and γ', which correspond to various orbits on their 'octopus' Fermi surface for the first three and the latter a central orbit around the spherical Fermi surface, dubbed the pearl; it is wise to compare these masses with what was extracted from QPI. Those two fermi surfaces seen in the work by G. J. McMullan et al's were consistent with previous measurements by L. Taillefer et al [88] and N. Kimura et al [117].

Band Label	Plane	m^*/m_e	m_{band}/m_e
η (Octopus)	(a-b)	(130 ± 20)	13.0
α_4' (Octopus)	(a-b)	(110 ± 30)	8.0
α_4 (Octopus)	(a-b)	(80 ± 20)	4.2
γ' (Pearl)	(a-b) and (b-c)	(16 ± 30)	1.9

Table 4.2: In plane effective masses obtained from G. J. McMullan et al's dHvA investigation [89], alongside the fully itinerant model calculations for newly observed dHvA orbits.

G. J. McMullan et al's work suggested that the existing and new experimental evidence showed that all three uranium f-electrons in UPt_3 are delocalised and that the partially localised model, that assumes two 5f-electrons per uranium atom are localised [89], disagrees too much with the experimental data. The effective masses extracted from QPI are very small, especially for a heavy fermion compound and especially compared to the established dHvA measurements. However the extrapolated band edges from these dis-

persive features in the QPI yield sensible and consistent values with those measured in ARPES. Yet since the effective masses are so low for directly inferred values, as opposed to the extrapolation used for the sensible band edges; it would be unwise to fully trust the band edge values when the masses are so inconsistent with decades of research.

Therefore it is from this that it can be concluded that the QPI data proved inconclusive, since if such small effective masses were to be believed, it would imply almost massless-like behaviour, akin to the electrons in Dirac cones such as those in graphene. Since the signals in QPI were so weak, it proved very difficult to identify peaks in q-space to track with bias; and those q-vectors chosen could perhaps be something inherent in the signal noise, which when folded in the symmetrisation process, appears as something real. Since UPt_3 has such a complicated band structure at the Fermi level, with a large number of Fermi surfaces in the heavy fermion state of UPt_3, again alluded to by G. J. McMullan et al [89]; it is unsurprising that QPI produced such a weak and complicated signal. The weak QPI response is perhaps somewhat surprising since having $\sim$10% of the surface as defects sites should provide strong QPI signatures. There may be a reasonable QPI response present, but washed out from all the band contributions, especially since the Fermi surface of UPt_3 is very three-dimensional; something that extra q-space resolution could perhaps resolve by measuring over much greater areas on a cleaner cleaved area that would allow it.

4.5 Conclusion

UPt_3 was found to cleave successfully despite having no natural cleavage plane to follow, producing a surface with patches of atomically flat uranium terminated areas. The only defects seen in STM were vacancies in the uranium lattice and superficial uranium atoms which sat directly above a uranium site. Step edges were often seen which would step down one atomic layer and with a uranium termination. Spectroscopically UPt_3 was measured to behave as a typical heavy fermion material in STS, where it's spectral structure followed that of a typical Fano line-shape, with little variation from 8 K down

to 25 mK; where it was fitted with a Fano width of 17.9 meV and an asymmetry q-factor of -0.61. Similar to work on URu_2Si_2 [96], the Fano parameters Γ, q and ω_0 varied across the material surface, with atomic variation visible in q and Γ, pointing towards preferred tunnelling through the localised f-states of the uranium sites on the uranium atomic sites as well as increased hybridisation strength.

At 25 mK no signatures of superconductivity were observed, suggesting that superconductivity is suppressed at the surface; either a side effect of it being potentially a p-wave superconductor or that it behaves similar to URu_2Si_2 which did not see direct evidence of the superconducting gap [92]. Sitting 2 mV above the Fermi level and with an overall width of 4 mV, was a gap-like structure consistent with the pseudogap seen in optical reflectivity measurements, thought to be an f-f inter-band transition [105]. The energy scale of this gap-like structure is consistent with the known 10 K Kondo temperature of UPt_3, which could mean that the phenomenon is explained as a Kondo resonance, as suggested by N. Grewe [114].

Strong signatures of inelastic tunnelling were observed in the spectroscopy, with large step-like jumps in conductance at $\pm$20 mV and $\pm$30 mV. The intensity of these conductance jumps, measured by mapping the peak in the second derivative of the current, varied with the atomic lattice and suppressed at defects. These inelastic signatures are consistent with the known phonon spectra in UPt_3, where in particular there is a very strong A_{1g} breathing phonon of the Pt atoms at 20 mV [104]. Such strong jumps in conductance suggest strong electron-phonon coupling, a fact already known from other techniques. Interestingly strong electron-phonon coupling is concomitant with weak superconductivity, since the transition temperatures are around 0.5 K. There was no evidence of antiferromagnetic phenomena and there were no spectral changes as magnetic fields of up to 10 T were applied, far above the superconducting critical field.

Quasiparticle interference measurements did not see any strong quasiparticle signatures on the real-space surface and Fourier imaging did not see any strong modulation peaks within 100 mV of the Fermi level. Careful analysis of line-cuts of symmetrised QPI data did find weak dispersing features which gave low effective masses. These low mass quasiparticles contradict the vast background of research that point to the heavy fermion behaviour in UPt_3, suggesting that these could be lighter and never before seen surface state bands. However the band edge estimates, assuming parabolic dispersion around the Γ point, were consistent with high-resolution ARPES measurements of the heavy bands in UPt_3 [98].

Further work to establish the superconducting nature of UPt_3 is warranted, to assess whether the surface superconductivity is truly suppressed or whether it was an issue with sample quality. Up to date RRR measurements are due to be carried out to check the sample quality of UPt_3 used in this work, but higher quality samples should also be measured to see whether it is consistent. More successful cleaves with larger untarnished atomically flat planes would allow greater q-resolution in QPI, to establish whether the quasiparticle dispersions are heavy or not, or if more clear signatures of QPI modulations could be seen. The superconducting gap or its suspected p-wave behaviour is yet to be convincingly shown, similarly with its sister p-wave candidate Sr_2RuO_4, where the superconducting nature remains unclear with noticeably strong phonon effects.

Chapter 5

Superconductivity and Topological Surface States in $PdTe_2$

5.1 Background

$PdTe_2$ belongs to the Transition Metal Dichalcogenide (TMD) family of materials, with a compositional formula MX_2, where M is a transition metal element from group IV, V, VI, VII or IX; whilst X is a chalcogen atom. TMDs have attracted a lot of interest in recent years because of their potential for small scale electronic devices. Structurally they are very similar to graphene, which itself lacks a band gap; however when produced as semiconducting monolayers, the TMDs have direct band gaps; as well as strong spin-orbit coupling [118]. There are about sixty TMDs and around two-thirds of them form layered structures in a X-M-X formation [119]; where the chalcogen atoms lie in two hexagonal planes which are separated by a plane of metal atoms. The TMDs have been found to cleave down to less than 1000 Å [119], making them ideal building blocks for fabricated electronic devices. The layered structures of TMDs are weakly held together in bulk crystals and vary in stacking order and metal atom coordination. TMDs can vary in electronic properties depending on their constituent elements, that range from semiconducting behaviour in ReS_2 [120] to simple metallic behaviour in $NbTe_2$ and $NbTa_2$ [121], but additional phenomena such as superconductivity and charge-density wave formation

in NbS_2 and $NbSe_2$ [122][123].

$PdTe_2$ is an intermetallic, layered compound in the TMD family, with the tellurium atoms positioned in an octahedral coordination; and is known to exhibit superconductivity and Pauli paramagnetism [119]. $PdTe_2$ has lattice parameters of a = 4.0365 Å and c = 5.1262 Å[124] and its crystal structure is shown in the figure below:

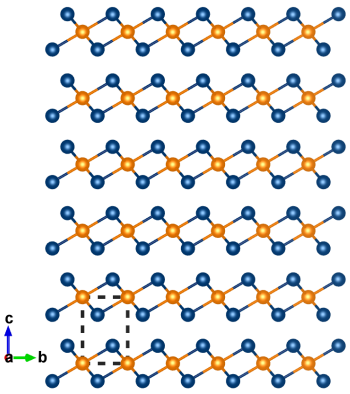

(a) Layered structure of $PdTe_2$.

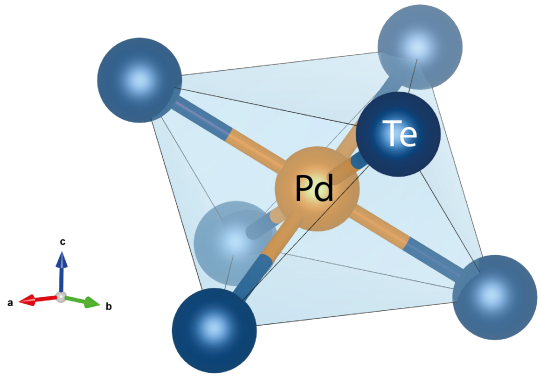

(b) Crystal structure of $PdTe_2$

Figure 5.1: Crystal structure of $PdTe_2$, where Pd atoms are shown in orange and Te atoms in blue; with a) showing the layered structure of $PdTe_2$ alongside the unit-cell in the dashed rectangle and b) a smaller representation demonstrating the triangular lattice of the upper termination of Te atoms.

$PdTe_2$ is a superconductor below 1.7 K [125], with recent experiments involving the intercalation of Cu atoms between its traditional $PdTe_2$ layers in the Cu_xPdTe_2 system boosting its T_c to a maximum of 2.6 K at an intercalation of 5% [126]. In a small subset of the TMDs, using group X elements as the transition metal, the sulphur and selenium compounds are semiconducting with a gap of ∼0.4 eV and diamagnetic; whilst the tellurides are metallic and paramagnetic, with $PdTe_2$ being the sole superconductor [127]. The superconductivity in $PdTe_2$ has been shown to be anisotropic in resistivity measurements in field which demonstrated that the superconductivity survives up to applied fields of 2000 Oe when the current is measured perpendicular to the c-axis; whereas it is almost entirely suppressed at 500 Oe measured parallel to the c-axis [128]. It has a sibling compound PdTe which is also a superconductor, with a T_c = 4.5 K, which is thought to be a strongly coupled superconductor thanks to a large jump in heat capacity

and gap-to-critical-temperature ratio [129].

$PdTe_2$ has been observed to support a type-II Dirac cone, which has been seen experimentally as a small circular hole pocket from in-plane Fermi surface measurements. Along the k_z direction, the same state is strongly tilted due to the type-II nature [130]. The hole pocket was also found to have topologically non-trivial Berry phase in dHvA experiments, confirming $PdTe_2$ as a type-II Dirac semimetal [128]. A type-II Dirac cone differentiates itself from a type-I Dirac cone by instead of merely being a linearly dispersing cone at the Fermi level, the type-II version is strongly tilted in k-space, violating Lorentz invariance and emerges at topologically protected touching points between electron and hole pockets [131]. This type-II Dirac cone has gone on to be considered a ubiquitous example of phenomena that result from a single orbital manifold in the transition-metal dichalcogenides; additionally supporting the presence of type-I bulk Dirac cones as well as topological surface states (TSS). This cornucopia of topological physics is hypothesised to be the direct result of a single p-orbital manifold in a trigonal crystal field and has been demonstrated in several TMDs [131][132][130]. Density-functional theory calculations and ARPES measurements have proven the existence these type-I and type-II three-dimensional bulk Dirac fermions and the topological surface states. The topological phenomena in $PdTe_2$ derive from the Te chalcogen-derived p-orbitals where protected band crossings and hybridisation produce tilted bulk Dirac cones, inverted band gaps (IBG) and spin-polarised topological surface states [130]. These spin-polarised topological surface states at the Fermi level are mediated by this inverted band gap, which itself is well above the Fermi level; producing a multi-valley Fermi surface with a chiral spin texture [133].

The presence of both spin-polarised topological surface states and superconductivity offers a chance to explore their interplay and whether the superconductivity could itself be of topological nature. It is believed that one way to achieve topological spin-triplet superconductivity would be through the spin-polarised surface states in Dirac semi-metals, such as $PdTe_2$, that would allow orbital mixing, to produce topologically non-trivial su-

perconductivity of Cooper pairs that have different quantum numbers [134]. Or whether like in the non-centrosymmetric compound BiPd where Dirac surface states with a helical spin texture turned out to coexist with topologically-trivial ordinary s-wave superconductivity [135]. Another route suggested was to couple the superconductivity of one material with the topological surface states of another material through the proximity effect, such as in the coupling of superconductors with topological insulators such as HgTe [136][137] and Bi_2Se_3 [138][139][140].

Recent magnetisation and AC susceptibility measurements suggest that $PdTe_2$ behaves as a type-I BCS superconductor in the bulk with a very large Meissner effect [141]. In addition, it was found that surface superconductivity is much more robust in field, with an upper critical field of the order $\sim$35 mT but with a lower critical temperature of $\sim$1.33 K. Resistivity revealed a much higher critical field of $\simeq$300 mT, producing a phase diagram that is similar to the non-centrosymmetric superconductors $LaRhSi_3$ [142] and AuBe [143], which are believed to experience a magnetic field induced transition from type-I to type-II superconductivity at low enough temperatures; an effect that is possible when the ratio of the penetration depth to the coherence length is close to $1/\sqrt{2}$ [141]. Whether this surface superconductivity is of topological origin is unknown thus far and is investigated in this thesis.

5.2 Normal State

5.2.1 Topography

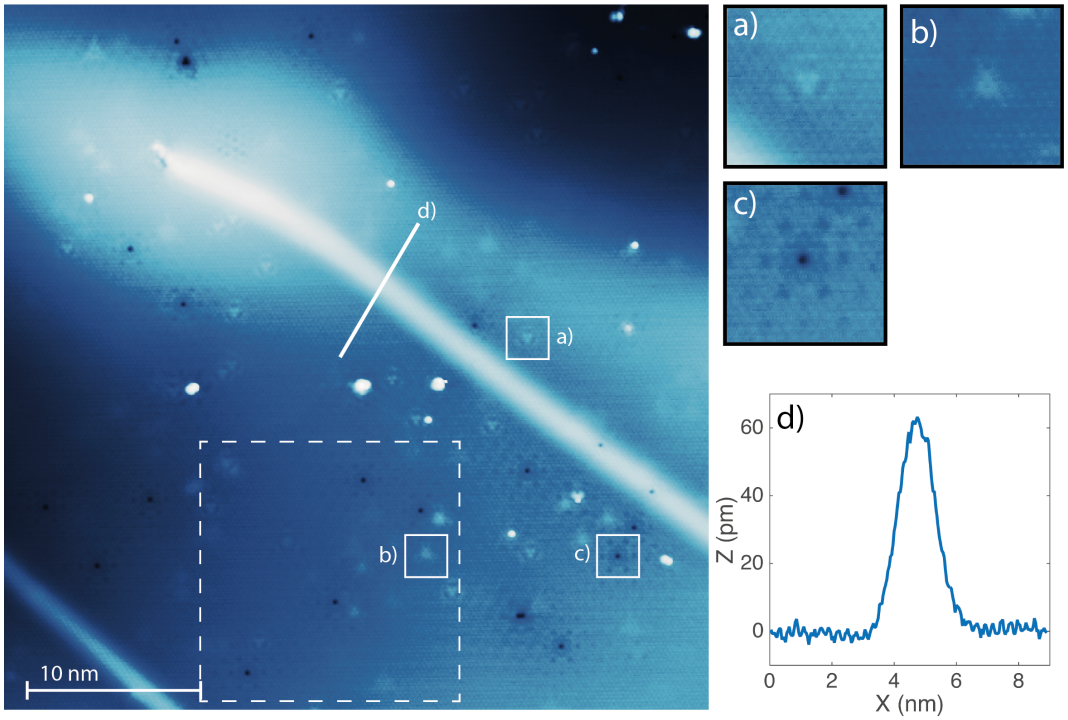

Figure 5.2: Topography of $PdTe_2$ taken at T = 8 K , using V_s = -10 mV and I_s = 0.2 nA set-point values over a $(40\ nm)^2$ area. Contrast enhanced non-linearly to aid the eye to various features seen on a typical $PdTe_2$ surface. Three of the typical surface defects are labelled and expanded as a,b,c). The dashed box is for the zoomed in surface on the proceeding figure. d) Shows a line-cut across the surface streak.

The $PdTe_2$ samples were provided by the King group at the University of St Andrews, grown by chemical vapour transport from the same batch used in recent ARPES measurements [130][133]. The surface of $PdTe_2$ revealed topographies that show the triangular lattice of the Te termination atoms. There are many types of defects visible on the surface of $PdTe_2$, including: vacancies of missing Te atoms with visible triangular modulations surrounding them, streaks of enhanced density of states which appear as smoothly raised wisps in the topography and triangularly symmetric shapes with small halos around them or star-like spikes.

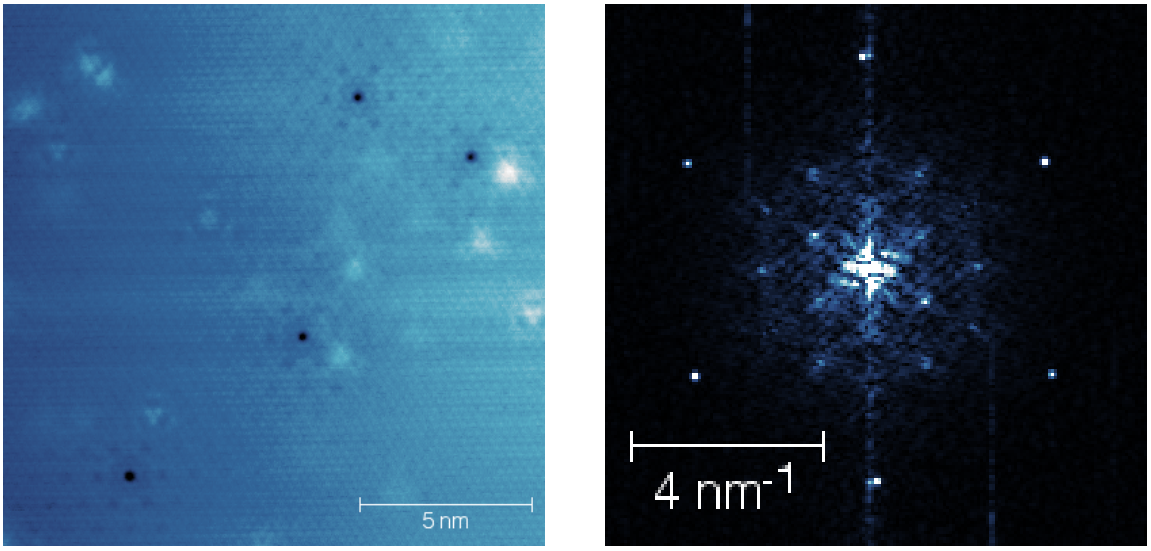

(a) Cropped topography. (b) FFT of cropped topography.

Figure 5.3: Cropped topography from figure 5.2 with its Fourier transformed image.

Cropping the topography in figure 5.2 makes it much easier to see the pronounced modulation surrounding the vacancy defects in the $PdTe_2$ surface. The Fourier transform of this cropped topography shows the strong peaks associated with this modulation and the other quasiparticle signatures inherent on the surface.

5.2.2 Normal State Spectroscopy

Spectroscopy in the normal state of $PdTe_2$ at 8 K reveals a density of states spectrum which resembles a flat terrain with strong resonant peaks. It can be seen that there is a strong peak at ∼-120 mV and an even more intense twin peak structure around the Fermi level, that is split into two peaks at ∼-10 mV and ∼4 mV. The relative intensities of these features was found to be both tip and surface dependent, perhaps hinting towards a potential surface state nature of these features as opposed to a presumably more robust bulk phenomena.

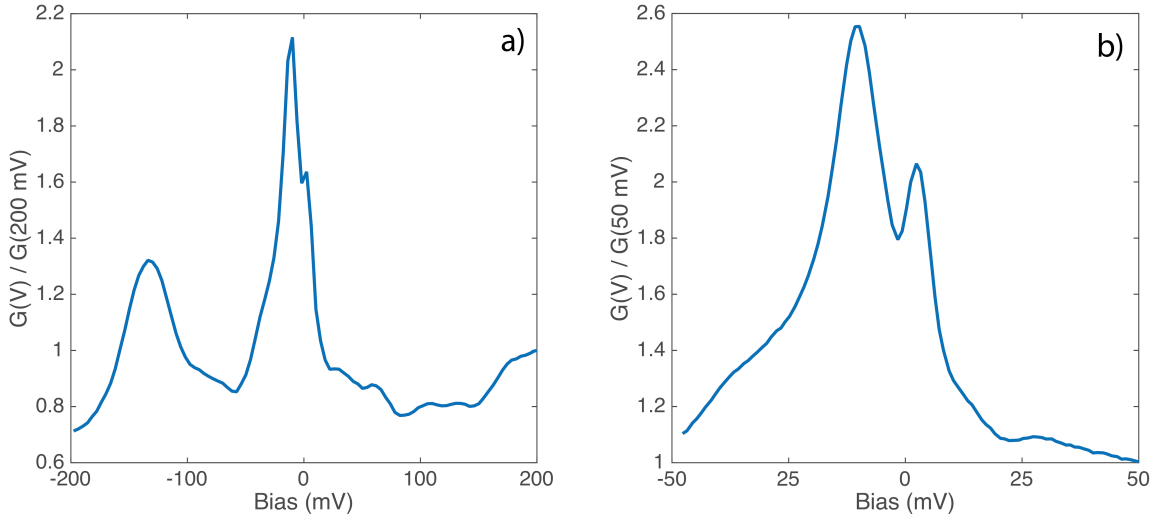

Figure 5.4: Representative spectra of $PdTe_2$ at 8 K, taken as averages of 64 individual spectra over a $(3\ nm)^2$ area. a) resolved using $Vs = 200$ mV, $I_s = 0.1$ nA and $V_L = 5$ mV and b) $V_s = 50$ mV, $I_s = 0.1$ nA and $V_L = 2$ mV.

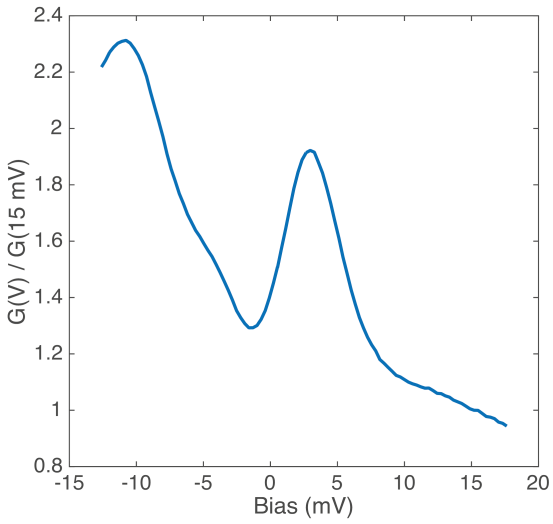

Figure 5.5: Average spectrum of $PdTe_2$ at 8 K, taken as the average of of 64 individual spectra over a $(3\ nm)^2$ area, using $V_s = 15$ mV, $I_s = 0.1$ nA and $V_L = 0.6$ mV.

5.3 Superconductivity

5.3.1 Superconducting State Spectroscopy

Spectroscopy in the superconducting state of $PdTe_2$ at 40 mK reveals the same peaked structure as that of the normal state, however with another even more intense peak around ∼200 mV, which may be a tip effect from changes in nanostructure from changing temperature and location. The original twin peak structure at the Fermi level is now accompanied by two further sub-peaks of a very narrow width.

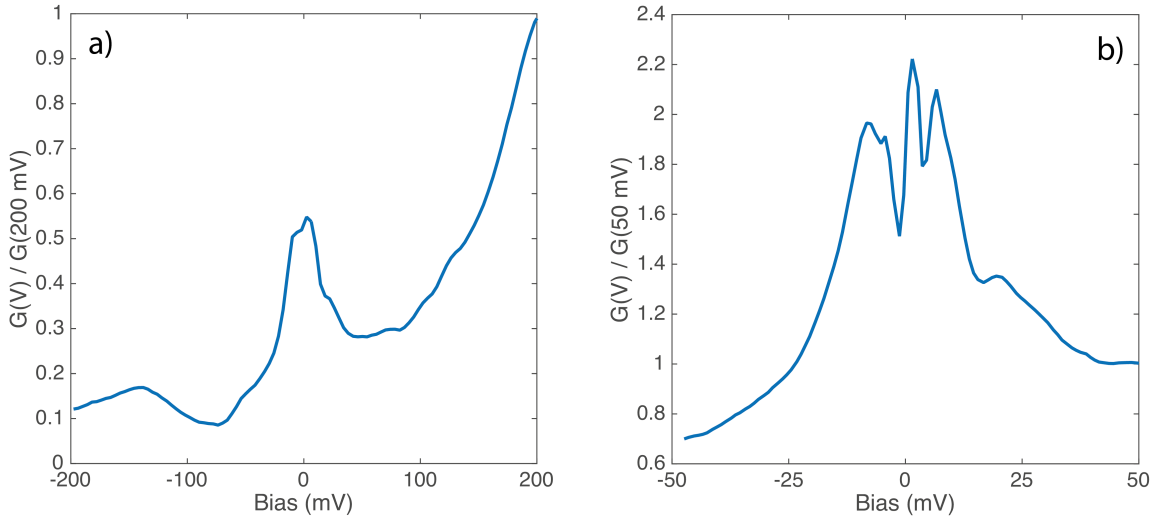

Figure 5.6: Representative spectra of $PdTe_2$ at 30 mK, taken as averages of 64 individual spectra over a $(3\ nm)^2$ area. a) resolved using $V_s = 200$ mV, $I_s = 0.1$ nA and $V_L = 5$ mV; b) using $V_s = 50$ mV, $I_s = 0.1$ nA and $V_L = 2$ mV.

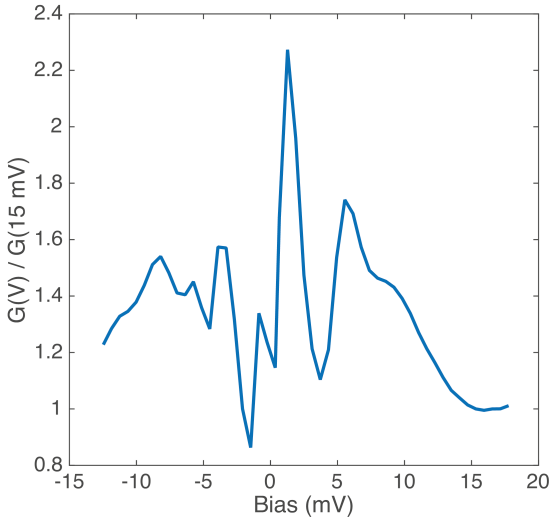

Figure 5.7: Average spectrum of $PdTe_2$ at 30 mK, taken as the average of of 64 individual spectra over a $(3\ nm)^2$ area, using $V_s = 15$ mV, $I_s = 0.1$ nA and $V_L = 0.6$ mV.

These peaks in the spectroscopy, particularly at -130 mV, 0 mV and toward 200 mV can be compared to features seen in the predicted band structure for $PdTe_2$, which at least for the sub-E_F predictions have been matched in ARPES experiments. It can be seen in figure 5.8 that along the Γ-M direction there are band minima at these energies. Regions were bands are turning over and are flat produce a high density of states in a narrow energy width; appearing as peaks in spectroscopy. At the Fermi level and below at -130 mV, two surface state bands turn over; whereas at 200 mV there is the band maximum of a bulk hole-like band. The fact that the surface band minima appear as such intense peaks in spectroscopy demonstrate that in a surface probe such as STM (like ARPES), surface states can easily stand out from background bulk band structure.

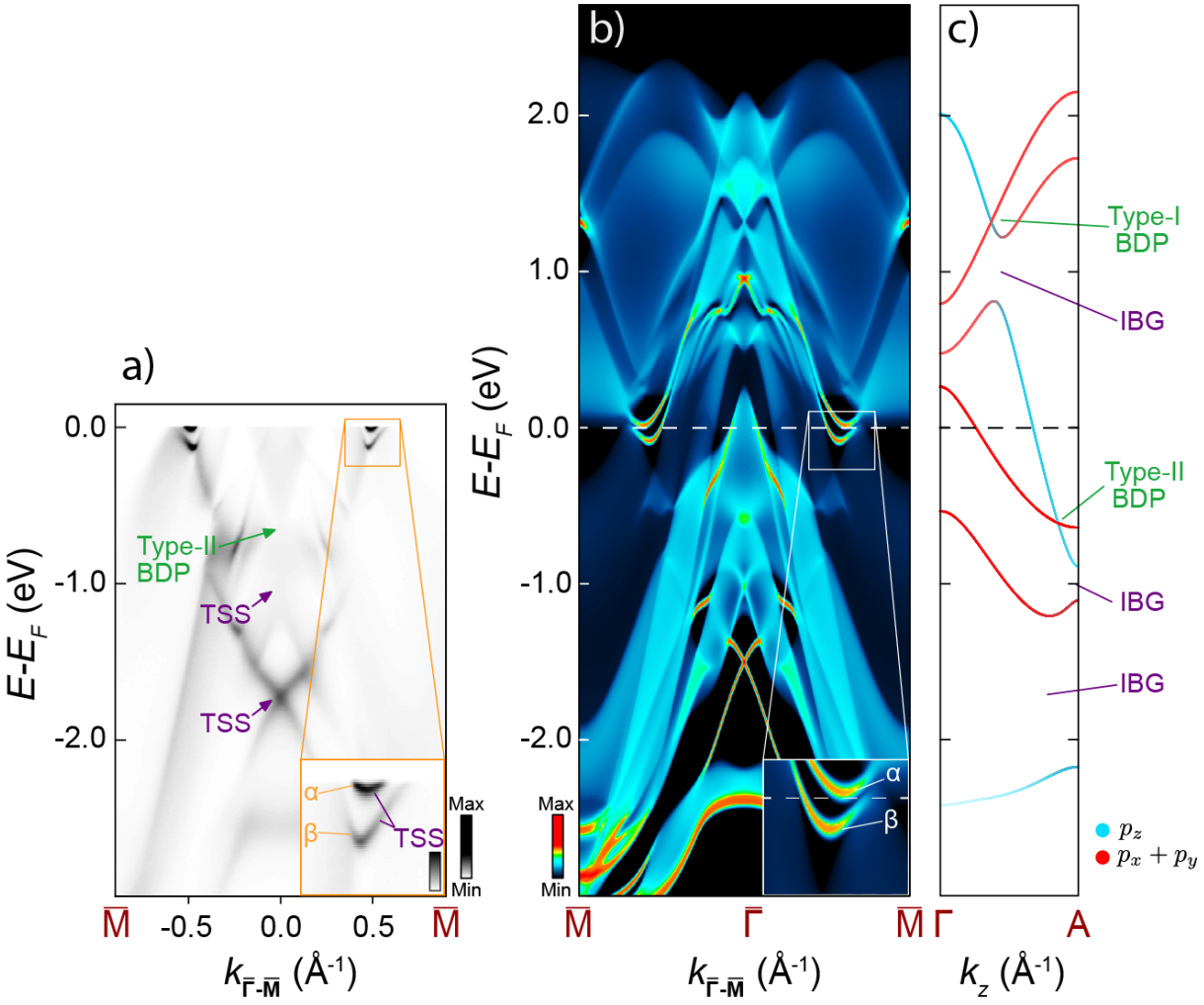

Figure 5.8: a) ARPES measurements along Γ-M using hν = 24 eV, marked with the various topological phenomena, with c) their dispersion along k_z. b) Supercell calculations of the dispersion along the in-plane Γ-M direction from M. S. Bahramy at the RIKEN centre. Figures taken from O. J. Clark et al [133].

5.3.2 Superconducting Gap

Concentrating on the superconductivity in $PdTe_2$ by using a very low lock-in amplitude of $V_L = 25$ μV revealed a near fully gapped (∼90 %) U-shaped superconducting gap at 40 mK of a width $\Delta \sim 215$ μeV. The data was fit with a simple BCS-Dynes type model which also took into account both thermal and lock-in broadening of the STM. Thermal broadening was taken as the proven electronic temperature of this STM which was of the order of 100 mK [58] and lock-in broadening was taken as the amplitude used in the spectroscopy. A Dynes broadening energy of ∼65 μeV fitted the data most accurately,

however the coherence peaks of the superconducting gap appear much broader than the model would allow; which could perhaps be attributed to anisotropy of the gap. The data is then also fitted to a BCS-Dynes model (without thermal and lock-in broadening) but includes superconducting gap anisotropy of the form:

$$\Delta = \Delta_0 + \Delta_1 cos(2\theta), \tag{5.1}$$

$$G_{an} = \frac{1}{2\pi}\int_0^{2\pi} G[\Delta(\theta)]d\theta \tag{5.2}$$

to attempt to recreate the known fact that the superconductivity in $PdTe_2$ is more robust in magnetoresistance when measured perpendicular to the c-axis than parallel to it [128]. This would manifest itself as a superconducting gap that is greater in one direction than in the other.

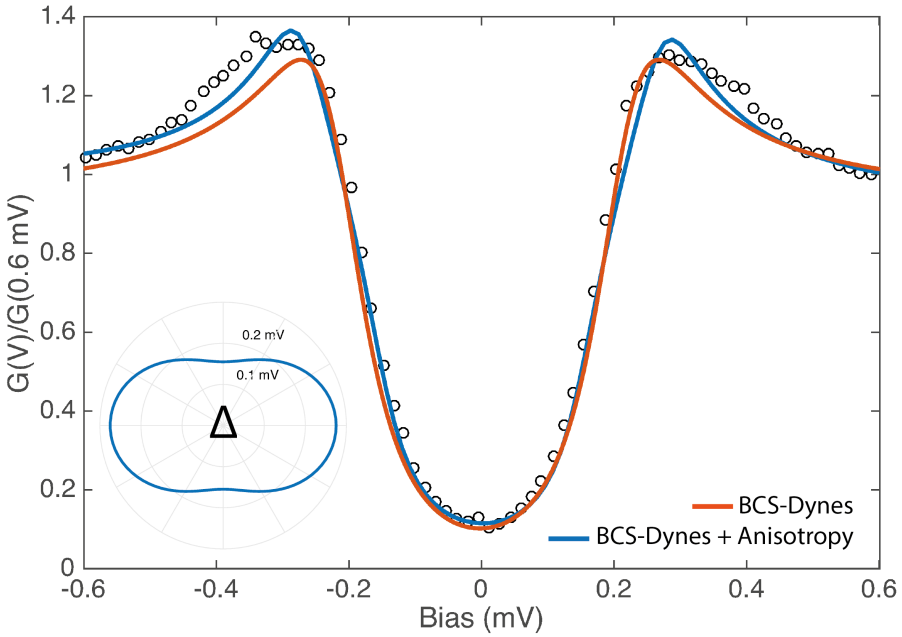

Figure 5.9: Superconducting gap of $PdTe_2$ taken at 40 mK, taken as an average of 256 spectra taken as an average over a $(5.4\ nm)^2$ area, using $V_L = 25\ \mu V$, $I_s = 0.4$ nA and $V_s = 8$ mV. Data fitted with a BCS-Dynes model incorporating both thermal broadening of 100 mK [33] and lock-in broadening of 25 μV (orange). A gap size of $\Delta = 215\ \mu eV$ and Dynes broadening of $\Gamma = 65\ \mu eV$ was used. The other fit is that of a simple BCS-Dynes gap with added gap anisotropy of the form $\Delta = \Delta_0 + \Delta_1 cos(2\theta)$, with $\Delta_0 = 215\ \mu eV$, $\Delta_1 = 60\ \mu eV$, $\Gamma = 45\ \mu eV$. Both models have an additional linear background and offset conductance.

The anisotropic gap fit fits somewhat better than the isotropic gap model, successfully broadening the coherence peaks of the main gap. This anisotropy gap of 60 μeV is ~30% of the primary gap and the gap at its maximum $\Delta_{max} = 275$ μeV has an energy scale that is 1.88 $k_B T_c$; compared to the isotropic gap ratio of 1.47 $k_B T_c$. The superconducting gap seen here in $PdTe_2$ looks remarkably similar to the superconducting gap seen in strontium intercalated bismuth selenide ($Sr_xBi_2Se_3$), where the Sr intercalation induces superconductivity in the otherwise topological insulator Bi_2Se_3 [144][145]. $Sr_xBi_2Se_3$ is likewise a candidate topological superconductor from its interplay of topological insulating states and the induced superconductivity; as well as showing similar bright 3-fold symmetric surface defects. The superconductivity was fully gapped with rather broad coherence peaks like $PdTe_2$, modelled well with an anisotropic gap of the same $\cos(4\theta)$ form and showed no zero-bias peaks in magnetic fields [146].

5.3.3 Superconducting Tip (S-S Junction)

Perhaps owing to the weakly bound layered structure of $PdTe_2$, the sample itself proved very flakey during experimentation, to the extent that it was very difficult to not have a superconducting tip caused by a flake of $PdTe_2$ itself. This superconducting tip was still atomically resolving, however it often made direct measuring of the superconducting gap impossible. This had the effect of doubling the width of the superconducting gap and producing intense coherence peaks, something that is easily explained by noting that the tunnelling current, when disregarding any thermal and lock-in broadening, is simply a convolution of the tip and sample density of states:

$$I_{T\to 0} = \frac{4\pi e|M|^2}{\hbar}\int_{-\infty}^{+\infty} \rho_s(\epsilon)\rho_t(\epsilon + eV)d\epsilon; \tag{5.3}$$

where two identical gap structures will result in a double gap in the differential conductance dI/dV. It can be seen in the figure below that the gap has now doubled in width from $\pm\Delta$ to $\pm 2\Delta$ where $\Delta = 215$ μeV. Since the suspected gap anisotropy is only a small effect as can be seen earlier, modelling the superconductor-superconductor Josephson

junction of $PdTe_2$ is done using a simple isotopic gap for both sample and tip.

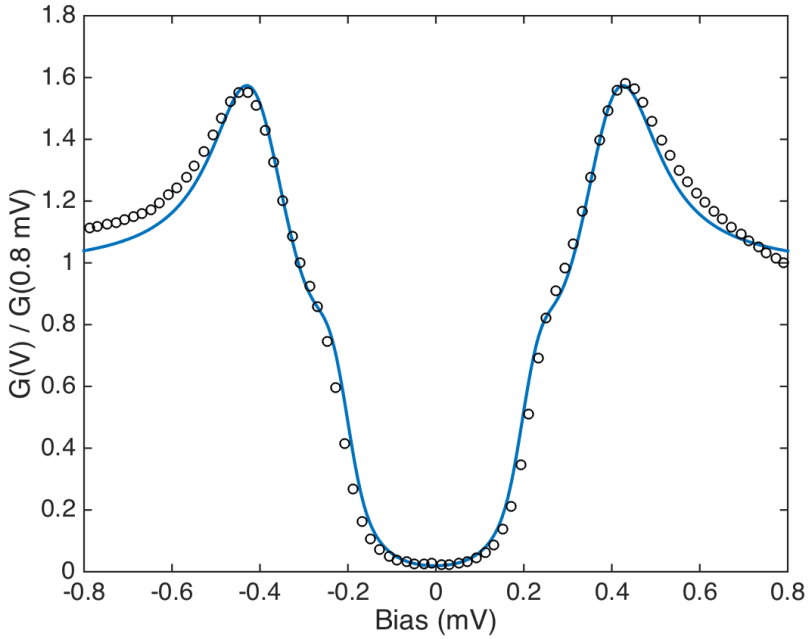

Figure 5.10: Superconducting gap of $PdTe_2$ at 40 mK with a superconducting tip produced by a flake of $PdTe_2$ with zero applied field. The data is fitted with a model which focused on a BCS-Dynes superconducting tip and sample with additional lock-in and thermal broadening. Data was fit with the parameters: $\Delta_s = 215$ μeV, $\Delta_t = 240$ μeV, $\Gamma_s = 90$ μeV, $\Gamma_t = 30$ μeV, $V_L = 30$ μV, $T_e = 100$ mK.

5.3.4 Field Dependence

To characterise further the superconductivity of $PdTe_2$, magnetic fields up to 1 T were applied out of plane to the sample surface (along the c-axis). Fitting the above field-dependent spectra with a convolution model incorporating thermal, lock-in and Dynes broadening, under the assumption that at small fields, taken as ±50 mT, the superconducting gap of the tip remains constant (fixed at 240 μeV), produces figure 5.11, which can be fitted with the BCS curve with good agreement:

$$\Delta(H) = \Delta_0 \left[1 - \left(\frac{H}{H_c} \right)^2 \right] \tag{5.4}$$

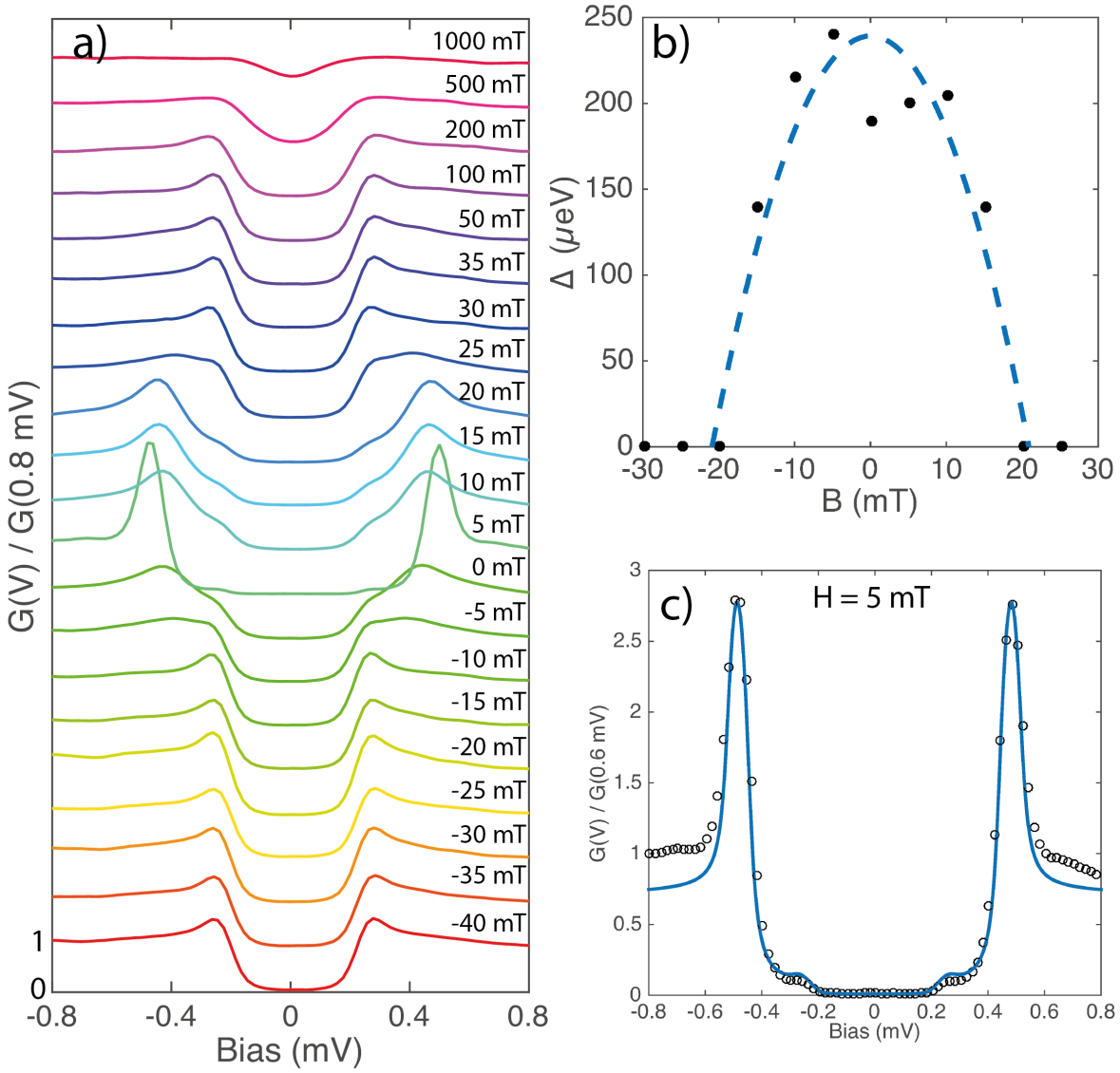

Figure 5.11: a) Field dependence of the superconducting gap of $PdTe_2$ with a superconducting tip at 40 mK. $I_s = 0.4$ nA, $V_s = 8$ mV and $V_L = 30$ μV. Each curve is taken as the average of 144 spectra over a 100 nm^2 area. Each spectrum is offset vertically by 1 for clarity. b) Superconducting gap values as a function of magnetic field, derived from fitting the field dependence curves with the earlier convolution model. The fit produced the parameters: $H_c = 21$ mT and $\Delta_0 = 239$ μeV. c) Superconducting gap structure (SS) in a 5 mT applied field, fitted with: $\Delta_s = 240$ μeV, $\Delta_t = 240$ μeV, $\Gamma_s = 18$ μeV, $\Gamma_t = 4$ μeV, $V_L = 30$ μV, $T_e = 100$ mK.

The superconducting magnet used in the experiment was found to have an offset of ∼-10 mT according to the fitting of Δ(H); the fit of the superconducting gap as a function of field produced a critical field $B_{c_2} \simeq 20$ mT and a zero-field gap of $\Delta(0) \simeq 240$ μeV.

5.3.5 Superconducting Vortices

Applying a small magnetic field to a type-II superconductor such as $PdTe_2$ allows the probing of Abrikosov vortices of quantised magnetic flux. Since each Abrikosov vortex has a single quantum of magnetic flux, applying a magnetic field (below the upper critical field) will produce a lattice of N vortices with the area density, σ:

$$\int_S B \; dS = \Phi = N\Phi_0, \tag{5.5}$$

$$\sigma = \frac{N}{S} = \frac{B}{\Phi_0}, \tag{5.6}$$

where Φ_0 is the flux quantum, equal to h/2e; S the surface area of the sample perpendicular to the applied magnetic field, B. Since the critical field of $PdTe_2$ was found to be so low ($\sim$20 mT), a much smaller magnetic field of 10 mT was applied to the sample along the c-axis as a compromise between vortex density and fullness of the superconducting gap. At 10 mT, a density of 4.8 μm^{-2}; i.e. it would take an STM scan window of (455 nm)^2 to fully image a single vortex (or at least two vortices would separated by 455 nm if assumed to be a simple square lattice of vortices). In a type-II superconductor in the presence of a magnetic field, the magnetic field penetrates only through pores in the surface which are formed as vortices of supercurrent. Here at the vortices the superconductivity itself is suppressed by the magnetic field, resulting in a superconducting gap that is not fully gapped i.e. that $N(E_F) \neq 0$. In STS this would manifest itself as an increase in zero-bias conductance which would decay exponentially away from the core of the vortex, scaled by the coherence length, or size of the Cooper pairs making up the super-current. In the figure below, the zero-bias conductance as normalised to the conductance at 0.62 mV (effectively in the normal state) is mapped, alongside the topography of the area in question. After correcting for the field offset with the Hall probe, (7 $\pm$ 2) mT was the real field applied at the sample.

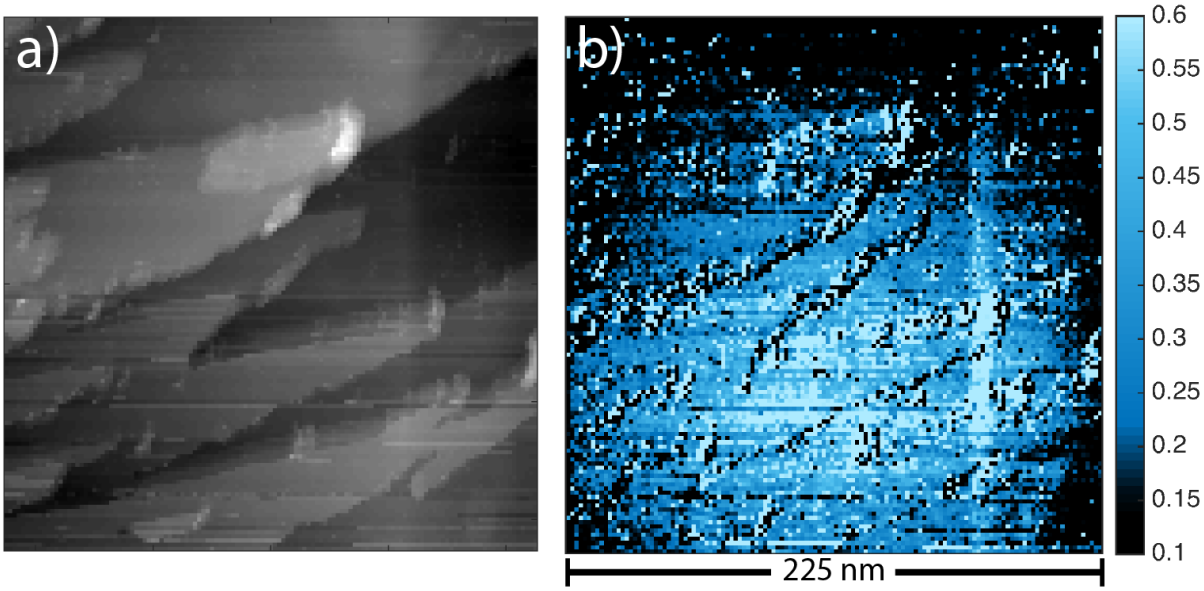

Figure 5.12: a) the real space topographic landscape obtained from the spectroscopic map in an applied field of (7 ± 2) mT, using $V_s = 8$ mV, $I_s = 0.4$ nA and $V_L = 0.1$ mV. b) spatial variation in the zero-bias conductance (ZBC) normalised to the average map conductance at 0.62 mV, revealing the superconducting vortex. The tip was superconducting from an accidentally obtained piece of $PdTe_2$.

From the image of the zero-bias conductance, the Abrikosov vortex is clearly visible as a round blob of enhanced conductance which decays away from its centre. By calculating an angular average, that is averaging over pixels that are a constant radius away from the centre of the vortex, a measure of the decay in ZBC is plotted in figure 5.13. In addition, the full spectroscopy is also plotted as an angular average, with the conductance plotted as the brightness in the colour map.

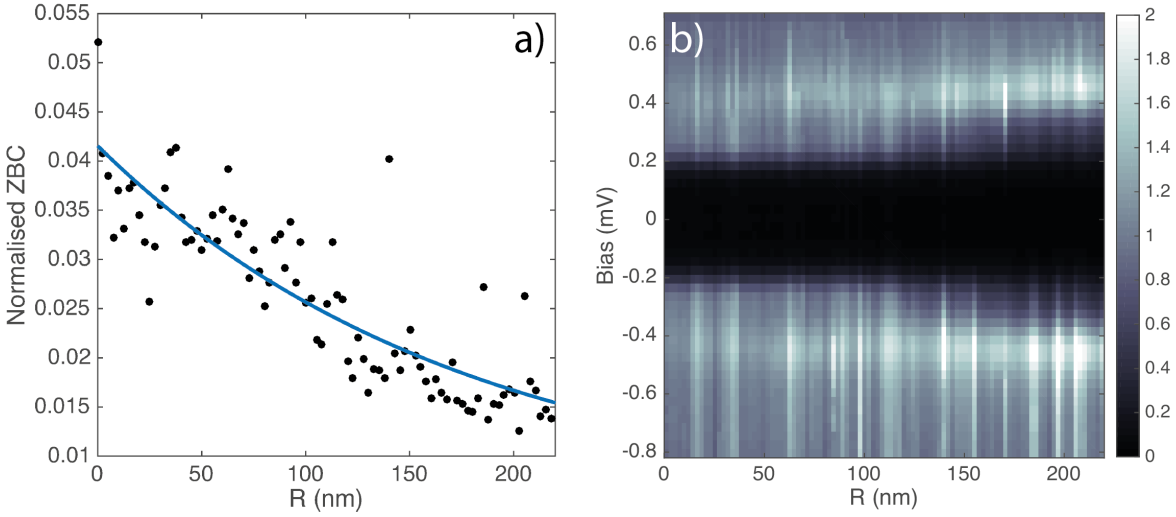

Figure 5.13: a) Zero-bias conductance (ZBC) as a function of radial distance from the centre of a vortex in (7 ± 2) mT applied field, taken as an angular average around points with the same radius. The fitted exponential-decay curve to the tail of the data reveals a decay length L = (175 ± 67) nm. b) shows the how the conductance changes as a function of radius from the centre of the vortex in (7 ± 2) mT applied field. Spectroscopy taken using V_s = 8 mV, I_s = 0.4 nA, V_L = 30 μV and normalised to the conductance at 0.6 mV.

It can be seen in the above figure that the zero-bias conductance decays exponentially away from the core of the vortex, with a few kinks and disturbances in the plot. This can be explained by looking back to the topography of the area probed, where are there are numerous step edges and cracks in the surface which would cause additional scattering and potential bound states that would raise the density of states at those locations. Comparing these cracks to the ZBC image it can be seen that there is significant enhancement of the density of states are these locations, which would then manifest themselves in the angular average of the ZBC. The density of states decays away from the centre of a vortex by essentially exponential decay, producing a characteristic decay length [147]. For this vortex in $PdTe_2$ the decay length of the ZBC was (175 ± 67) nm. This decay length is comparable to the superconducting coherence length ξ and for a BCS type-II superconductor the relation between the upper critical field, H_{c2}, and the superconducting coherence length, ξ, is given by:

$$\mu_0 H_{c_2} = \frac{\Phi_0}{2\pi\xi(0)^2}\frac{T_c - T}{T_c}, \tag{5.7}$$

where Φ is the superconducting flux quantum and T_c is the superconducting critical temperature [1]. For measurement temperatures of the order ∼40 mK and a critical temperature for $PdTe_2$ of the order ∼1.7 K [125]; this temperature scaling on the right-hand side of the equation is approximately 1 (0.98) and therefore can be simplified to:

$$\mu_0 H_{c_2} = \frac{\Phi_0}{2\pi\xi(0)^2}. \tag{5.8}$$

Therefore, for the extracted decay length value of 175 nm, the critical field should be of the order (11 ± 8) mT if a 1:1 correspondence is assumed between the decay length and coherence length. Vice-versa, the coherence length for the Δ(H) fitted value of H_c (20 mT) is ≈ 130 nm.

5.3.6 Conventional Superconductivity

The superconductivity of $PdTe_2$ appears to be completely conventional and described well by BCS theory. The superconducting gap of 215 μeV, when compared to its known T_c of 1.7 K gives a ratio of $\Delta = 1.47\ k_B T_c$; close to the standard BCS prediction of 1.76 $k_B T_c$. The superconducting gap is also modelled well with an anisotropic gap, with a primary gap and anisotropy gap of 215 μeV and 60 μeV respectively. The ratio of the anisotropy model gap at its maximum $\Delta_{max} = 275$ μeV has a ratio of 1.88 $k_B T_c$, larger, but close to the BCS value. The anisotropy in the superconductivity has been observed in recent magnetoresistance measurements and is consistent with this data. The vortex lattice did not appear to have any bound zero-bias states and appeared circular, with the decay length of the zero-bias conductance away from the core of the vortex of ∼175 nm that is comparable to the coherence length derived from the measured critical field of 20 mT to give ∼130 nm. The superconducting gap itself was particularly U-shaped with some slight Dynes modelled scattering, but definitely not V-shaped as is expected of more

exotic superconductors with noded order parameters. Since the superconducting gap is also modelled well with an anisotropic gap model, the vortices could appear elongated like recent work on $Ta_4Pd_3Te_{16}$, if the $PdTe_2$ was cleaved on its side [148]. This work appears to contradict recent magnetisation and magnetic susceptibility measurements that suggested that $PdTe_2$ was a type-I superconductor [141]. Measuring at least one vortex shows that, at least in some local area, that $PdTe_2$ is a type-II superconductor at the surface at the very least. Whether the type of superconductivity differs at the surface compared to the bulk is unknown, though it was suggested that surface superconductivity was more robust in magnetic fields in the same study [141]. Whilst the critical fields were of the same order for this STM work and their investigation, it is difficult to reconcile the presence of vortices and type-I behaviour, unless the samples themselves contained inclusions of type-I material which would produce a strong signal in their bulk techniques. A full temperature dependence would be interesting to see whether the type-II behaviour seen in STM persists in their proposed phase diagram region where surface superconductivity is destroyed and only the bulk remains due to suspected differences in critical temperatures (surface $T_c \simeq 1.33$ K and surface $B_{c2} \simeq 35$ mT [141]).

5.4 Quasiparticle Interference

$PdTe_2$ has a strong quasiparticle response in STS, with strong incommensurate modulations visible in patches around the atomic surface, visible in a narrow energy range around the Fermi level.

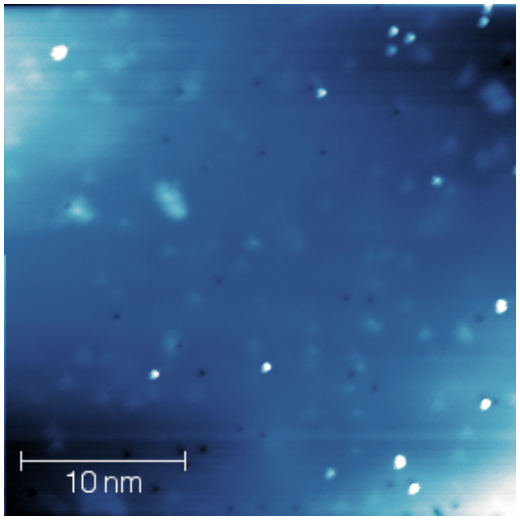

(a) Topography extracted from map.

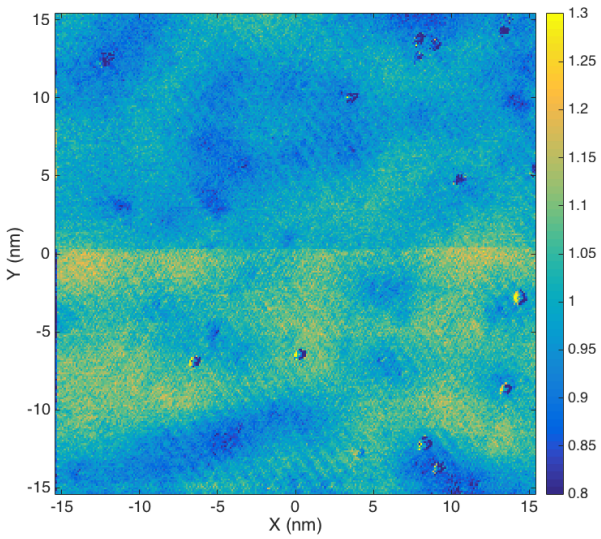

(b) Conductance at -10 mV.

Figure 5.14: Spectroscopic map of $PdTe_2$ taken at 8 K using $V_s = 30$ mV, $I_s = 0.05$ nA and $V_L = 5$ mV in zero-field. a) Is the extracted topography output of the map and b) is the conductance at -10 mV normalised to the layer average.

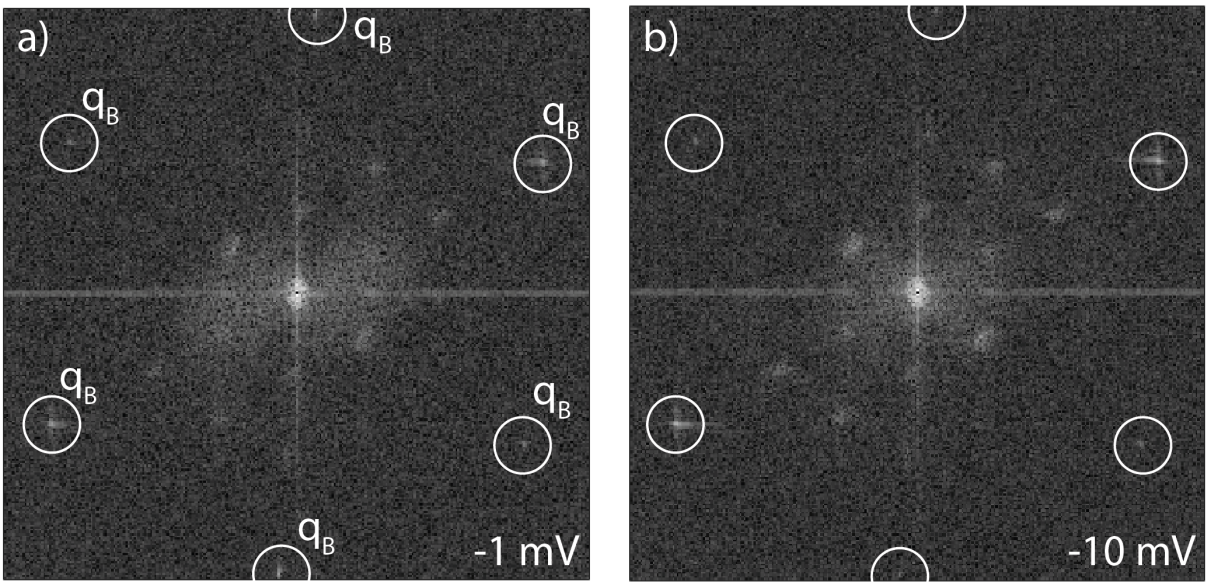

Figure 5.15: Fourier transforms of the conductance maps at a) -1 mV and b) -10 mV spectroscopic bias. q_B is defined as the scattering vector connecting the origin to the atomic lattice Bragg spot.

It can be seen in the above figures that there are quasiparticle signatures visible in the conductance and their Fourier transforms. The most intense modulations are seen as the inner six hexagonal points along the atomic Γ-M direction in the FFT with other

modulations visible further out in both Γ-M and Γ-K directions. The signal appears to be most intense along one particular direction as seen in the FFTs, however this is likely due to tip imperfections producing a preference for conductance along one direction.

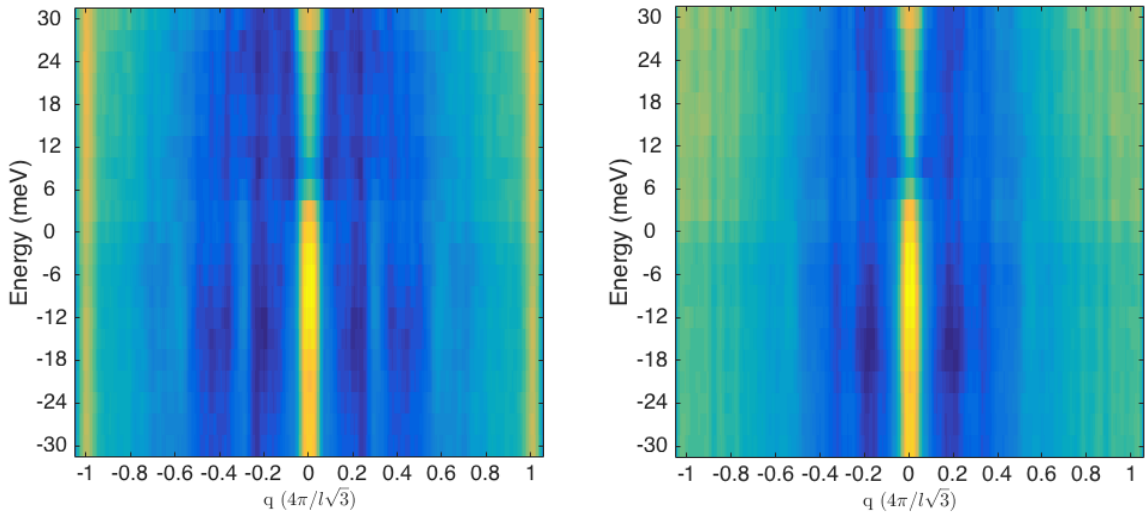

(a) Γ-M. (b) Γ-K

Figure 5.16: Dispersion along the high-symmetry directions of the triangular lattice, using the symmetrised Fourier transform data of the conductance at each bias voltage layer. For contrast an identical Lorentzian is subtracted from every layer to emphasise the modulation peaks.

Symmetrising the Fourier transform along their symmetry directions for each bias layer allows the extraction of the dispersion of QPI features with better signal to noise ratio. It can be seen that the peaks seen in the FFTs appear as bright stripes in the dispersion; with particular intensity along Γ-M at ∼0.3 q_B and ∼0.6 q_B and along Γ-K at ∼0.4 q_B and ∼0.5 q_B, where q_B is the scattering vector between the origin and the atomic Bragg spot. These QPI features do not appear to disperse at all, maintaining the same q-vector at the bias voltages where they were visible. However, these QPI signatures were only visible in the small range ∼ ±30 mV around the Fermi level before disappearing.

5.4.1 ARPES

The QPI data is best compared to Angular Resolved Photoemission Spectroscopy (ARPES), where the Fermi surface is mapped across the Brillouin Zone. The ARPES derived Fermi surface was measured by O. J. Clark et al in the King group at the University of St

Andrews; using a photon energy of hν = 107 eV, measuring E_F ±10 mV, probed close to a high-symmetry A-plane along k_z [133].

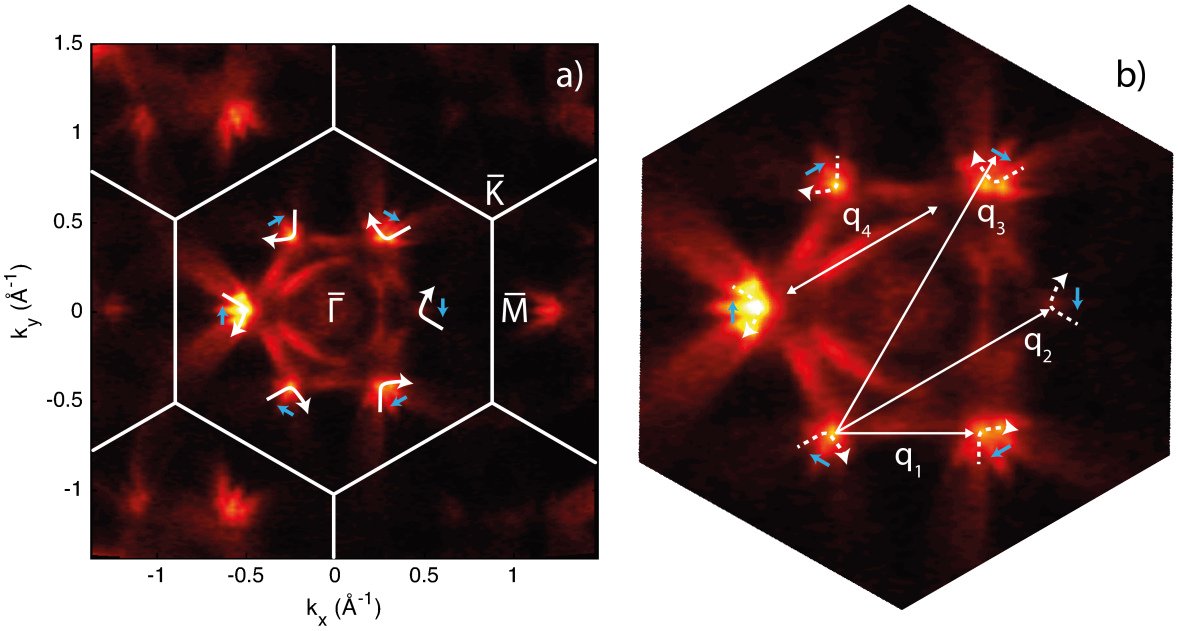

Figure 5.17: Fermi surface of $PdTe_2$ as measured in ARPES, labelled with a) the high-symmetry directions and the measured in-plane chiral spin texture. b) Likely major quasiparticle scattering vectors that conserve spin [133].

The Fermi surface of $PdTe_2$ exhibits 3-fold symmetry with six intense surface state lobes at hexagonal points along the Γ-M direction superimposed on a bulk hexagonal structure; with the addition of a 3-fold triangular symmetric surface state in the centre, aligned with its vertexes along Γ-M. In the very middle sits a bulk state and a small surface state ring. Looking at figure 5.8, the surface state which forms the lobes along Γ-M disperses very steeply in this small region around the Fermi level. Therefore scattering from these steeply dispersing surface bands go far to explain the non-dispersing modulation signature seen in the QPI dispersion plots; when the major scattering signatures occur from scattering vectors between the six lobes. The Fermi surface of $PdTe_2$ has an in-plane chiral spin texture, formed from two branches of a topological surface state, labelled α and β, with opposite chirality. The spin polarised states sit on the corners of a hexagonal Fermi surface, with the inner branch having an anticlockwise chirality and the outer branch going clockwise. The more defined point-like structure at the corner of the hexagon is

attributed to the α band of the topological surface state, with a local band minimum closer to the Fermi energy, forming an electron-like pocket that disperses away from the high-symmetry point as two wing-like structures (α') (see figure 5.8). The other band labelled β has a local band minimum at lower energy and crosses the Fermi level further out towards the high-symmetry direction, appearing as a dispersing oval like structure towards Γ-M [133]. The spin texture around the β band would suppress scattering between like-pockets, but the curved, almost hyperbolic in-plane spin texture of the α and α' bands provide points of common-spin to scatter to on adjacent sites and those around the hexagonal structure. Therefore the scattering vectors q_{1-3} would correspond to inter-band scattering between α pockets (q_1) and/or inter-band scattering between α and β pockets; with their scattering intensities governed by the number of parallel spin states which would likely manifest as an intense q_1 signal and lesser intensity for q_2 and q_3 respectively. The spin-texture of the inner triangular structure of the Fermi surface has not been studied so far, but since the other surface states have shown a chiral spin-structure, it can not be ruled out as a possibility. Intra-band scattering on this triangular structure without any spin texture would manifest itself in QPI as a hexagonally modulated ring-like structure; however if there were a spin-texture along the sides of the triangular structure, quasiparticle scattering could appear as more point like structures of intensity.

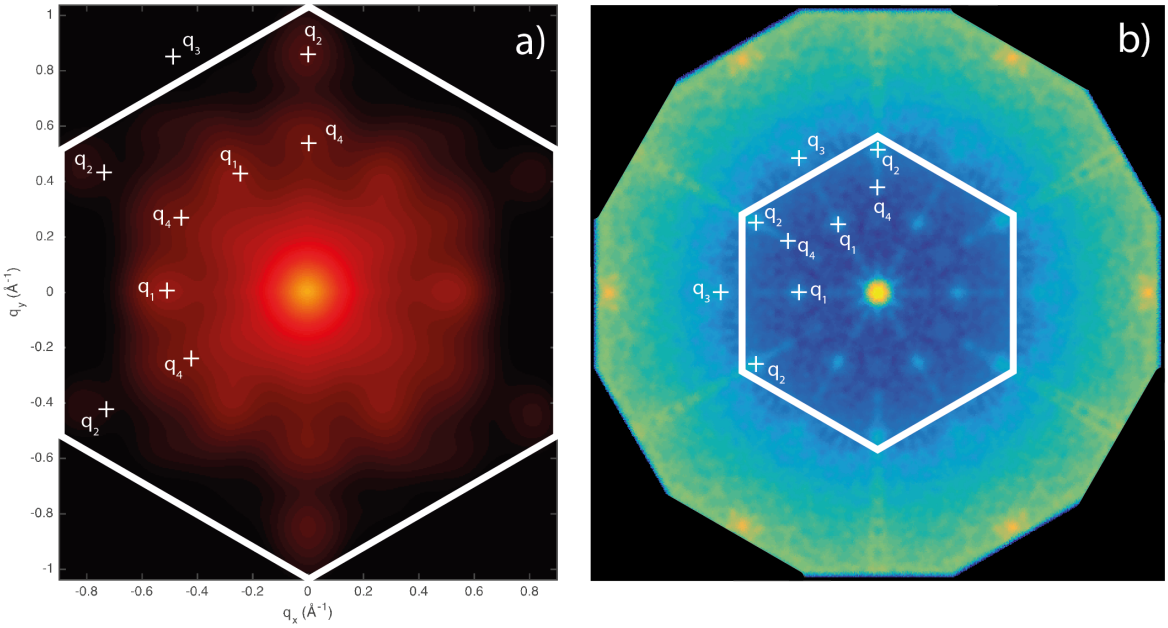

Figure 5.18: a) Autocorrelation of the Fermi surface of $PdTe_2$ and b) symmetrised zero-bias QPI data of $PdTe_2$ taken at 8 K.

Taking the autocorrelation of the Fermi surface, to mimic QPI makes it easier to ascertain whether the predicted scattering vectors match these data (see section 2.3). q_1, q_2, q_4 lie within the Brillouin Zone whereas q_3 lies just outside of it. The lobes of intensity in the Fermi surface autocorrelation broadly match the symmetrised QPI data with the appropriate scattering vectors labelled. By measuring the lengths of the scattering vectors in QPI, the above q-vectors labelled on the ARPES Fermi surface in figure 5.17 correspond in length and direction to those seen in QPI.

Vector	Direction	ARPES (Å^{-1})	QPI (Å^{-1})
q_1	Γ - M	0.55	0.55
q_2	Γ - K	1.00	0.97
q_3	Γ - M	1.02	1.09
q_4	Γ - K	0.67	0.70

Table 5.1: Extracted lengths of q-vectors from both ARPES and measured QPI data. QPI data is scaled such that the distance between the centre and a reciprocal lattice point is $4\pi/l\sqrt{3}$ and the unit cell length a is set by established crystallographic data as 4.0365 Å [124].

The scattering vector q_1, which appears as the most intense spot in QPI corresponds to a real-space wavelength, $\lambda = 2\pi/q_1$, of 11.424 Å or 2.83 basal atomic lattice spacings and

0.306 q_B reciprocal lattice vectors. This real-space modulation along the Γ-M (along the atomic directions) can be seen vividly in both topography (figure 5.3) and conductance as in figure (5.14) with the same incommensurability and wavelength. It can be noted this quasiparticle modulation, at least in topography, is nucleated around vacancy defects in the atomic surface. Whereas the modulation can be seen everywhere, it is most intense in areas of higher vacancy density and weaker on intact regions of the surface. q_2 and q_3 as inter-band scattering vectors on the spin-texture α and $\alpha - \beta$ bands appear with lesser intensity, with q_1 being the most intense and q_3 the least. This intensity heirarchy of the scattering vector intensity backs up the spin textured Fermi surface and its topological surface states, something only recently observed in spin-polarised ARPES measurements. There is a slight discrepancy between the measured ARPES scattering lengths and the signatures seen in QPI, which can easily be explained by the spin-texture. The ARPES derived scattering lengths are based on the non-spin polarised data where the lengths between lobes are measured; without direct use of the spin-texture. Where the ARPES derived lengths are shorter than the QPI lengths, the effect of the spin texture was underestimated in determining the exact location on the spin textures the scattering goes between. However, all four q vectors are in very close agreement overall, with the largest discrepancy being only a ∼6% undershoot of the ARPES derived length compared to QPI for q_3.

The QPI signatures q_{1-4} are only visible in between ±30 mV around the Fermi level where outside of this range the modulation peak washes into the background and modulations are not visible in the topography, let alone conductance images.This could be explained by the dispersing surface bands and their pockets drifting apart and eventually removing the non-forbidden scattering sites; or even just reduced intensity and density of states due to the band curvature and also from the fact that these α and β pockets vanish quickly away from the Fermi level as seen in ARPES. The other surface state scattering vector q_4 can not be readily explained with current ARPES measurements without additional selection rules that would be added by additional spin texture. The fact that point like

signals appear along Γ-K with the correct length suggest that there are discrete scattering points along the sides of the triangular inner surface state. Further spin-polarised ARPES measurements could test this hypothesis or even spin-polarised STM/STS to resolve spin-polarised QPI.

5.4.2 Relative Scattering Intensities

It can be seen in the QPI data and in the ARPES autocorrelations, that the scattering vectors are of different intensities where q_1 is more intense than q_2, which is more intense than q_3. It is possible to explain this intensity scaling with a simple model which takes into account the spin texture of the surface states, simply from geometry. Even though in first order scattering, spin must be conserved, this model is able to take into account the fact that scattering of parallel spins is the most intense and that there will be zero scattering for antiparallel spins. However for spins not aligned in anti-parallel, there will be a finite magnitude of scattering essentially based on a dot product; something that does not accurately reflect nature since it would not conserve spin, which spin-selection rules would therefore suppress. The model starts off by assuming that on each corner of the hexagonal Fermi surface sit N_α spins pointing anti-clockwise and N_β pointing clockwise, but averaged to a single direction respectively.

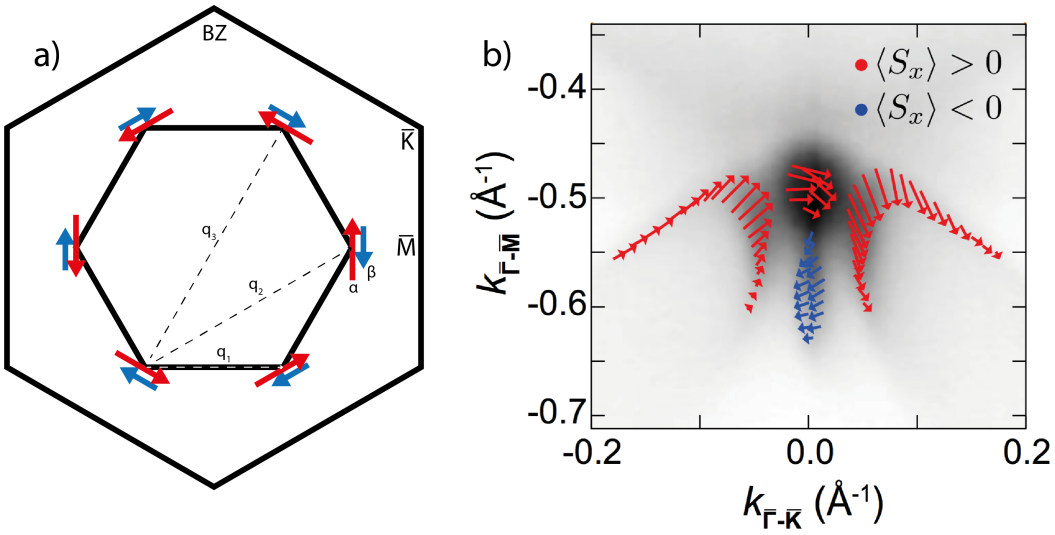

Figure 5.19: a) Schematic of the simplified spin texture of $PdTe_2$. b) Spin-polarised ARPES measurements on $PdTe_2$ taken from [133].

Each spin site can be represented by a spinor:

$$|\psi_{s_1}\rangle = \begin{pmatrix} 1 \\ e^{i\theta_1} \end{pmatrix}, \tag{5.9}$$

and the intensity of quasiparticle scattering is taken as the modulus squared of their overlaps:

$$I_{1,2} = |\langle\psi_{s_1}|\psi_{s_2}\rangle|^2 = 2(1 + \cos(\theta_2 - \theta_1)). \tag{5.10}$$

Which is essentially just a slightly modified dot product of the spin vectors and the intensity of scattering between two sites is therefore proportional to the cosine of the angle between them as:

$$I_{\sigma,\mu} \propto (1 + \cos\theta_{\sigma,\mu}), \tag{5.11}$$

which governs the intensity I of quasiparticle scattering between spin sites σ and μ with an angle θ between them. The model then considers scattering from spins between α sites, β sites and α-β sites on the Fermi surface.

$$I_i \propto I^0_{\alpha,\alpha}(1 + \cos\theta^{(i)}_{\alpha,\alpha}) + I^0_{\alpha,\beta}(1 + \cos\theta^{(i)}_{\alpha,\beta}) + I^0_{\beta,\beta}(1 + \cos\theta^{(i)}_{\beta,\beta}) \tag{5.12}$$

$\mathrm{I}^0_{\alpha,\alpha}$ are pre-factors which are then set to loosely reflect scattering amplitudes where they are proportional to the product of the number of spin species in the scatter:

$$I^0_{\lambda,\gamma} = kN_\lambda N_\gamma, \tag{5.13}$$

where k is a scaling factor that assumes that apart from the number product, there is no other dependence for the scattering amplitudes. Inserting this factor gives:

$$I_i = kN^2_\alpha(1 + \cos\theta^{(i)}_{\alpha,\alpha}) + kN_\alpha N_\beta(1 + \cos\theta^{(i)}_{\alpha,\beta}) + kN^2_\beta(1 + \cos\theta^{(i)}_{\beta,\beta}) \tag{5.14}$$

Then by relating the number of α spins to β spins as the ratio:

$$a = \frac{N_\beta}{N_\alpha}, \tag{5.15}$$

the intensity expression becomes:

$$I_i = kN_\alpha^2(1 + \cos\theta_{\alpha,\alpha}^{(i)}) + kaN_\alpha^2(1 + \cos\theta_{\alpha,\beta}^{(i)}) + ka^2N_\alpha^2(1 + \cos\theta_{\beta,\beta}^{(i)}). \tag{5.16}$$

Now considering the 3 main scattering vectors q_1, q_2 and q_3 and their geometry, the three q vectors can be described by three equations:

$$I_1 = kN_\alpha^2(1 + \cos 60^\circ) + kaN_\alpha^2(1 + \cos 120^\circ) + ka^2N_\alpha^2(1 + \cos 60^\circ). \tag{5.17}$$

$$I_2 = kN_\alpha^2(1 + \cos 120^\circ) + kaN_\alpha^2(1 + \cos 60^\circ) + ka^2N_\alpha^2(1 + \cos 120^\circ). \tag{5.18}$$

$$I_3 = kN_\alpha^2(1 + \cos 180^\circ) + kaN_\alpha^2(1 + \cos 0^\circ) + ka^2N_\alpha^2(1 + \cos 180^\circ). \tag{5.19}$$

.

Evaluating this and factorising produces:

$$I_1 = \frac{kN_\alpha^2}{2}(3a^2 + a + 3) \tag{5.20}$$

$$I_2 = \frac{kN_\alpha^2}{2}(a^2 + 3a + 1) \tag{5.21}$$

$$I_3 = \frac{kN_\alpha^2}{2}(4a) \tag{5.22}$$

Finally, simplifying further with:

$$I_0 = \frac{kN_\alpha^2}{2} \tag{5.23}$$

From inspection and from plotting the three scattering intensities as a function as the spin-site ratio, a, it can be seen that for all values of a, $I_1 > I_2 > I_3$. For the fully spin degenerate Fermi surface structure, the effective angle between the spins in the scattering vectors would all be 0° and identical in intensity as:

$$I_{deg.} = I_0(4a^2 + 4a + 4) \tag{5.24}$$

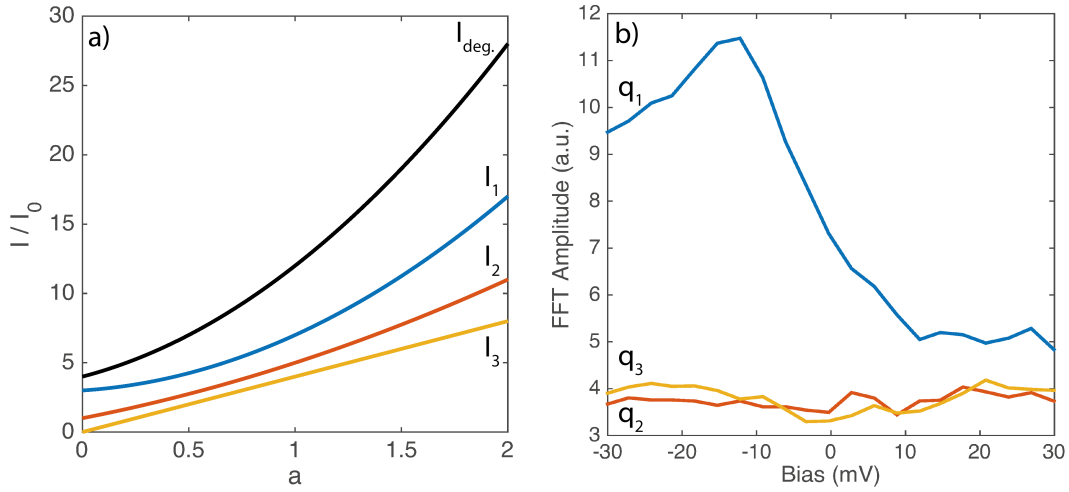

Figure 5.20: a) Predicted scattering vector intensities from the geometric spin texture model as a function of spin-site ratio and b) Fourier intensity of the modulation peaks of the QPI scattering vectors as a function of bias.

It can be concluded from this model that the geometry and therefore the spin texture is the most important factor for determining the relative intensities of the quasiparticle scattering vectors, with the ratio of spin populations having no effect on the ordering of which vector is the most intense, but would naturally affect the absolute intensity of the vectors. Therefore from the spin-polarised ARPES measurements, which first determined the chiral spin texture, the quasiparticle scattering vectors in QPI follow this geometrical model which requires a chiral spin texture; consistent with the spin-texture of these surface states. As expected, the case for a fully spin degenerate Fermi surface would have

identically intense q-vectors and these would have much greater intensity overall than their spin-polarised equivalents.

5.4.3 Long Wavelength QPI

Measuring over much larger areas revealed long wavelength modulations in conductance across the sample surface, with a characteristic wavelength of the order of ∼10 nm. One benefit of probing QPI over larger areas is substantial increase in q-space resolution, as demonstrated in figure 5.21; which provides even clearer visualisation of the scattering vectors seen earlier. The much longer modulation of the order 5-10 nm would correspond to a scattering vector of length approximately 0.063 - 0.126 $Å^{-1}$, or normalised as 0.035 - 0.070 q_B, where q_B is defined as $4\pi/l\sqrt{3} = 1.7974$ $Å^{-1}$. This approximate range of scattering lengths for the long-wavelength modulation is indicated on the QPI plot in figure 5.21 as the two dashed circles labelled q_L. There does appear to be ring like structures in the QPI in this q range, however to fully resolve any potential sub-structure of this QPI feature, further maps would need to be taken over an even greater area to achieve sufficient q resolution.

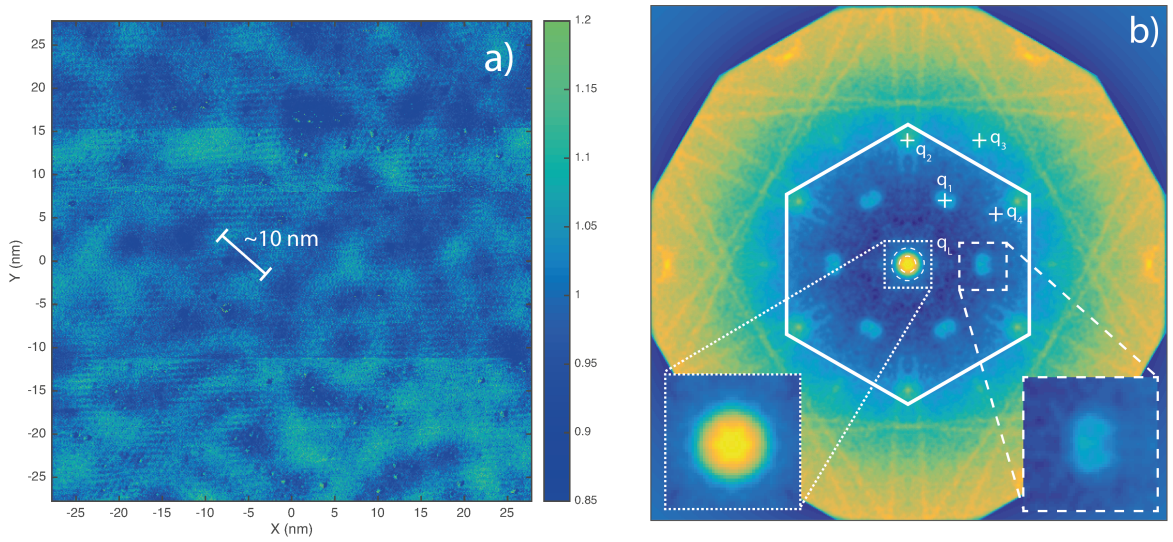

Figure 5.21: a) Normalised zero-bias conductance map of $PdTe_2$ at 8 K and b) its symmetrised QPI FFT labelled with q vectors and with zoomed insets of q-space structure.

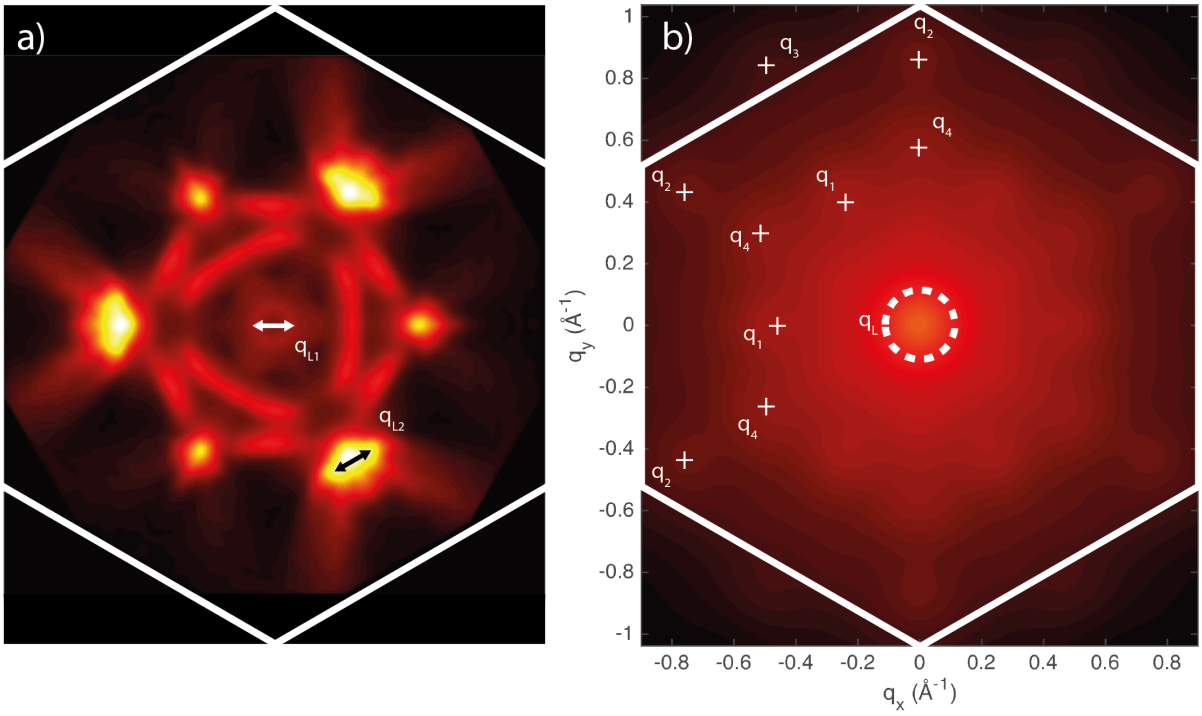

Figure 5.22: a) Symmetrised ARPES Fermi surface, retaining both the 3-fold and 6-fold symmetry components. b) Autocorrelation of the symmetrised Fermi surface.

Looking at the symmetrised ARPES Fermi surface, to sharpen the spectral features, it

can easily be seen that the innermost ring structure attributed to another surface state has a diameter of approximately $q_{L1} \simeq 0.1$ Å^{-1}, therefore offering a q vector of the same length that it is consistent with the predicted q range for the long wavelength modulations of the order 5-10 nm. This surface state is not known or expected to have a spin texture (spin degenerate) therefore would create a ring like signature in QPI. Of course at this resolution, it is possible that the ring structures in the QPI could be due to a Lorentzian-like peak formed by incoherent scattering from defects. There is another possibility of scattering between α' wings at the corners of the hexagonal Fermi surface, represented by q_{L2} which is of length $\sim$0.1 Å^{-1} and would point in the Γ-K direction. This scattering is allowed by the spin texture and would produce a hexagonal structure in QPI around the centre, with corners pointing towards Γ-K. There is insufficient q-resolution in QPI results to image the finer structure of the long-wavelength region, so it is not possible to tell whether the long wavelength modulations come from the inter α' scattering or the circular inner surface state or both. It is interesting that quasiparticle scattering off these small surface states can produce surface modulations of conductance of the order of 10%, with the other topological surface state scatterings superimposed over the top and nucleated at lattice vacancy defects.

It also visible that when much greater q resolution is achieved from probing a larger area, but sacrificing energy resolution, the QPI signatures associated with q_1 of nearest neighbour surface inter-band scattering opens out into a more crescent moon shape. This crescent shape is likely due to the spin texture of the chiral surface states, where only certain sides of the wings and pockets of the α and β bands have non-forbidden scattering vectors to conserve spin; producing a scattering sub-structure that mimics the surface state pockets. One would imagine that as these bands disperse, especially the α' wings, that the crescent shaped QPI signature would likewise evolve.

5.4.4 Incipient Charge Density Wave Order?

Even though the QPI measurements match remarkably well to available scattering vectors seen in ARPES and the spin texture of the Fermi surface, there is the possibility that the modulations seen here in STM could be a form of incipient charge density wave order (CDW), in particular the strong modulation in q_1. The family of TMDs contain many metallic compounds that transition into CDW order, with established CDW order seen in 1T-TaS_2 [149], 1T-$TaSe_2$ [150] and 2H-$NbSe_2$ [151][152]. With particular relevance is the nearly-commensurate CDW order in 2H-$NbSe_2$, where below T_{CDW} = 33.7 K there is a transition from a metallic phase to a CDW ordered phase, which is nearly-commensurate with an energy and temperature independent wavelength of three atomic spacings with 3Q-order. What was interesting was that above T_{CDW}, signatures of the CDW order were still visible in STM, nucleated at defects [153]. These patches of nucleated shorted-ranged CDW order would grow approaching T_{CDW} before covering the entire surface, suggesting that there is an important role for the defects in this transitional region before full CDW coverage kicks in. STS measurements saw significant spectroscopic changes at the CDW wave vector 0.7 eV below the Fermi level with minimal changes at the Fermi level, however no CDW gap was observed there; which the authors instead attributed to strong electron-lattice interactions to create the CDW order, instead of the more conventional Fermi surface physics approach [153]. This short-ranged CDW order was also observed in STM studies when there was a high intercalation of species such as Mn and Co; observing that long-range order with full global coherence only sets in at T_{CDW} [154].

This incipient CDW order looks remarkably like the modulations seen in this work on $PdTe_2$, where surrounding the vacancy defects in the surface, strong and short-ranged incommensurate modulations existed. This modulation was often clearer and slightly more widespread when seen in conductance rather than topography, but still only existed in patches around defects like $NbSe_2$. If this modulation, designated q_1 earlier on, was instead incipient CDW order, it would not be inconsistent with the rest of the TMD

family. No CDW order has been observed in $PdTe_2$ to date, whether incipient or not, and thus there is no characteristic temperature scale to compare to. But if it were the case in $PdTe_2$, the existence of the patches of short-ranged modulations could suggest a CDW ordering temperature even colder than 40 mK where it was observed here with very little difference between its appearance at 8 K. With such a low potential temperature scale, it could remain incipient at all temperature scales, possibly explaining its absence in ARPES and other techniques to date. Such incipient CDW behaviour has been seen in other superconductors such as the high-temperature superconductor $YBa_2Cu_3O_y$ [155]; perhaps pointing a link between many unconventional superconductors and CDW behaviour. In the absence of CDW signatures from other techniques and from the closely matching TSS-QPI scattering data, the hypothesis of incipient CDW is unlikely to be true.

5.5 Conclusion

$PdTe_2$ was cleaved to produce larger atomically flat areas thanks to the layered crystal structure seen in the transition metal dichalcogenides. The surface contained many defect structures with 3-fold symmetric enhancements in density of states and six-fold symmetric modulations that spread $\sim$5 nm from vacancy defects with an incommensurate wavelength. Spectroscopy reveals a density of states profile with many large peaks that are consistent with band extrema as seen in ARPES below the Fermi level and predicted in DFT calculations above it [133].

The superconductivity was measured at 40 mK which showed a superconducting gap structure that matched a standard BCS shape, with a gap of $\Delta = 215$ μeV and evidence for anisotropy when fitted with an anisotropic gap of the form $\Delta = \Delta_0 + \Delta_1 \cos(2\theta)$ with 30% anisotropy and a gap maximum of 275 μeV. As a downside of $PdTe_2$ being such an easy material to cleave, with weak Van der Waals bonding between layers, $PdTe_2$ debris readily and robustly formed a superconducting tip which proved very difficult to remove. However these superconducting tips showed atomic resolution and spectroscopic stability.

A full field dependence with the superconducting tip suggested a critical magnetic field of ∼20 mT and zero-field gap size of ∼240 μeV. A large superconducting vortex was observed which appeared with a coherence length of the order ∼175 nm that contained no zero-bias bound states, affirming itself as a type-II superconductor. The coherence length produces a BCS critical field of the same order as that measured form the field-dependence; all evidence pointing to $PdTe_2$ being a conventional type-II superconductor, contradicting recent magnetisation and magnetic susceptibility measurements that saw strong type-I behaviour with enhanced surface superconductivity [141].

Quasiparticle interference saw strong modulations consistent with the topological surface states recently measured in ARPES [130][133] and an intensity hierarchy and q-space structure that is consistent with a spin textured Fermi surface. Scattering from these spin-polarised topological surface states produce strong modulations in real space, in particular a q-vector of length 0.55 $Å^{-1}$, which formed trailing modulations in the surface charge density, nucleated at vacancy defects. These modulations look at first glance like incipient CDW order as seen in $NbSe_2$, however evidence for this has not been seen in ARPES and it would be too much of a coincidence for this to match the topological surface states. These scattering vectors were not found to disperse in the energy ranges studied, but they were seen to vanish outside of an approximate window of ±30 mV, consistent with idea that the intense scattering occurs at the band minima of these surface states which disperse off rapidly. As revealed in higher-resolution long-wavelength QPI, the structure of the q-vector of 0.55 $Å^{-1}$ length opens up into a crescent moon shape, something that must be caused by the spin texture of the α and β pockets of the Fermi surface and the relative scattering sites at neighbouring Fermi surface lobes.

The interesting conclusion of this chapter is that even though there are such prominent topological surface states, as detected in ARPES and inferred by QPI, the superconductivity appears to be completely ordinary. Topological materials with superconductivity, whether through proximity or nature, were thought of as a route to p-wave supercon-

ductivity. The fact that a topological material, topological simply due to its orbital and crystal structure as a member of the TMD family [130], possesses ordinary type-II BCS superconductivity calls into question whether p-wave materials are achievable this way. Other superconducting members of the TMD family should be investigated in the same way as this work to see if the topological nature and conventional superconductivity is ubiquitous.

Chapter 6

High Magnetic Field Superconductivity in FeSe

6.1 Introduction

Iron based superconductors are a family of layered materials with transition temperatures that can reach as high as 55 K and Cooper pairing mechanisms that are believed to driven by spin fluctuations, leading to unconventional superconductivity such as anisotropic s-wave and d-wave symmetries. The iron based superconductors have crystal structures that are generally planar layers of iron atoms, connected by tetrahedrally coordinated pnictogen or chalcogen anions. These layers are stacked and separated by blocking layers, typically made up of rare-earth and alkaline-earth metals, as well as other species. The superconductivity is believed to originate in the iron layers, in a similar vein to the copper-oxygen layers in the high-temperature cuprate superconductors [156].

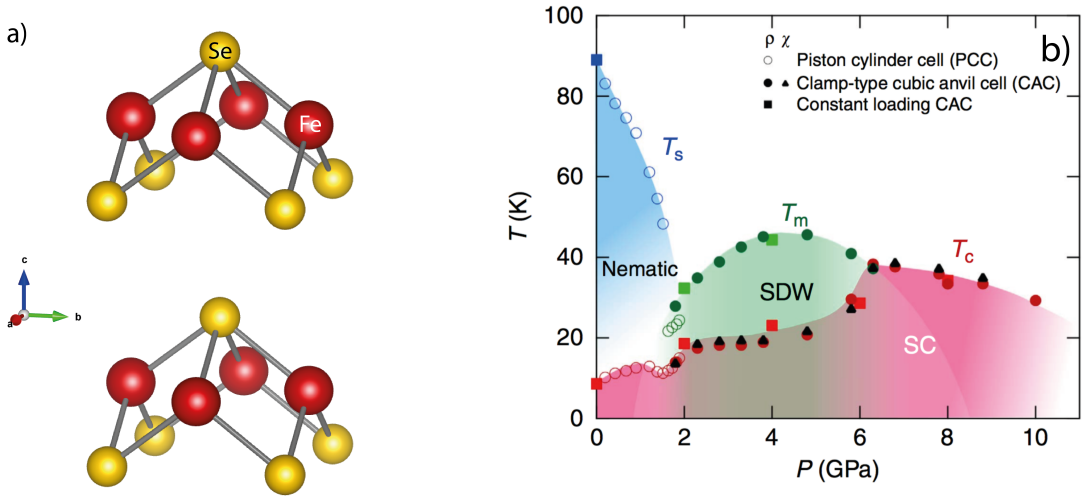

Figure 6.1: a) Crystal structure of tetragonal FeSe which has the lattice parameters a = b = 3.765 Å and c = 5.518 Å [157] and becomes orthorhombic below 87 K to have a = 3.773 Å , b = 3.777 Å c = 5.503 Å as α-FeSe [158]. b) Pressure-Temperature phase diagram of FeSe taken from [159].

FeSe is the simplest of the iron-based superconductors, consisting only of iron-selenium stacked layers and has a transition temperature in the bulk of T_c ~8 K [158] which can be enhanced up to 27 K by applying hydrostatic pressure [160]. Growing thin films of FeSe on $SrTiO_3$ substrates can boost the T_c further up to 80 K [161] and then even further to above 100 K when grown on doped $SrTiO_3$ [162]. FeSe has a structural transition below 87 K, where it changes from a C_4 symmetric tetragonal crystal structure to a C_2 symmetric orthorhombic structure, without the appearance of any long-range magnetic order [163]. At the same time as the structural transition, the electronic structure also undergoes a transformation from C_4 symmetry to C_2 symmetry, which is commonly referred to as a nematic phase. This change in electronic structure is also believed to affect the superconductivity. During this structural and electronic symmetry breaking, the time-reversal symmetry is maintained. The order parameter for a phase transition where rotational symmetry is broken whilst preserving time-reversal symmetry is known as a director; which defines an axis without any particular direction, akin to liquid crystal nematic phases [164][165]. Applying pressure to FeSe creates a phase-diagram of states where FeSe can exist as regions of coexistence and competition of these nematic and superconducting states as well as a spin-density wave (SDW) ordered phase [159].

One of the most famous defects in the iron-based superconductors are the iron-site defects with a dimer-like appearance seen on the surface of FeSe. These dimer-like defects appear as bright dumbbell shapes in STM pointing along either the a or b crystal axes, with two shadow features that run in parallel surrounding them, both separated by approximately 16 iron-site spacings. These dimer-like defects have been attributed to an iron site vacancy beneath the selenium surface termination in both the equivalent iron sites, which allows the defect to point in either axis direction. This hypothesis is backed up by STM studies and density functional theory (DFT) calculations [166]; replacing the old theory that they were caused instead by selenium adsorbates or substitutions [167][168]. The parallel lines that connect these shadows are all themselves in parallel on each domain and become rotated by 90 degrees across a twin boundary where the crystal structure is reflected. The twin-boundaries run at 45 degrees to the Fe-Fe bond directions and suppress the superconductivity. These twin-boundaries have been consistently seen to pin vortices in magnetic fields [169]. The twin-boundaries are also thought to cause a twist in the order-parameter, without any zero-bias signatures in STS, suggesting that time-reversal symmetry gets broken, but is then maintained within each domain [170]. The nematicity was found to couple strongly to stripe spin-fluctuations, which become strongly enhanced at the structural transition at 87 K in neutron scattering experiments. Similarly a sharp spin-resonance is observed in the superconducting state, with a $\sim$4 meV width, which is believed to be consistent with the electron-boson mode seen in STS; supporting the idea that both the superconductivity and nematicity are spin fluctuation driven [171].

There has been recent controversy over the high-magnetic field regime in FeSe, where in a study led by S. Kasahara et al it was suggested that above $\sim$13.5 T, FeSe enters into a new superconducting phase that persists until around 17 T [172]. The residual thermal conductivity in magnetic fields experienced a kink at this 13.5 T, referred to as H^*, and produced a downturn that increased in steepness with lowered temperature. This proposed high-field phase coincides with the point where the three energy scales that describe the system become comparable, that is: $\mu_B H^* \sim \epsilon_F \sim \Delta(0)$, entering into the BCS-BEC (Bose-Einstein Condensate) regime. In this crossover regime, it was suggested

that the strongly spin-inbalanced Fermi liquid might change into something completely different; with ideas being proposed such as Lifshitz-like electronic transition or that a new superconducting phase may occur that has a mixture of odd-frequency pairing and spin-triplet pairing or a spatially modulated FFLO-like state [172]. These measurements were backed up by later magnetic torque, NMR and transport measurements which showed a very large non-linear diamagnetic response below 20 K [173]. This temperature scale coincided with the apparent opening of a pseudogap, adding to the mystery of the superconducting phase diagram of FeSe in the BCS-BEC crossover regime [173]. However later thermal conductivity measurements by P. Bourgeois-Hope et al at 75 mK, a much lower temperature than in Kasahara's work, and in fields up to 17 T, demonstrated there were firstly no zero-energy quasiparticles and therefore no nodes in the superconducting gap of FeSe. But also that at 14 T, the residual heat capacity converges to that of the normal state; suggesting that FeSe is just no longer superconducting above 14 T and that this field-scale is in fact just the upper critical field H_{c2}. The work did however reaffirm the two-band character of the superconductivity with one gap estimated to be an order of magnitude smaller than the other [174]. The aim of this investigation would be to see whether bulk FeSe is still superconducting at 14 T and if there is a significant change in the gap structure or the vortex state.

6.2 Superconductivity in High Magnetic Field

6.2.1 Topography

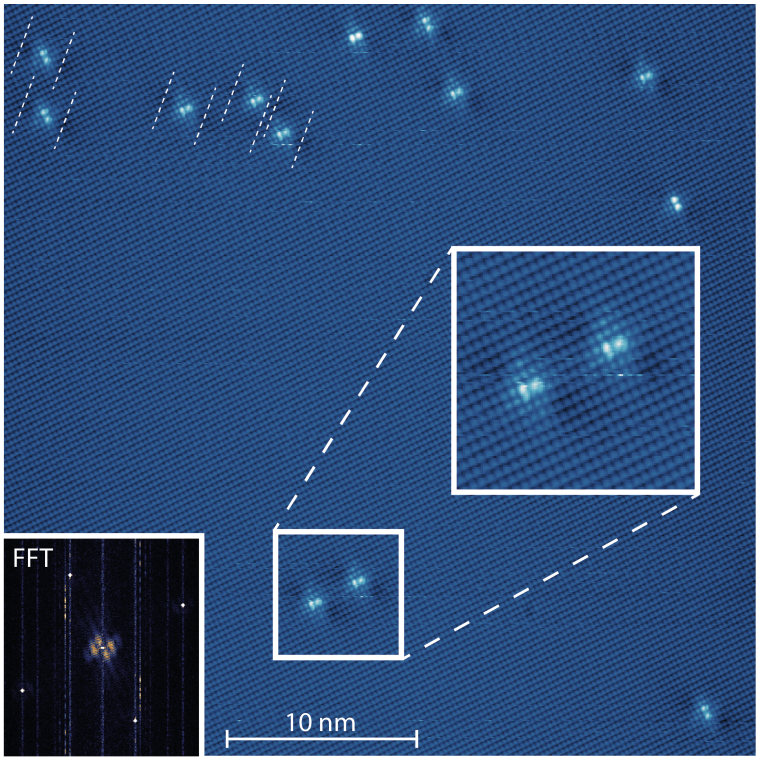

Figure 6.2: Topography of FeSe taken at 60 mK using $V_s = 0.05$ mV and $I_s = 0.1$ nA. Two dimer defects have been magnified to emphasise their structure and quasiparticle signatures. The inset shows the FFT of the surface topography.

The bulk FeSe crystals were supplied by A. Coldea and were characterised to have a residual resistivity ratio (RRR) of 20-30. Topographic imaging on FeSe reveals the selenium terminated surface, its orthorhombic structure where the FFT inset shows the orthorhombic structure of this α-FeSe phase and thus its C_2-rotational symmetry. The defects visible on the surface are that of iron-site dimer-like defects, which lie along both axes and have a visible quasiparticle interference signature in the shadowing surrounding them. The shadows run in parallel when these dimers lie on the same domain, as indicated in the above figure where there is no twin-boundary present to rotate these shadows $\pi/2$. At 60 mK FeSe is well into its nematic-orthorhombic and superconducting state and is therefore ideal to investigate the high-field superconductivity.

6.2.2 Superconducting Gap

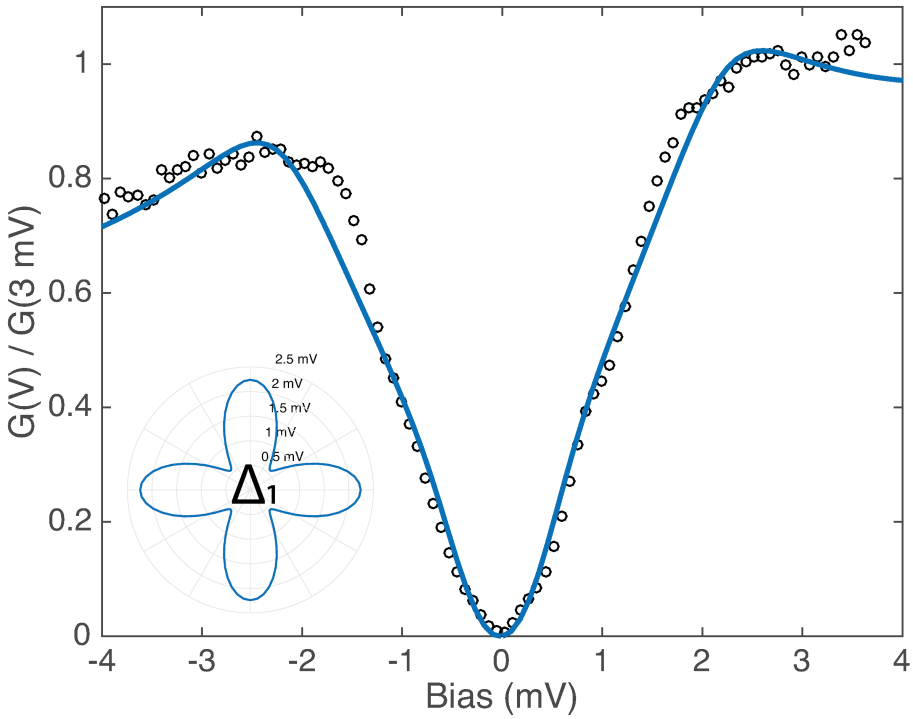

Figure 6.3: Superconducting gap of FeSe at 70 mK, taken as average of 144 spectra over a $(3\ \text{nm})^2$ area using $V_s = 8$ mV, $I_s = 0.4$ nA and $V_L = 50\ \mu$V. Data modelled with a larger anisotropic gap $\Delta_1 = \Delta_1^0 + \Delta_1^a\cos(4\theta)$ with a second s-wave gap Δ_2, both with Dynes broadening; in addition to a linear background.

The superconducting gap spectra in FeSe reveal a complex gap structure with at least two distinct gaps. Following recent STM/STS studies on FeSe, a gap structure that consists of one anisotropic s-wave gap and one conventional s-wave gap is modelled on this zero-field data. A good fit was achieved using $\Delta_1^0 = 1.4$ mV, $\Delta_1^a = 0.84$ mV ($\Delta_1^a/\Delta_1^0 = 0.6$), $\Gamma_1 = 0.65$ mV, $\Delta_2 = 0.55$ mV and $\Gamma_2 = 0.55$ mV. These parameters match closely those in the recent work by Lin Jiao et al [175], however for this data a fit with greater anisotropy was used which could potentially be a product of sample quality if the nematicity linked anisotropy was linked to defects and internal strain. The close fitting helps to confirm the anisotropic superconductivity in FeSe as well as its two band character. The gap minimum appears slightly V-shaped, however it proved difficult preparing a non-superconducting tip on FeSe with sufficient sharpness to capture the coherence peaks of the superconducting gap, so it is unsurprising that the inner gap structure is broadened and captured well with a

Dynes fit. The superconductivity is however fully gapped and consistent with a fit with no nodes suggesting there are no zero-energy quasiparticles, a conclusion also reached by recent thermal conductivity measurements that cemented its two-band character [174].

6.2.3 Magnetic Field Dependence

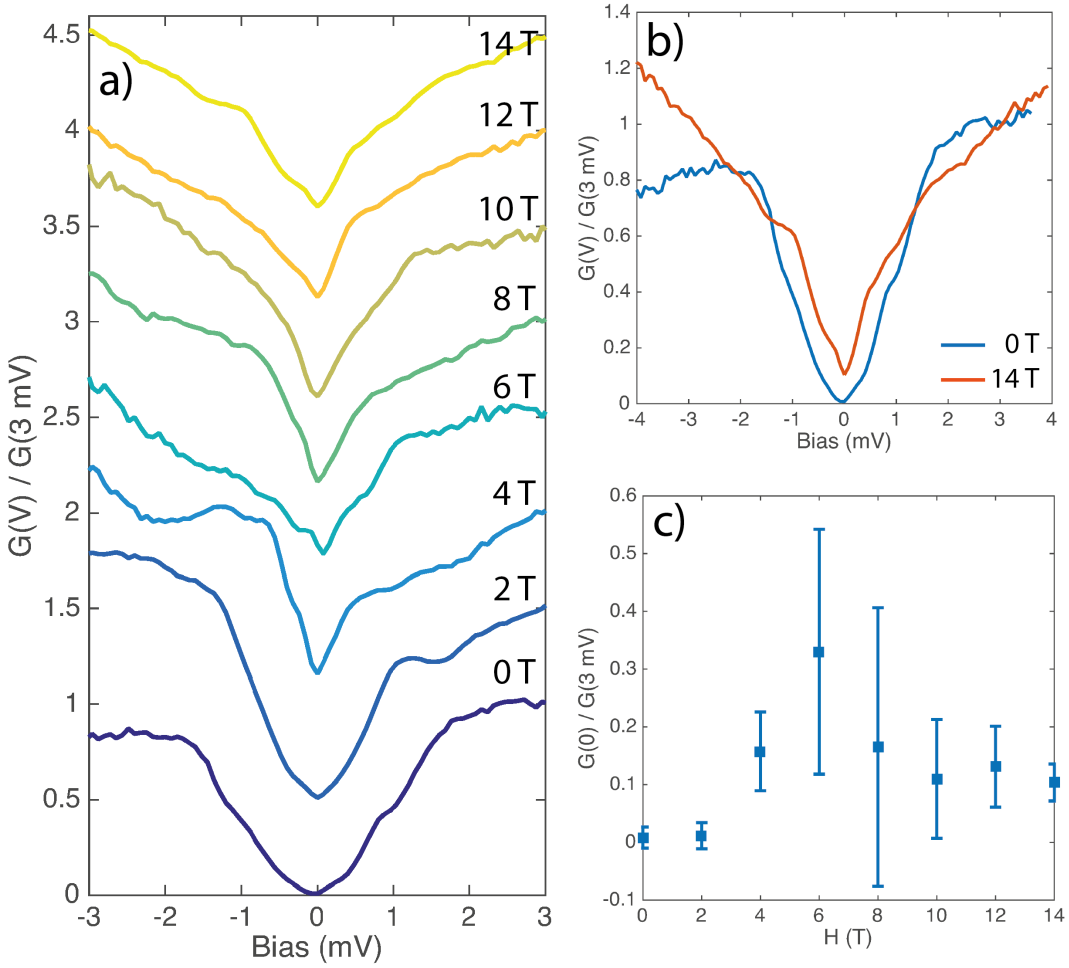

Figure 6.4: a) Field dependence of the superconducting gap in FeSe at 70 mK, taken as an average of 144 spectra over (3 nm)^2 using V_s = 8 mV, I_s = 0.4 nA and V_L = 50 μV. Each spectra is normalised to the conductance at 3 mV and offset vertically by 0.6 for clarity. b) Normalised spectra taken at 0 T and 14 T. c) Normalised zero-bias conductance plotted against applied magnetic field.

When a magnetic field was applied along the c-axis, the superconducting gap survived all the way to 14 T, where the spectrum was still gapped over 90%, compared to the fully gapped 0 T spectrum. This result appears to contradict the findings in P. Bourgeois-Hope's thermal conductivity measurements which claimed that FeSe reverts to the nor-

mal state at ∼14 T by comparing the residual thermal conductivity in magnetic fields to the estimated value from the Wiedemann-Franz law and their residual resistivity extrapolations for the normal state [174]. It does however appear to agree with their claim that the superconductivity is ultimately nodeless, where the zero-field spectrum in this work is fitted well with a nodeless model (anisotropic s-wave) and maintaining broadly the same spectral shape up to 14 T. There were considerations for sample quality, where their upper critical field values ranged from (13.3 ± 0.2) T up to (15.2 ± 0.2) T [174]. But even going for a high-quality sample with a ∼15 T critical field, one would expect significant suppression of the superconducting gap at 14 T. The superconductivity largely maintained its gap structure all the way to 14 T, with features consistent with the previously modelled two-gap character, with the larger primary gap having significant anisotropy and a smaller secondary gap. Both superconducting gaps have been found to be very anisotropic through superconducting QPI measurements by P. O. Sprau et al, with their gap maxima oriented orthogonally in momentum space and that these gaps have the opposite sign to one another; suggesting orbital-selective Cooper pairing in FeSe toward Fe d_{yz} orbitals [176].

The robustness up to 14 T would lead one to believe that FeSe is a superconductor, in whatever form, into far higher magnetic fields; potentially as high as 17 T as mentioned in Kasahara's investigation. However from this data it is not possible to define the nature of this 14 T superconductivity, such as an FFLO-like state which would have spatial variation in the order parameter and non-zero momentum Cooper pairs [172].

The next step would be to investigate whether there is, as one would expect, a vortex lattice at 14 T and whether the structure of the superconducting gap varies spatially. If the gap were to vary spatially, this could be considered evidence for an FFLO-like state, like in recent Josephson tunnelling STM measurements on $Bi_2Sr_2CaCu_2O_{8+x}$ by M. H. Hamidian et al, where they observed the spatial modulations in the superconducting gap size, attributed to density waves in the Cooper pair density (PDW) [177].

6.3 Conclusion

STM on FeSe showed atomically flat surfaces of the Se termination, with the characteristic iron-site dimer-like defects thought to be from iron-site vacancies. The superconductivity at 70 mK showed a fully gapped structure consistent with a 2 band model: with one band being very anisotropic, fitted with an anisotropy of 60% in a $\cos(4\theta)$ model with an average gap of $\Delta_1 = 1.4$ meV; as well as a smaller second gap of $\Delta_2 = 0.55$ meV.

FeSe was measured to maintain its superconducting gap at 70 mK all the way up to 14 T, with only a $\sim$10% reduction in gap depth at 14 T. The 14 T gap maintained largely the same structure as the 0 T gap, with the anisotropic shoulders and smaller second superconducting gap. The fact that the superconductivity persists up to 14 T contradicts recent thermal conductivity measurements [174], which claimed FeSe returns to the normal state at 14 T; giving credence to Kasahara's idea of a BCS-BEC crossover state between 14 and 17 T [172].

Further work to establish whether the vortex structure is affected at very high magnetic fields should be carried out to see whether the superconductivity behaves as normal, or whether it behaves strange enough to sit with the conflicting thermal conductivity [174][172] and STS measurements.

Chapter 7

Quasiparticle Interference in SmB_6

7.1 Introduction

7.1.1 Topological Kondo Insulators

Topological Kondo Insulators (TKIs) are a new class of materials that have gained significant interest, especially with regards to the unusual electronic behaviour of SmB_6. TKIs are a combination of the topological insulators realised in the theoretical works by Liang Fu, Charles Kane and Eugene Mele [178][179]; and heavy fermion compounds, which are themselves grounded in Kondo physics [10]. One of the great discoveries in this branch of condensed matter physics was that band insulators could themselves belong to topological classes, even if some are trivial. A standard band insulator is formed when the Fermi level of a material lies within an energy gap and one might expect that two band insulators with two different energy gaps and Fermi energies would be able to smoothly (adiabatically) deform into one another without breaking any symmetries. It was then discovered that this is not always possible because of the topologies associated with their ground-state wavefunctions [180]. This means that when a material with one topology meets another, such as a TI material having a boundary to vacuum, the symmetry must break or an energy gap must close to allow them to connect. For non-interacting topological systems, the only available option is for the energy gap to close up at the surface,

which would allow metallic conducting states to exist at the surface. These metallic surface states have been measured to have chiral spin textures in many compounds. Heavy fermion behaviour and its relation to Kondo physics has been discussed earlier in this thesis (UPt_3), but with the caveat that if the Fermi level lies within the hybridisation gap produced from the hybridisation of flat f-electron bands and the broader itinerant electrons, in a single-band material the system becomes an insulator: designated a Kondo Insulator (KI) [180]. The first Kondo Insulator discovered was SmB_6, where it was originally found to show no magnetic ordering down to 350 mK; which was considered unusual for the family of magnetic rare-earth hexaborides to which SmB_6 belongs [24]. Kondo insulators are sometimes described as semiconductors, in particular the metal to insulator transition behaviour in the d-electron Kondo insulator FeSi, which has often been called renormalised silicon due its remarkably similar behaviour to semiconducting silicon, but with much heavier electron-quasiparticle masses [181]. FeSi was a great demonstrator for the Kondo insulating effect, due to its large hybridisation gap of 60 meV ($\sim$ 750 K) being easily accessible at even room temperature [182] as well as its weak spin-orbit coupling [17]. Many other Kondo insulating compounds exist, including many rare-earth systems and it is ultimately the topological properties of their ground state wavefunctions that will define their additional non-trivial character and whether they will behave as TKIs or as humble KIs.

7.1.2 SmB_6

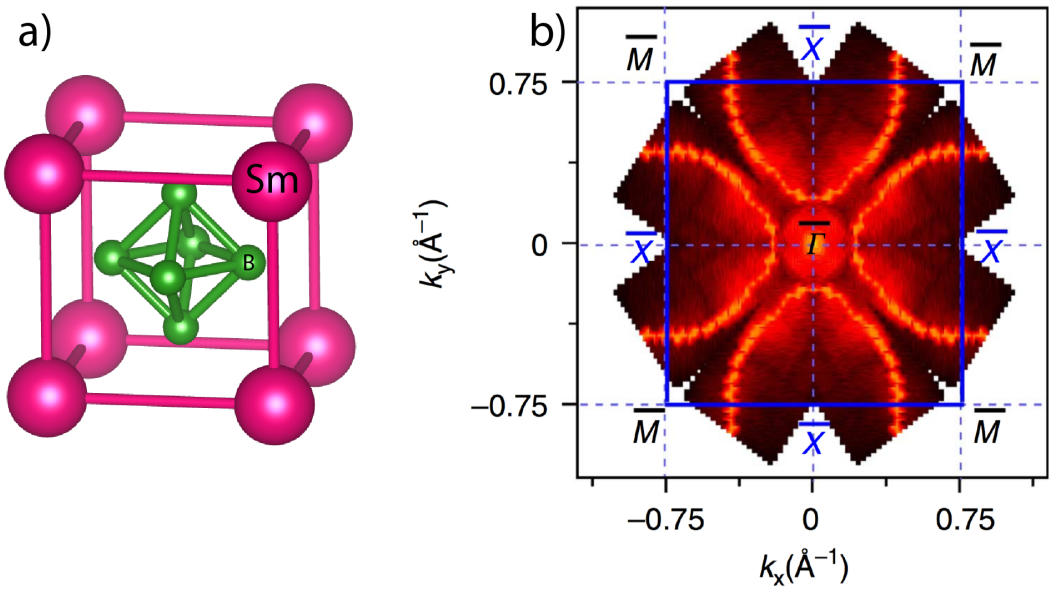

Figure 7.1: a) Crystal structure of SmB_6 where the cubic atomic lattice has an atomic spacing of a = 4.1327 Å at 100 K [183]. b) Fermi surface of SmB_6 as seen in ARPES at 6 K [184].

Samarium hexaboride (SmB_6) is a heavy fermion Kondo insulator with a cubic lattice of samarium atoms, enclosing an octahedron of boron atoms with a unit cell lattice spacing of a = 4.1327 Å [183]. Interesting behaviour was first spotted in SmB_6 by transport measurements, which saw that at temperatures below 50 K there is a sudden and significant rise in resistivity, due to the opening of the Kondo hybridisation gap, that saturates below 4 K [24][185]. This saturation in resistivity was first thought to come from impurity states in the bulk, however this residual resistivity did not improve with purer crystals as expected. The high residual resistivity was then proposed to come from metallic conducting states that only existed at the surface; which was backed up by Hall effect measurements that were thickness independent, with robust non-local transport that made SmB_6 a promising TKI candidate [186]. The electronic properties of SmB_6 are governed by the properties of the 4f and 5d bands and their hybridisation, which produces a hybridisation gap of the order of ∼15 meV in the bulk [187]. SmB_6 has been observed to have a mixed valence of $\simeq$ 2.5, which corresponds to a f-occupation averaging $\simeq$ 5.5 from the Sm^{2+} and Sm^{3+} states [188]; producing multiplets of 4f states in spectroscopy

that are often visualised as a large 4f resonance peak ∼15 meV below the Fermi level in ARPES studies [189] and as discrete peaks in STS [190][187].

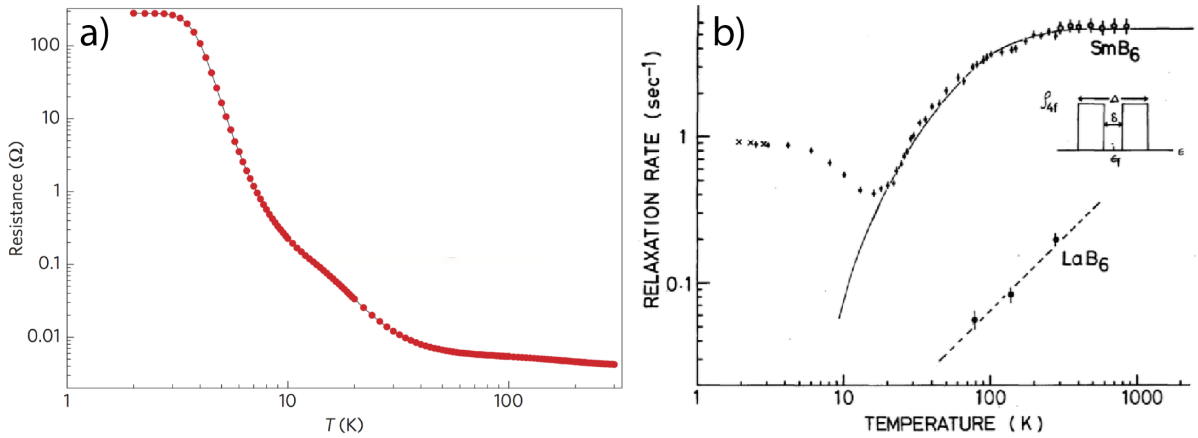

Figure 7.2: a) Plot of SmB_6 resistance versus temperature, showing the sudden rise below 50 K and plateau around 5 K, figure taken from [191]. b) NMR T_1 spin-lattice relaxation rate of SmB_6 as a function of temperature, compared with the good metal LaB_6, taken from [192].

The TKI theory proposed by M Dzero et al predicted the existence of a metallic surface state within the Kondo hybridisation gap, which explained the reported resistance saturation [193]. ARPES measurements have been reported to have revealed the in-gap surface states, structurally consistent with a theoretical topological model Fermi surface [184] and that these surface states are spin-polarised, with their spins locked to the crystal momentum, producing four surface pockets with chiral spin textures [194]. However there is still some controversy, since there are similar metallic states found simply from the d-f band hybridisation and that nobody has yet measured the Dirac cone at the surface that would confirm the topological nature of any metallic surface state [195]. In addition, much older NMR experiments on SmB_6, an overwhelmingly bulk measurement, saw a rise in $1/T_1$, the spin-lattice relaxation rate, below 10 K and saturation at 5 K; following the trends seen in resistance measurements [192][196][197]. Whilst the higher temperature behaviour could be explained by relaxation processes from the 4f states, the low temperature behaviour was believed to be caused by low-energy magnetic excitations that produce a temperature-independent relaxation rate. The magnetic excitations seen in NMR were not thought to come from the atomic lattice, but from some localised states that are

spread over several atomic distances which have small magnetic moments that would quickly disappear at higher temperatures. These magnetic excitations in SmB_6 would be very different to typical non-magnetic semiconductors and these localised states could open a low-temperature conductance channel that is often attributed to exotic surface states [192].

Recent STM/STS measurements on SmB_6 reveal the gradual opening of the Kondo hybridisation gap as the temperature is lowered, producing the characteristic Fano lineshape seen in similar heavy fermion materials like UPt_3 earlier in this thesis. The opening of this gap coincides with the enhancement of a coherence peak towards the left side of this gap that is suggested to be of magnetic origin [198]. Within the overall Fano structure sit several smaller resonances that can be seen on non-reconstructed surfaces without defects. These small resonances become sharper and enhanced likewise to lower temperatures, suggesting the possibility of an additional energy scale in SmB_6 [190]. STM/STS and in particular QPI at mK temperatures would allow the probing of these surface states with high momentum and energy resolution. Quasiparticle scattering between these surface states would allow their structure and indirectly their spin texture to be confirmed, through which vectors are not forbidden by spin-selection rules. Previous tight-binding models and their predictions for QPI concentrate on the topological surface states and their effects on low-temperature conduction and spin-textures [199][200][201]; however this work uniquely concentrate only on the effect of the bulk states and whether they can describe the quasiparticle and spectroscopic properties of SmB_6.

7.2 Mean-Field Hamiltonian

The tight binding model used in this investigation is based on the bulk mean-field hamiltonian used in the surface theory work by Bitan Roy et al [199]. The Hamiltonian contains on its diagonal two four-by-four sub-Hamiltonians for d-electrons, H^d, and f-electrons, H^f; with hybridisation terms between these orbitals in the off-diagonals, V_h. The compact version of this Hamiltonian is represented as:

$$H_{bulk}(\mathbf{k}) = \begin{pmatrix} H^d(\mathbf{k}) & V_h(\mathbf{k}) \\ V_h^\dagger(\mathbf{k}) & H^f(\mathbf{k}) \end{pmatrix}, \tag{7.1}$$

These d and f-electron orbital Hamiltonians are defined with the indices d and f respectively in $H^l(\mathbf{k})$ by:

$$H^l(\mathbf{k}) = \epsilon^l \hat{I}_4 + t^l \begin{pmatrix} \hat{\phi}_1(\mathbf{k}) + \eta_l \hat{\phi}_2(\mathbf{k}) & (1-\eta_l)\hat{\phi}_3(\mathbf{k}) \\ (1-\eta_l)\hat{\phi}_3(\mathbf{k}) & \eta_l \hat{\phi}_1(\mathbf{k}) + \hat{\phi}_2(\mathbf{k}) \end{pmatrix}, \tag{7.2}$$

where t^d and t^f are the hopping amplitudes and ϵ^d and ϵ^f are the likewise corresponding chemical potentials for the d and f electrons respectively. The above equation contains terms of the form:

$$\hat{\phi}_j(\mathbf{k}) = \hat{\sigma}_0 \phi_j(\mathbf{k}), \tag{7.3}$$

where $\hat{\sigma}_0$ and $\hat{I}_4 = \hat{\sigma}_0 \bigotimes \hat{\sigma}_0$ are respectively the two- and four-dimensional identity matrices; whilst the different components of the $\phi(\mathbf{k})$ functions are defined as:

$$\phi_1(\mathbf{k}) = \frac{1}{2}(c_x + c_y + 4c_z), \tag{7.4}$$

$$\phi_2(\mathbf{k}) = \frac{3}{2}(c_x + c_y), \tag{7.5}$$

$$\phi_3(\mathbf{k}) = \frac{\sqrt{3}}{2}(c_x - c_y), \tag{7.6}$$

with $c_\alpha = \cos k_\alpha$, for $\alpha = x, y, z$. For everything following, the lattice is simplified to having a spacing of $a = 1$. The hybridisation matrix is then defined as:

$$V_h(\mathbf{k}) = \frac{V}{4}\begin{pmatrix} 3(\bar{\sigma}_x - \bar{\sigma}_y) & \sqrt{3}(\bar{\sigma}_x + \bar{\sigma}_y) \\ \sqrt{3}(\bar{\sigma}_x + \bar{\sigma}_y) & \bar{\sigma}_x - \bar{\sigma}_y + 4\bar{\sigma}_z, \end{pmatrix}, \tag{7.7}$$

where $\bar{\sigma}_\alpha = \hat{\sigma}_\alpha \sin k_\alpha$ for $\alpha = x, y, z$ and $\hat{\sigma}_{x,y,z}$ are the standard two-dimensional Pauli matrices. The bare hybridisation amplitude is represented by V. This work restricts itself to hole-like f states, i.e. $t^d t^f < 0$. In Bitan Roy's work, the parameters chosen to demonstrate their model were: $t^d = -2$ eV, $t^f = +0.05$ eV, $V = 0.0365$ eV, $\eta_d = -0.3$, $\eta_f = -0.29$, $\epsilon^d = 0.2$ eV$-3t^d(1+\eta_d)$, $\epsilon^f =$ -0.01 eV$-3t^f(1+\eta_f)$. In the original paper by Bitan Roy, the parameters t^d and t^f had their signs swapped and were originally assigned as 2 eV and -0.05 eV respectively, which yield a different band structure to their own plots as well as existing literature [195].

7.2.1 Band Structure From Published Values

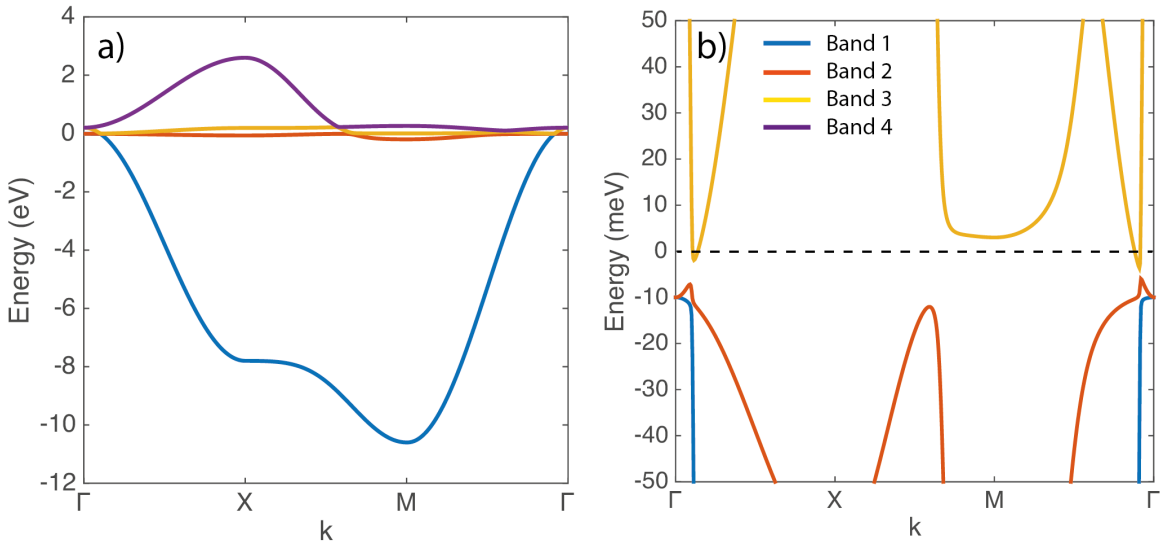

Figure 7.3: Calculated bulk band dispersion of SmB_6 showing a) the full dispersion and b) the dispersion between ±50 meV using the incorrect but published parameters $t^d = 2$ eV and $t^f =$ -0.05 mV.

7.2.2 Solving Numerically

In order to solve this mean-field Hamiltonian numerically, a k-space grid was introduced where $k_z = 0$ and k_x and k_y run between $-\pi/a$ and $+\pi/a$ for the first Brillouin Zone.

For the band structure results shown below, the k-grid has 401^2 points and the lattice spacing, a, is normalised to $a = 1$. The mean-field Hamiltonian is then applied to this grid, where each element in the two-dimensional k-space matrix defines a k-vector $(k_x, k_y, 0)$. By numerically diagonalising and obtaining the eigenvalues and eigenvectors for each k-vector, an output matrix is produced where each k-space point is associated with eigenvalues and an eigenvector. The overall Hamiltonian is 8-by-8 and therefore produces 8 eigenvalues and an 8-component eigenvector associated with the 8 energy band solutions.

7.3 Results

7.3.1 Band Structure

The band structure is obtained from the eigenvalues of the Hamiltonian at each point in k-space and taken as line cuts along the high-symmetry directions.

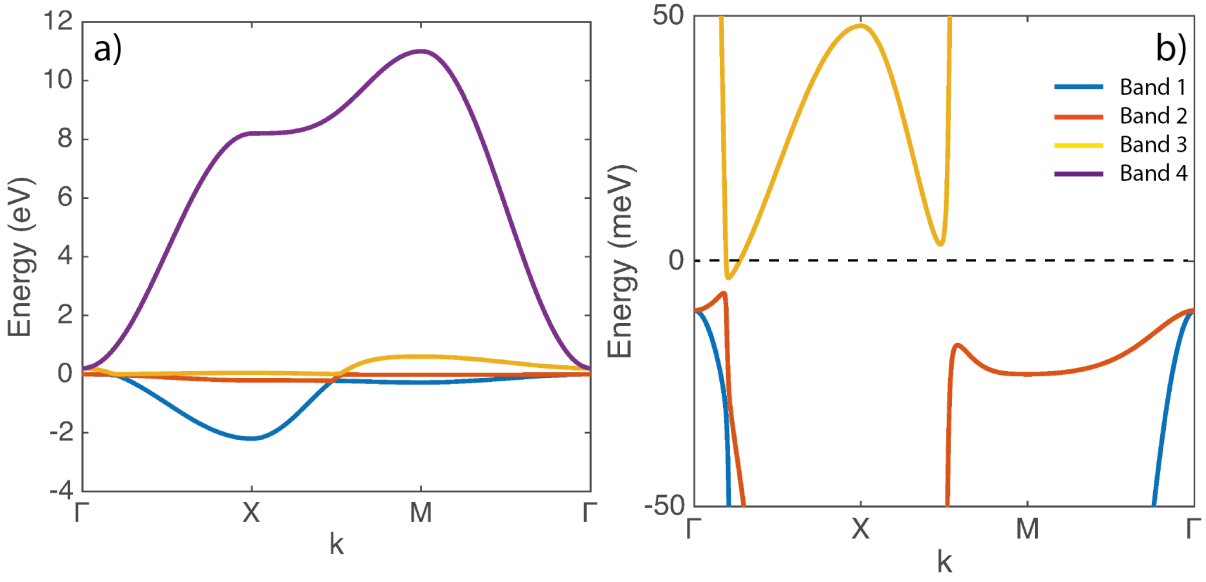

Figure 7.4: Calculated bulk band dispersion of SmB_6 showing a) the full dispersion and b) the dispersion between ±50 meV.

It can be noted that because of the symmetry of the Hamiltonian, only four of the bands appear to be unique, with each band having a copy. The hybridisation gap is visible

in the band structure with an apparent width of about 5 meV around the Γ point. In this model there are two strongly dispersing d-bands, shown in purple and blue, and two f-bands which lie flat and are shown in red and yellow. Upon zooming into a small energy range of ±50 meV around the Fermi level the effect of the hybridisation terms can be seen between the d and f-bands.

7.3.2 Fermi Surface

In order to visualise the Fermi surface and energy cuts through k-space, the matrix of eigenvalues had to be discretised to produce shapes of a finite thickness. The k-space grid was then sub-divided into 200 bins to each an over-sampling ratio for the original k-states of 2:1 to reduce the risk of any under-sampling effects and reduce computational time for later analysis. Since there are 8 (4 unique) bands in the system, an additional orbital-character weighting term is effectively introduced by instead of simply counting +1 if the (E, k_x, k_y) point is within the histogram pixel, the weight of that point is tallied by adding the magnitude of the eigenvector components of each of the bands for that state. This allows one to see in energy cuts how strong the orbital-character of the features are and how that changes with energy. The energy axis is divided into bins of equal 5 meV width order to produce finite and visible band structures along this axis.

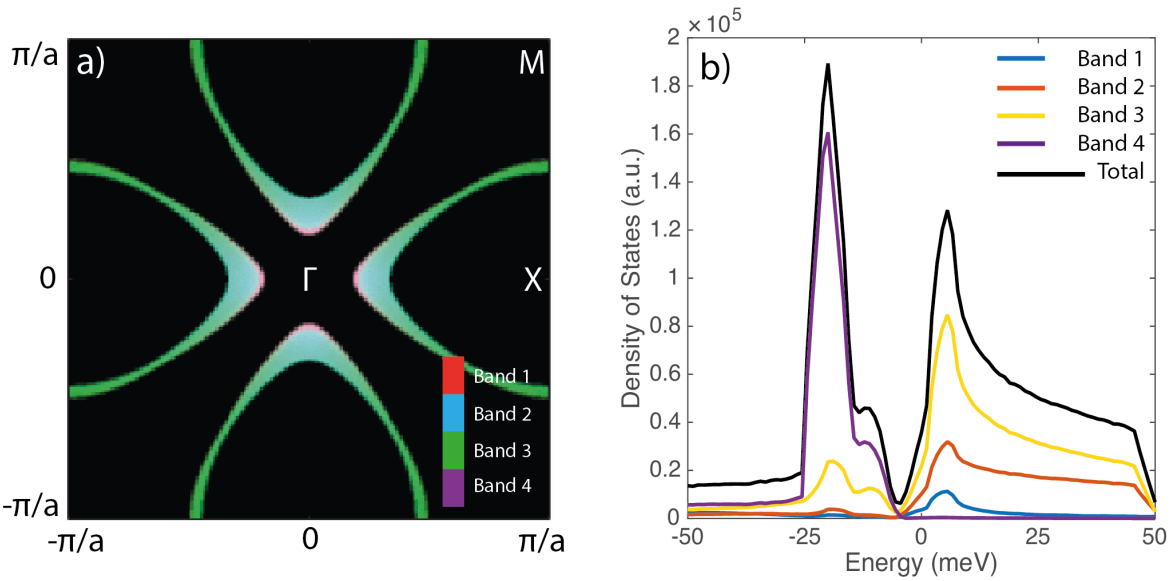

Figure 7.5: a) Fermi surface of the SmB_6 model with orbital character for the four unique bands visualised as four separate colours: red, cyan, green and magenta for bands 1-4 respectively. The reciprocal lattice vector length, $\pi/a = 0.7602$ Å^{-1}, where the unit cell length is derived from X-ray studies [183]. Fermi surface here is averaged over a ± 5 meV energy range to capture the pockets around the X points. b) Effective density of states of the system using ± 2.5 meV energy resolution.

An energy cut at 0 meV produces the Fermi surface shown above. The high-symmetry directions are labelled and the orbital character is displayed as hues of colour in cyan, green, magenta and red. An effective measure of the density of states is also plotted, calculated by counting the number of states that lie in these histogram bins, summed over all k-states for each energy. This density of states plot mimics the characteristic STS spectra seen in many studies on SmB_6 [190], where there sits a large peak beneath the Fermi level with a significant hybridisation gap of $\sim$ 20 meV width; with an overall shape that appears akin to a Fano resonance in STS. The peaks in the density of states and likewise in STS, can be seen to come almost entirely from the f-bands in the system. By comparing the energy scale at which the f-bands in the calculated band structure turn over, it is obvious that the strongly enhanced density of states of these flat f-states dominate the density of states structure and likely any spectroscopic features in the following analysis. The Fermi surface itself appears in this model as four elliptical pockets at the X points when a greater energy window is averaged over, consistent with the ARPES measurements such as by M. Neupane et al, that captured all the low energy

states in a ±4 meV window due to the inherent resolution limit in ARPES [184].

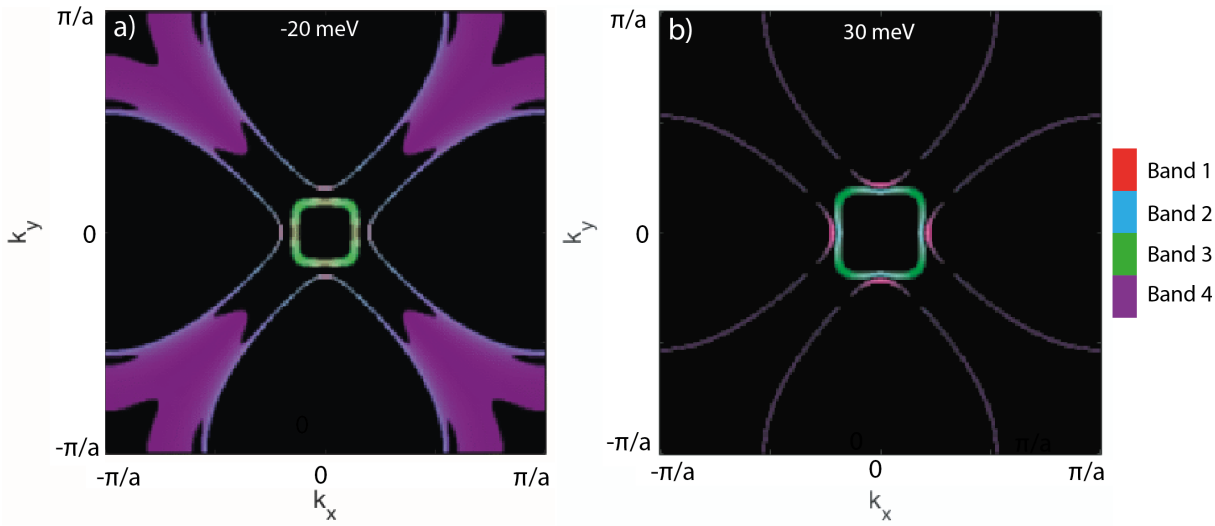

Figure 7.6: Energy cuts at a) -20 meV and b) 30 meV in the Brillouin Zone of SmB_6, visualised with orbital character colours.

The energy cuts show the presence of the elliptical hole-like pockets at the X-point which shrink towards the Fermi level and similar structures above the Fermi level which have electron-like dispersion. The effect of the hybridisation can be seen in the energy cut at +30 meV, where the green central square shape is distorted by the surrounding pink coloured bands.

7.3.3 ARPES Comparison

The band structure calculated here can be compared to the dispersion of bands measured in ARPES. Along the Γ-X direction the dispersion is seen as the two f-bands and a single very steep d-band, whereas along M-X only the f-bands can be seen. By looking at the location of the f-band turnovers, it is noticeable that the calculated band structure appears to be ∼20 meV above the ARPES bands measured by E. Frantzeskakis et al. The modelled lines in the ARPES figures are taken from F. Lu et al that utilised a bulk Local-Density Approximation (LDA) + Gutzwiller theory, but required a one-third renormalisation of the 4-f states to fit the measured band structure and also a rigid vertical shift of 20 meV in binding energy to account for the suspected difference in the

chemical potential (Fermi energy) between the data and the model [202][195]. It is likely that this shift in the chemical potential mismatch of 20 meV also explains the offset in this work compared to ARPES.

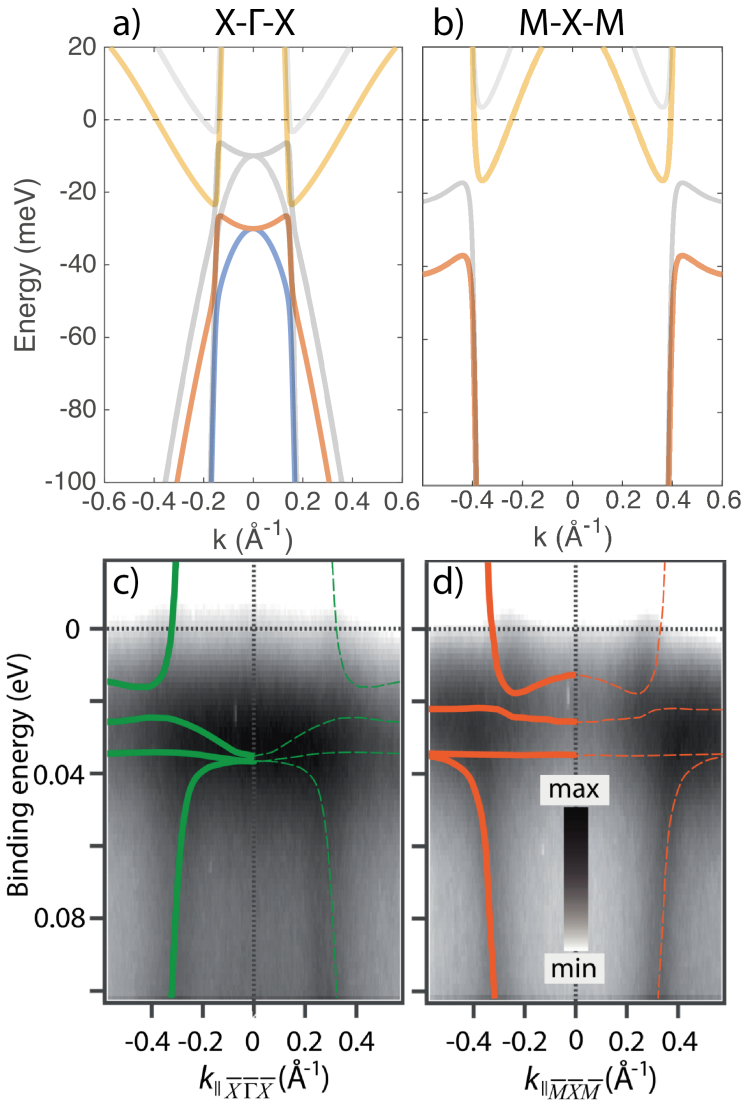

Figure 7.7: a,b) Calculated band structure along select high-symmetry directions. c,d) LDA + Gutzwiller theory calculations laid over ARPES data taken at $k_z = 6\pi/a$ ($h\nu$ = 70 eV at T = 38 K) on the SmB_6 (001) terminated surface; ARPES figures taken from [195]. The calculated band structure pre-shift is shown in greyscale.

The most striking features in the ARPES data are the steeply dispersing bands which are likely from the d-bands. There is a flat band of intensity in the ARPES data consistent with the other flat hybridised f-bands as they turn over, however the small band minima just below the Fermi level are barely resolvable. It is then from this ARPES work that the model used in this investigation can be considered largely accurate in describing the bulk

states in SmB_6. To take into account the 20 meV shift needed to compare the ARPES with F. Lu et al, the Fermi surface is plotted again below but at an energy cut of +20 meV:

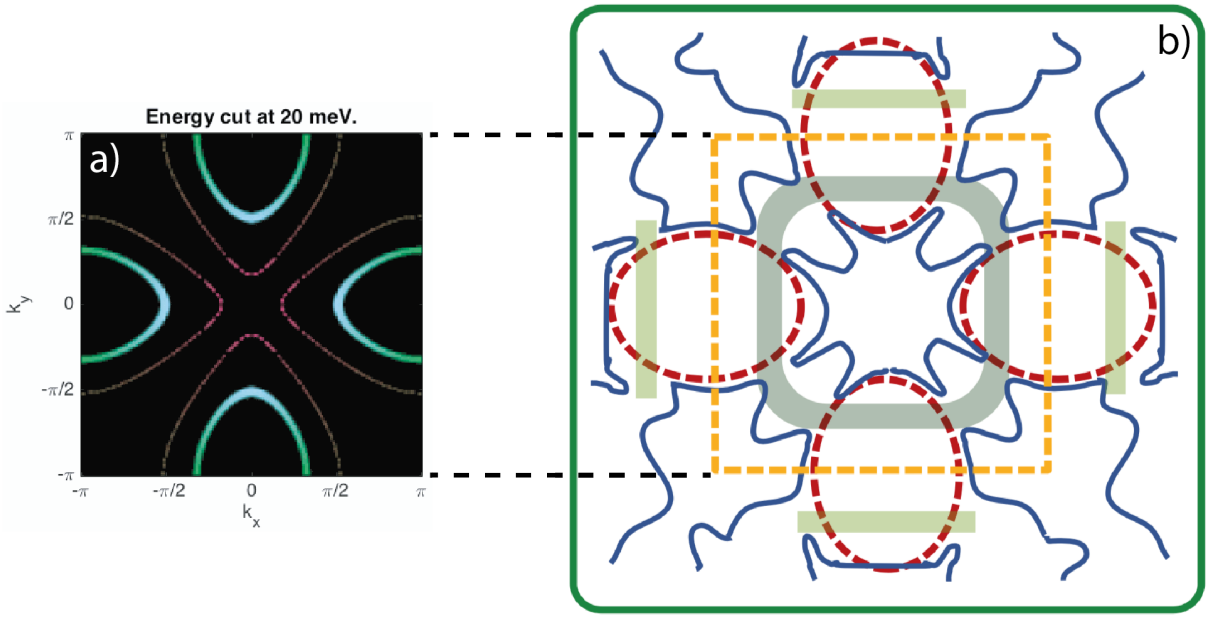

Figure 7.8: a) Calculated energy cut at 20 meV, which due to the reported 20 meV shift in binding energy as seen in ARPES, represents a more accurate Fermi surface of SmB_6 in this model. b) Schematic diagram of the Fermi surface of SmB_6 with the non-hybridised bands in dashed lines and hybridised bands in solid lines. The 1st Brillouin zone is shown as the dashed yellow square and the hybridisation gap from the 5d-4f band hybridisation is shown as solid green. Figure taken from [195].

With the 20 meV shift, the model matches quite well with the schematic in the figure above as well as the typical Fermi surface seen in ARPES measurements [184][203]. There is some discrepancy between the calculated band structure and the ARPES measurements in terms of the lateral scaling, where it can be seen that the strongly dispersing bands fall at greater wave-vector values in ARPES, as well as the wider hybridised states. The band structure overlaid on the ARPES data incorporated a one-third renormalisation of the f-bands, something not taken into account in the tight binding model, which can explain the lateral differences in the band structure.

7.3.4 Experimental Data

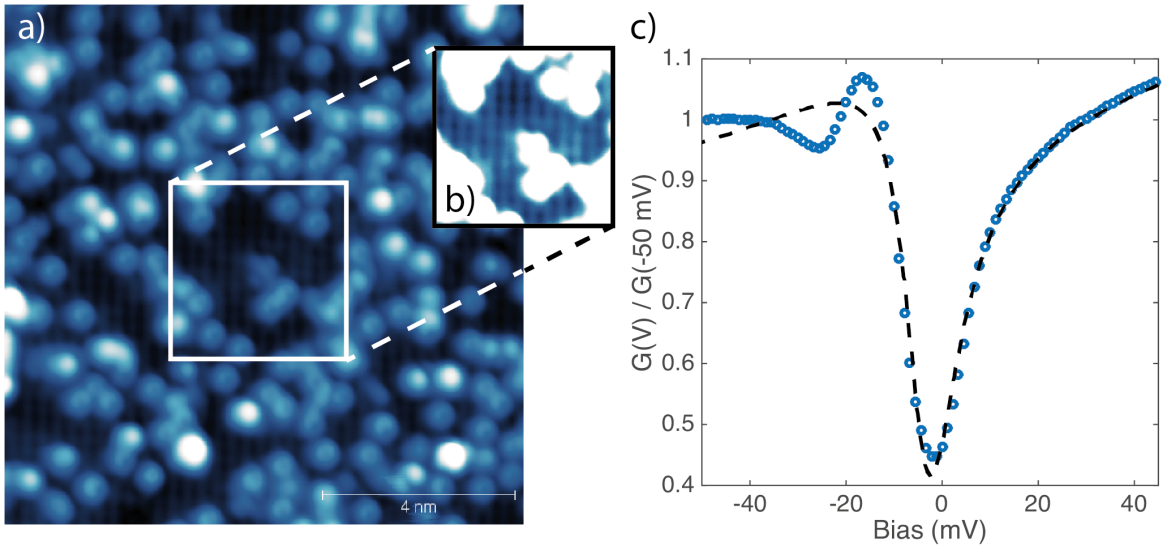

Figure 7.9: a) Topograph of the Sm terminated surface with typical abundance of boron clusters on top, obtained using V_s = 200 mV and I_s = 0.05 nA b) Contrasted section of the surface to emphasise the square atomic lattice underneath. c) Normalised average spectrum of SmB_6 taken as an average over 100^2 spectra over an area of $(10\ nm)^2$ using V_s = 50 mV, I_s = 0.5 nA and V_L = 5 mV. Data taken at 8 K and in zero-field. The spectrum was fit with a Fano line-shape, which produced Γ = 6.64 meV and q = -0.288.

SmB_6 was cleaved to reveal a Sm terminated surface with clusters of boron. This SmB_6 data was measured by Z. Sun and A. Maldonado in the Wahl group at the Max Planck Institute for Solid State Research (MPI-FKF) in Stuttgart. The spectrum at 8 K of SmB_6 is fit very well with a Fano line-shape as expected for a heavy fermion compound, producing from the least squares fit a width Γ = 6.64 meV and a Fano asymmetry parameter of q = -0.288. This energy scale of the Fano width is comparable to the 50 K temperature where the resistivity in SmB_6 begins its rise, where $\Gamma \sim k_B T^*$ produces T^* $\sim$ 77 K.

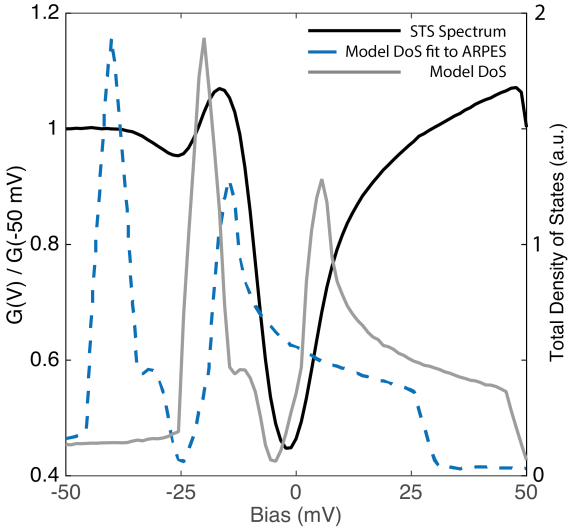

Figure 7.10: Plot of the average spectrum from the SmB_6 QPI map alongside the total density states from the tight binding model.

The measured spectrum is consistent with the unshifted tight binding model density of states, with the hybridisation gap aligning very well with the Fano resonance. The peak at ∼-15 mV on the negative edge of the hybridisation gap aligns with the peak in the spectrum, which can be attributed to the hybridised f-states. The rigid shifted model fails to describe the STS of SmB_6, suggesting the chemical potential seen at the surface of the ARPES measurements [195] is different to what is measured in STM/STS. The ARPES measurements by E. Frantzeskakis et al did not identify which exact termination they were measuring on, when SmB_6 is theorised to have different surface spectroscopic properties depending on whether the cleave termination is polar or non-polar, including just whether the termination is at the Sm or B layer. Density functional theory (DFT) calculations by J. Kim et al predicted band structure changes on the order of 20 meV depending on whether there is a Sm termination or a B termination, which can provide metallic states in the hybridisation gap [204]. Similarly, a combined ARPES and DFT study by Z. -H. Zhu et al explained the metallic surface states with the coexistence of Sm and B terminations with differing polarity, but with much greater spectroscopic energy shifts on the order of an electronvolt [205]. The STM/STS data here was measured on the Sm termination, but it is unknown whether this is the same as the ARPES measurements the band structure is compared to; making it difficult to identify the cause

of the apparent chemical potential difference. Outside of the hybridisation zone, the model fails to describe the rest of the spectroscopy, likely due to the simplicity of the bulk model that only considers the hybridisation effects.

7.3.5 Experimental QPI

QPI was then measured on the surface shown above on the Sm (100) termination; the data was symmetrised to improve signal to noise and filtered with a low-pass filter. To produce something that would be comparable to QPI data, the histogram of the energy cut data obtained from the model is processed using an autocorrelation. The autocorrelation effectively produces an output image of all the possible scattering amplitudes that would be seen in QPI. Ignoring selection rules, the energy cuts were transformed to a greyscale image where individual orbital character is no longer included, but still contributes towards the intensity of the states. All the data obtained from the mean-field calculation from now on is rotated 45 degrees to match up with the experimental data which displayed its Bragg peaks in the diagonal of its images. A few examples of comparing the calculated QPI from the mean-field Hamiltonian and real QPI data taken on SmB_6 from the MPI-FKF are shown below.

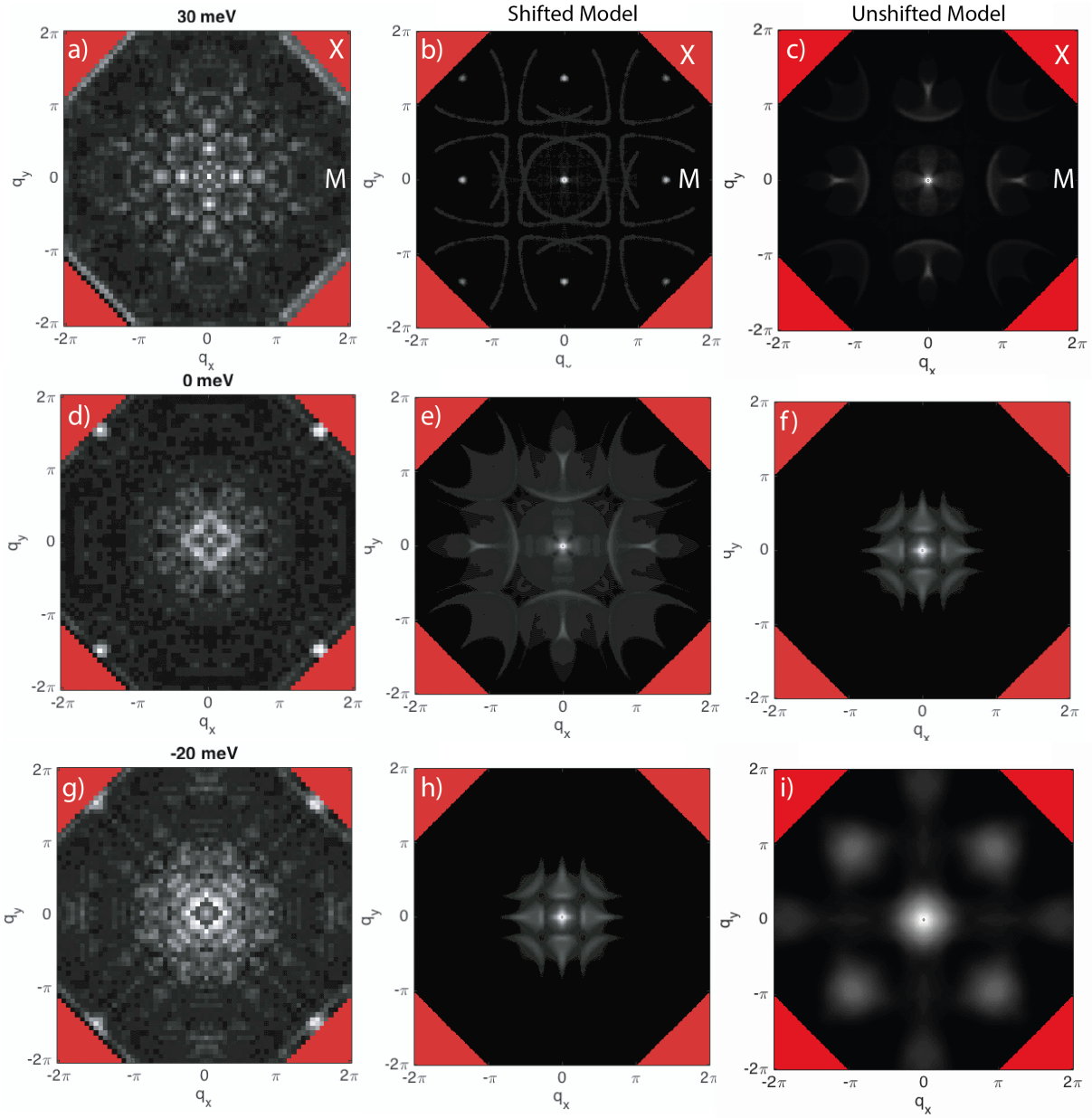

Figure 7.11: Comparison between measured QPI data and the tight binding model QPI at 30 meV (a,b,c), 0 meV (d,e,f) and -20 meV (g,h,i) for both shifted and unshifted models. The real QPI data for SmB_6 taken at 8 K and in zero-field. The calculated data is rotated 45 degrees and has had a Gaussian subtracted from it with standard deviation 1 and height corresponding to the maximum data point in the energy cut to improve contrast.

From the figures comparing the measured QPI and the model, both including or excluding the 20 meV shift in energies advocated by E. Frantzeskakis et al, there is no total agreement in the structure of the data. Since the model used in this work was merely a bulk Hamiltonian, there is the possibility that what is seen in QPI, which is inherently a surface technique, are states not included in the bulk model. There is also the fact

that STM is more sensitive to d-orbitals than f-orbitals due to their greater delocalisation, therefore biasing the signal towards the d-states, whereas the model treated the d and f-states equally (but weighted for orbital character). From the QPI layers alone it is difficult to decide whether the unshifted or shifted regime fits better, but since the spectroscopy was best matched by the original unshifted model; the unshifted model is used in the rest of this chapter.

7.3.6 QPI Dispersion

Taking cuts along the two high-symmetry directions in the simulated and measured QPI data allows one to visualise in q-space the dispersive band structure.

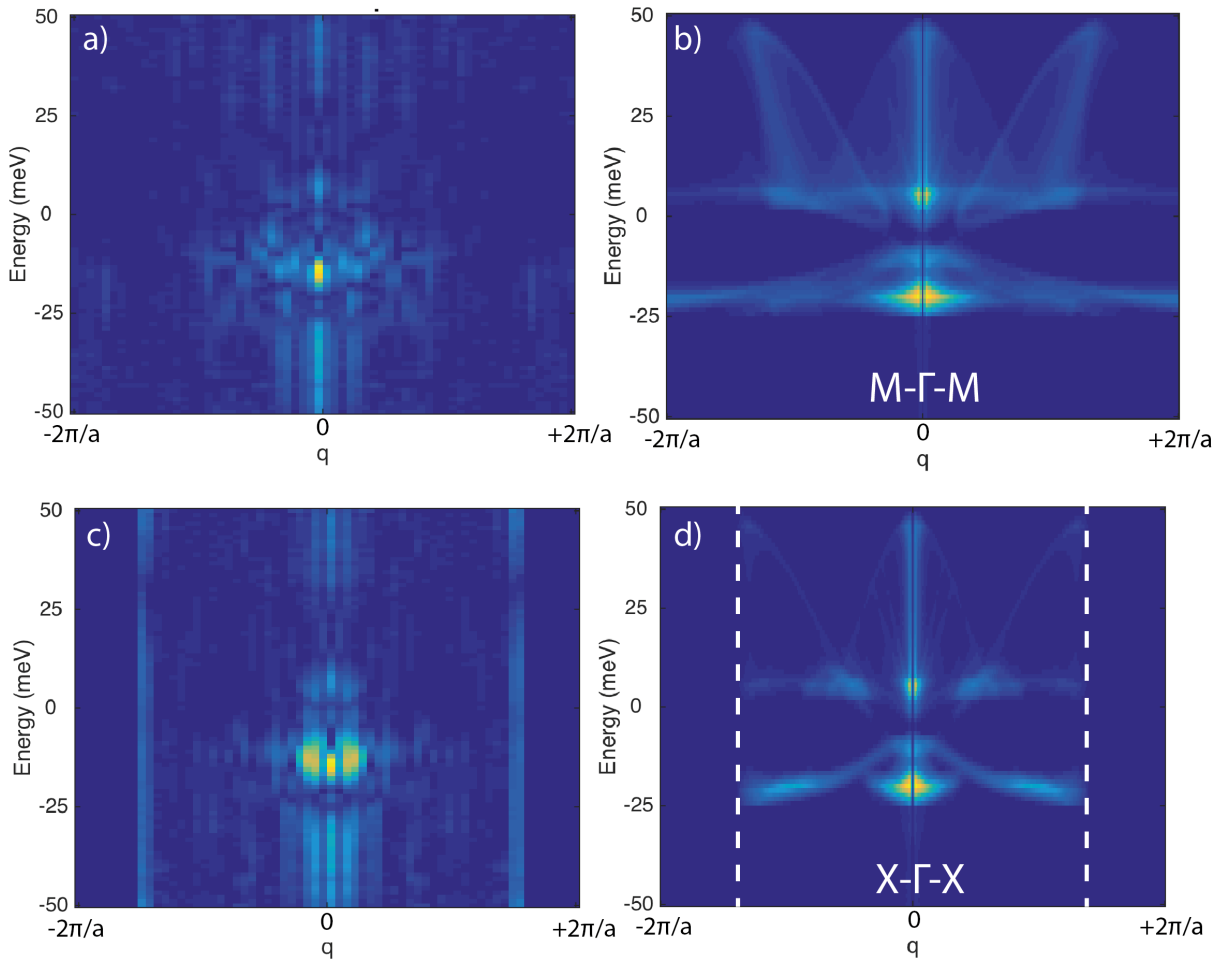

Figure 7.12: Comparison between the dispersions extract from the measured QPI data and the tight binding model along the Γ-M direction (a,b) and Γ-X (c,d).

For the unshifted dispersion, there are many similarities between the model and the experimental data. There are bright lobes of intensity at both edges of the hybridisation gap, which sit at approximately -20 meV and +5 meV, with the negative edge lobe being the most intense in both experiment and theory. As mentioned earlier, these hybridisation gap edges are a product of the d-f hybridisation with greater intensity on the negative edge where the flat f-states sit. The hybridisation gap is clearly visible in the model and experiment as a region of reduced intensity between the two lobes. However there does appear to be more signal and therefore states in the hybridisation gap in the measured QPI compared to the bulk model. Much further above the hybridisation gap, there does appear to be some evidence of the highly dispersive d-states where vaguely parabolic structures can be seen. These d-states are much weaker than the f-states, as expected from intuition. Further below the hybridisation gap, where the model predicts flat wings from the f-states, there is less consistency with the QPI data. Whilst there is a relatively wide structure, it does not reflect the full extent of the f-states; likewise for the shelf of states on the positive edge of the gap. The column of intensity in the measured data below the hybridisation gap matches the width of the central lobe, suggesting this signal may be from the lower f-states; however the full extent of this column of states is not seen in the model. Overall the model QPI matches the data very well, suggesting that the majority of the QPI structure can be explained by bulk states, which do not need the rigid energy shift deemed necessary in ARPES [195]. The one-third renormalisation of the f-bands could improve the model by more accurately simulating the states around the hybridisation gap, although it is not obvious which features in the QPI/model would benefit.

7.3.7 Orbital Decomposed QPI

Separating out the d and f-orbital contributions to the simulated QPI allows one to visualise which QPI features can be attributed to what kind of orbital phenomena. f-bands have much shallower dispersion and therefore produce a much greater density of states than d-bands. Something which can overwhelm the contrast of the two, making

the d band contributions harder to see.

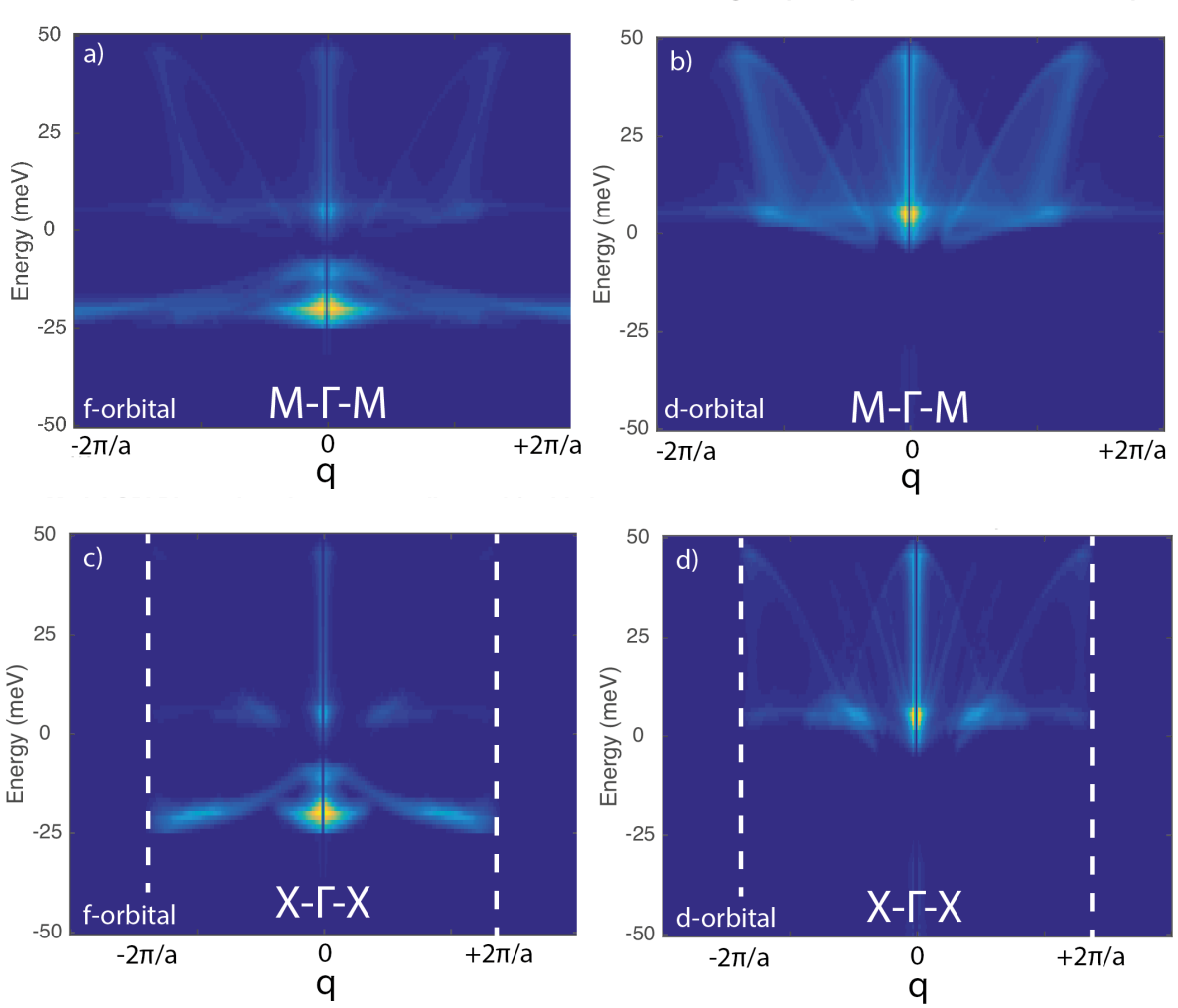

Figure 7.13: Orbital separated QPI simulations: a) f-orbital QPI along Γ-M, b) d-orbital QPI along Γ-M, c) f-orbital QPI along Γ-X, d) d-orbital QPI along Γ-X.

Decomposing the d-orbital contribution out of the QPI dispersion, leaving just the f-orbital contribution demonstrates that the flat wing structures below the hybridisation gap are from the f-bands. The lobe below the hybridisation gap is present in this f-only representation, suggesting that below the hybridisation gap, the f-bands dominate the QPI signatures in SmB_6 as well as spectroscopy. On the other hand, decomposing to leave the d-states demonstrates that the parabolic and light-band states are from the d-bands. Likely from the hybridisation, it produces another flat shelf of states at the positive edge of the hybridisation gap as well as a small and intense lobe of states. This intensity at the positive edge of the hybridisation gap is seen with great clarity in the measured QPI data. Since d-orbitals are much more delocalised than f-orbitals, STM is

likely to be much more sensitive to these d-states as opposed to f-states. There do appear to be more states within the hybridisation gap than what is seen in the bulk tight binding model, which could either be explained by surface states, possibly topological ones, that are not featured in the bulk model; or even just from a difference in the hybridisation strength or the renormalisation of the f-bands, as done by E. Frantzeskakis, where their model required a one-third extra renormalisation to match their ARPES data [195].

The ARPES measurements by E. Frantzeskakis et al showed that the X states at the surface of (100) SmB_6 were metallic, which opposes the idea that, at least in the bulk, the system is gapped as a Kondo insulator. These X states were concluded to not be topological nor to be sitting in the Kondo hybridisation gap from their measurements, in conjunction with quantum oscillation measurements on the Fermi surface areas [206]. There is the possibility that the chemical potential could be different at the surface than in the bulk, as demonstrated in the rigid 20 meV shift downwards in binding energy in their ARPES data, but deemed unnecessary in this chapter. The ARPES data saw that the Fermi level sat 20 meV above lowest-lying d-f hybridisation gap, whereas in the bulk the Fermi energy sits in the hybridisation gap to make it a Kondo insulator (KI). Differing chemical potentials at the surface, producing metallic behaviour, would create a conduction channel that could explain the plateau in its resistivity [195]. The fact that such a shift in the chemical potential was not needed in this STM work could suggest that either the ARPES measurements were taken on a different termination than the Sm termination used here, since the ARPES data shown earlier had an unknown termination; or the fact that their measurements at 38 K produced different surface properties than the 8 K STM/STS work, since 38 K is not that far into the Kondo regime of this material. However, this work arrives at the same conclusion that the behaviour of SmB_6 can be explained simply through bulk phenomena rather than topological surface states; although there was not enough resolution for the QPI states within the hybridisation gap to ascertain their presence and distinctiveness from the bulk signatures.

7.4 Conclusion

The bulk tight binding model used in this chapter [199] was able to reproduce the band structure observed in SmB_6 ARPES measurements by E. Frantzeskakis [195], after taking into account a 20 meV rigid shift of the band structure to greater binding energy. This rigid shift represents a different chemical potential at the surface compared to the bulk in the work by E. Frantzeskakis and was necessary to produce the correct Fermi surface and explain the topologically trivial metallic surface states seen in the ARPES measurements. However for spectroscopy and QPI, the rigid shift does not work and successfully models the data without it. Spectroscopy on SmB_6 produced the typical Fano line-shape seen in heavy fermion compounds, with a characteristic energy width $\Gamma = 6.64$ meV and an asymmetry parameter q = -0.288, consistent with a hybridisation gap width of $\sim$25 meV. A peak in the STS spectrum coincides with the negative edge coherence peak of the hybridisation gap in SmB_6 from the f-states, reproduced in the bulk model.

QPI calculations based on the tight binding model followed the measured QPI data very well, with lobes of intensity on the edges of the hybridisation gap seen in both cases, with particular intensity from the f-states. Signatures of the wider f-states beneath the hybridisation gap are visible, but not the full structure as predicted. There is some evidence for quasiparticle states within the hybridisation gap, with non-zero intensity seen between the edges of the hybridisation gap that isn't fully accounted for in the bulk model. This work therefore does not rule out the role of topological surface states within the hybridisation gap, however the bulk model describes remarkably well the rest of the QPI data.

The topological surface states predicted in SmB_6 should have a spin texture, therefore spin-polarised STS-QPI would be able to potentially measure this since backscattering should be forbidden and a comparison with the data in this chapter could help determine the nature of the in-gap states. The fact that the bulk model describes the data so well,

it is not unreasonable to agree with E. Frantzeskakis that the material becomes metallic at the surface without any topological nature. Likewise, the conclusion from early NMR work that suggested that localised electronic states with small magnetic moments seen in the bulk could explain the low-temperature resistivity and spin-lattice relaxation rate plateaus; and therefore the inherent bulk character of the phenomena seen in SmB_6.

Chapter 8

Conclusion

In this thesis I have shown how scanning tunnelling microscopy and spectroscopy (STM/STS) can be used to investigate the superconducting and electronic properties of four different quantum materials. Two of these materials are heavy fermion compounds, three are superconductors and three are theorised or measured to have topological surface properties. The high electronic and momentum resolution afforded in STM/STS has allowed the probing of quasiparticle states near the Fermi level and their dispersion from the underlying band structure.

In chapter 4, I demonstrated how the heavy fermion behaviour in UPt_3 produces a characteristic Fano line-shape, with Fano parameters that vary with the atomic lattice; strongly similar to URu_2Si_2 [97][96]. Alongside the Fano structure, sit signatures of inelastic tunnelling with a particular strong signal at 20 meV which is found to be consistent with phonon excitations, in particular a A_{1g} Pt breathing phonon [104]. Matching past optical reflectivity measurements [105], a small gap-like structure is found above the Fermi level that is consistent with a pseudogap formed from an f-f inter-band transition. No superconducting gap was detected, which could be an effect of p-wave superconductivity being suppressed at the surface, since recent sample characterisation measurements from the same batch gave a critical temperature of $\simeq 550$ mK, indicating high sample quality. QPI measurements did not produce strong quasiparticle signatures, but did reveal evidence of light electron and hole-like bands at the Fermi level, with band edges consistent with

high-resolution ARPES measurements of the f-states [98].

In chapter 5 I showed that the surface of $PdTe_2$ has strong defect and quasiparticle signatures with symmetries that match the underlying lattice as 3-fold and 6-fold symmetric. Spectroscopy showed that a density of states profile characterised by large resonances corresponded to band extrema as seen in ARPES and predicted in DFT calculations [130][133]. The superconductivity was found to be conventional BCS type-II, with a gap size of the order $\Delta \simeq 215$ μeV and signatures of anisotropy. The upper critical field was found to be of the order of 20 mT and the vortex state showed a coherence length of the order of 175 nm. This type-II behaviour contradicted recent magnetisation and susceptibility measurements that suggested strong type-I behaviour with enhanced surface superconductivity. The strong quasiparticle signatures were revealed in QPI to correspond to scattering from the topological surface states in $PdTe_2$. In particular a scattering vector of length 0.55 $Å^{-1}$ produced CDW-like features, nucleated at lattice vacancies; however fully explained by QPI and no CDW has been seen in ARPES and other techniques in $PdTe_2$. The intensity hierarchy and q-space structure of the scattering vectors are well explained by the chiral spin texture of the TSSs, suggesting that a link between the ubiquity of topological behaviour in the transition metal dichalcogenides and QPI. However the strong topological character coexisted with ordinary BCS superconductivity, calling into question some theories of engineered topological superconductivity.

In chapter 6 the high field superconducting properties of the iron-based superconductor FeSe were measured. Surfaces showed the characteristic iron-site dimer-like defects and their quasiparticle shadows. The superconducting gap in zero-field at 70 mK showed strong 2 band character with the larger gap having significant anisotropy consistent with previous studies [175]. FeSe was found to still have superconducting gap at 14 T, contradicting mK thermal conductivity measurements that suggested it returned to the normal state at this field [174] and perhaps supporting the BCS-BEC crossover idea proposed by Kasahara [172]. However further measurements on the vortex state are needed to fully characterise this high field superconductivity.

In chapter 7 I showed that a bulk tight binding model of SmB_6 was able to well describe

the band structure seen in ARPES [195], once including a rigid shift corresponding to a change in chemical potential between the surface and the bulk; but not necessary to describe the spectroscopy and QPI. Calculated QPI images matched the measured QPI with reasonable accuracy and suggesting that the quasiparticle signatures in SmB_6 are from the hybridised d-states and f-states from the bulk band structure. Conductivity was seen within the hybridisation gap, however there is not enough sophistication in the model nor data to ascertain whether these are topological states or simply topologically-trivial metallic states a the surface.

Bibliography

[1] James F. Annett. *Superconductivity, Superfluids and Condensates*. Oxford University Press, 1st edition, 2004.

[2] J. Bardeen, L. N. Cooper, and J. R. Schrieffer. Theory of superconductivity. *Physical Review*, 108(5):1175–1204, December 1957.

[3] D.R. Tilley and J. Tilley. *Superfluidity and Superconductivity*. Adam Hilger, Bristol and New York, 3rd edition, 1990.

[4] K. Ishida, H. Mukuda, Y. Kitaoka, K. Asayama, Z. Q. Mao, Y. Mori, and Y. Maeno. Sprin-triplet superconductivity in Sr_2RuO_4 identified by ^{17}O Knight shift. *Letters to Nature*, 396:658–660, December 1998.

[5] H. Tou, Y. Kitaoka, K Asayama, N. Kimura, Y. Ōnuki, E. Yamamoto, and K. Maezawa. ^{195}Pt Knight shift study of single crystal UPt_3 - evidence for odd-parity pairing. *Proceedings of the 21st International Conference on Low Temperature Physics, Prague*, S2:779–780, August 1996.

[6] A. P. Mackenzie and Y. Maeno. p-wave superconductivity. *Physica B*, (280):148–153, 2000.

[7] S. E. Barett, D. J. Durand, C. H. Pennington, C. P. Slichter, T. A. Friedmann, J. P. Rice, and D. M. Ginsberg. ^{63}Cu Knight shifts in the superconducting state of $YBa_2Cu_3O_{7-\delta}$ (T_c = 90 K). *Physical Review B*, 41(10):6283–6296, April 1990.

[8] M. Takigawa, P. C. Hammel, R. H. Heffner, and Z. Fisk. Spin susceptibility in superconducting $YBa_2Cu_3O_7$. *Physical Review B*, 39(10):7371–7374, April 1989.

[9] I. Iguchi and Z. Wen. Experimental evidence for a d-wave pairing state in $YBa_2Cu_3O_{7-y}$ from a study of $YBa_2Cu_3O_{7-y}$/insulator/Pb Jospehson tunnel junctions. *Physical Review B*, 49(17):12388–12391, May 1994.

[10] A. C. Hewson. *The Kondo Problem to Heavy Fermions*. Cambridge Studies in Magnetism. Cambridge University Press, 1st edition, 1993.

[11] J. Kondo. Theory of dilute magnetic alloys. *Solid State Physics*, 23:183–281, 1970.

[12] Stephen Blundell. *Magnetism in Condensed Matter*. Oxford University Press, 1st edition, 2001.

[13] G. R. Stewart. Heavy-fermion systems. *Reviews Of Modern Physics*, 56(4):755–787, October 1984.

[14] S. Doniach. The kondo lattice and weak antiferromagnetism. *Physica B*, 91:231–234, 1977.

[15] S. Doniach. Phase diagram for the Kondo lattice. *Valence Instabilities and Related Narrow-Band Phenomena, Springer*, pages 169–176, 1977.

[16] Tadao Kasuya. A theory of metallic ferro- and antiferromagnetism on Zener's model. *Progress of Theoretical Physics*, 16(1):45–57, July 1956.

[17] P. Coleman. Heavy fermions: electrons at the edge of magnetism. *https://arxiv.org/abs/cond-mat/0612006v3*, 3, January 2007.

[18] P.M. Chaikin and T.C. Lubensky. *Principles of Condensed Matter Physics*. Cambridge University Press, 5th edition, 2010.

[19] S. Hemmatiyan, M. Rahimi Movassagh, N. Ghassemi, M. Kargarian, A. T. Rezakhani, and A. Langari. Quantum phase transitions in the kondo-necklace model: perturbative continuous unitary transformation approach. *Journal of Physics: Condensed Matter*, 27(155601), March 2015.

[20] F. Steglich, U. Rauchschwalbe, U. Gottwick, H. M. Mayer, G. Sparn, and N. Grewe. Heavy fermions in Kondo lattice compounds (invited). *Journal of Applied Physics*, 57(1):3054–3059, April 1985.

[21] Mostafa Enayat, Zhixiang Sun, Ana Maldonado, Hermann Suderow, Silvia Seiro, Christoph Geibel, Steffen Wirth, Frank Steglich, and Peter Wahl. Superconducting gap and vortex lattice of the heavy-fermion compound $CeCu_2Si_2$. *Physical Review B*, 93(045123), January 2016.

[22] S. Doniach and M. Šunjić. Many-electron singularity in X-ray photoemission and X-ray line spectra form metals. *Journal of Physics C: Solid State Physics*, 3:285–291, September 1970.

[23] Robert Joynt and Louis Taillefer. The superconducting phases of UPt_3. *Reviews Of Modern Physics*, 74:235–294, January 2002.

[24] A. Menth, E. Buehler, and T. H. Geballe. Magnetic and semiconducting properties of SmB_6. *Physical Review Letters*, 22(7):295–297, February 1969.

[25] U. Fano. Effects of configuration interaction on intensities and phase shifts. *Physical Review*, 124(6):1866–1878, December 1961.

[26] Y. Dubi P. Wölfle and A. V. Balatsky. Tunneling into clean heavy fermion compounds: Origin of the Fano lineshape. *Physical Review Letters*, 105(246401), 2013.

[27] A. R. P. Rau. Perspectives on the fano resonance formula. *Physica Scripta*, 69(C10-13), 2004.

[28] O. Újsághy, J. Kroha, L. Szunyogh, and A. Zawadowski. Theory of the Fano resonance in the STM tunneling density of states due to a single Kondo Impurity. *Physical Review Letters*, 85(12):2557–2560, September 2000.

[29] Markus Ternes. Spectroscopic manifestations of the Kondo effect on single adatoms. *Journal of Physics: Condensed Matter*, 21(053001), 2009.

[30] M. Plihal and J. W. Gadzuk. Nonequilibrium theory of scanning tunneling spectroscopy via adsorbate resonances: Nonmagnetic and Kondo impurities. *Physical Review B*, 63(085404), February 2001.

[31] Gerd Binnig and Heinrich Rohrer. Scanning tunneling microscopy - from birth to adolescence. *Reviews Of Modern Physics*, 59(3):615–625, July 1987.

[32] A. C. Phillips. *Introduction to Quantum Mechanics*. Wiley, 1st edition, 2003.

[33] U.R. Singh S.C. White and P. Wahl. A stiff scanning tunneling microscopy head for measurements at low temperatures and high magnetic fields. *Review of Scientific Instruments*, 82(113708), 2011.

[34] J. Bardeen. Tunnelling from a many-particle point of view. *Physical Review Letters*, 6(2), 1961.

[35] J. Tersoff and D. R. Hamann. Theory of the scanning tunneling microscope. *Physical Review B*, 31(2), 1985.

[36] C. Julian Chen. *Introduction to Scanning Tunneling Microscopy*. OUP Oxford, second edition, 2007.

[37] Mostafa Enayat. Construction and operation of a milli-kelvin spectroscopic imaging STM for the study of correlated electron materials, PhD thesis. *École Polytechnique Fédérale de Lausanne, Switzerland*, May 2014.

[38] R. C. Dynes, V. Narayanamurti, and J. P. Garno. Direct measurement of quasiparticle-lifetime broadening in a strong-coupled superconductor. *Physical Review Letters*, 41(21):1509–1512, November 1978.

[39] J. R. Hahn and W. Ho. Single molecule imaging and vibrational spectroscopy with a chemically modified tip of a scanning tunneling microscope. *Physical Review Letters*, 87(19), October 2001.

[40] P. Wahl, L. Diekhöner, M. A. Schneider, and K. Kem. Background removal in scanning tunnelling spectroscopy of single atoms and molecules on metal surfaces. *Review of Scientific Instruments*, 79(043104), 2008.

[41] Shun Chi, Ramakrishna Aluru, Stephanie Grothe, A. Kreisel, Udai Raj Singh, Brian M. Andersen, W. N. Hardy, Ruixing Liang, D. A. Bonn, S. A. Burke, and Peter Wahl. Imaging the real space structure of the spin fluctuations in an iron-based superconductor. *Nature Communications*, (15996), 2017.

[42] Mark A. Reed. Inelastic electron tunneling spectroscopy. *Materials Today*, 11(11):46–50, November 2008.

[43] Jenny Hoffman. *A Search for Alternative Electronic Order in the High Temperature Superconductor $Bi_2Sr_2CaCu_2O_{8+\delta}$ by Scanning Tunneling Microscopy.* PhD thesis, University of California, Berkeley, Fall 2003.

[44] J.E. Hoffman, K. McElroy, D. H. Lee, K. M Lang, H. Eisaki, S. Uchida, and J. C. Davis. Imaging quasiparticle interference in $Bi_2Sr_2CaCu_2O_{8+\delta}$. *Science*, 297:1148 – 1151, 2002.

[45] K. McElroy, R. W. Simmonds, J. E. Hoffman, D. H. Lee, J. Orenstein, H. Elsaki, S. Uchida, and J. C. Davis. Relating atomic-scale electronic phenomena to wave-like quasiparticle states in superconducting $Bi_2Sr_2CaCu_2O_{8+\delta}$. *Nature*, 422:592–596, April 2003.

[46] K. McElroy, G. H. Gweon, S. Y. Zhou, J. Graf, S. Uchida, H. Eisaki, H. Takagi, T. Sasagawa, D. H. Lee, and A. Lanzara. Elastic scattering susceptibility of the high temperature superconductor $Bi_2Sr_2CaCu_2O_{8+\delta}$: A comparison between the real and momentum space photoemission spectroscopies. *Physical Review Letters*, 96(067005), February 2006.

[47] R. S. Markiewicz. Bridging k and q space in the cuprates: Comparing angle-resolved photoemission and STM results. *Physical Review B*, 69(214517), June 2004.

[48] U. Chatterjee, M. Shi, A. Kaminski, A. Kanigel, H. M. Fretwell, K. Terashima, T. Takahashi, S. Rosenkranz, Z. Z. Li, H. Raffy, A. Santander-Syro, K. Kadowaki, M. R. Norman, M. Randeria, and J. C. Campuzano. Nondispersive Fermi Arcs and the absence of charge ordering in the pseudogap phase of $Bi_2Sr_2CaCu_2O_{8+\delta}$. *Physical Review Letters*, 96(107006), March 2006.

[49] Qiang-Hua Wang and Dung-Hai Lee. Quasiparticle scattering interference in high-temperature superconductors. *Physical Review B*, 67(020511), January 2003.

[50] C. Bucci P. Gorla and S. Pirro. Complete elimination of 1k pot vibrations in dilution refrigerators. *Nuclear Instruments and Methods in Physics Research A*, 520:641–643, 2004.

[51] S. Pirro, A. Alessandrello, C. Brofferio, C. Bucci, O. Cremonesi, E. Coccia, E. Fiorini, V. Fafone, A. Giuliani, A. Nucciotti, M. Pavan, G. Pessina, E. Previtali, M. Vanzini, and L. Zanotti. Vibrational and thermal noise-reduction for cryogenic detectors. *Nuclear Instruments and Methods in Physics Research A*, 444:331–335, 2000.

[52] Michael Möser. *Engineering Acoustics: An Introduction to Noise Control*. Springer, second edition, 2009.

[53] Benjamin MacLeod. An ultra-low-vibration facility for housing a dilution tmperature scanning tunneling microscope. *Master of Applied Science Thesis*, August 2015.

[54] B. P. MacLeod, J. E. Hoffman, S. A. Burke, and D. A. Bonn. Acoustic buffeting by infrasound in a low vibration facility. *Review of Scientific Instruments*, 87(093901), 2016.

[55] Bert Voigtländer, Peter Coenen, Vasily Cherepanov, Peter Borgens, Thomas Duden, and F. Stefan Tautz. Low vibration laboratory with a single-stage vibration isolation for microscopy applications. *Review of Scientific Instruments*, 88(023703), 2017.

[56] Frank Pobell. *Matter and Methods at Low Temperatures*. Springer, third edition edition, 2007.

[57] Nathaniel Craig and Ted Lester. *Hitchhiker's Guide to the Dilution Refrigerator*, volume Version 2.00. Marcus Lab, Harvard University, August 2004.

[58] U. R. Singh, M. Enayat, S. C. White, and P. Wahl. Construction and performance of a dilution-refrigerator based spectroscopic-imaging scanning tunnelling microscope. *Review of Scientific Instruments*, 84(013708), 2013.

[59] A. M. J. den Haan, G. H. C. J. Wijts, F. Galli, O. Usenko, G. J. C. van Baarle, D. J. van der Zalm, and T. H. Oosterkamp. Atomic resolution scanning tunneling microscopy in a cryogen free dilution refrigerator at 15 mK. *Review of Scientific Instruments*, 85(035112), 2014.

[60] Jason D. Hackley, Dmitry A. Kislitsyn, Daniel K. Beaman, Stefan Ulrich, and George V. Nazin. High-stability cryogenic scanning tunneling microscope based on a closed-cycle cryostat. *Review of Scientific Instruments*, 85(103704), 2014.

[61] M. H. Van Maaren. On the superconductivity, carrier concentration and the ionic model of Sn_4P_3 and Sn_4As_3. *Physics Letters*, 29A(6):293–294, June 1969.

[62] Percy Zahl, Thorsten Wagner, Rolf Möller, and Andreas Klust. Open source scanning probe microscopy control software package GXSM. *Journal of Vacuum Science and Technology B, Nanotechnology and Microelectronics: Materials, Processing, Measurement, and Phenomena*, 28(C4E39), May 2010.

[63] E. R. Schemm, W. J. Gannon, C. M. Wishne, W. P. Halperin, and A. Kapitulnik. Observation of broken time-reversal symmetry in the heavy-fermion superconductor UPt_3. *Science*, 345(6193):190–193, July 2014.

[64] Andrew Huxley, Donald M^{c}K. Paul Pierre Rodière, Niels van Dijk, Robert Cubitt, and Jacques Flouquet. Realignment of the flux-line lattice by a change in the symmetry of superconductivity in UPt_3. *Nature*, 406:160–164, 2000.

[65] J. P. Brison, N. Keller, P. Lejay, J. L. Tholence, A. Huxley, N. Bernhoeft, A. I. Buzdin, B. Fåk, J. Flouquet, L. Schmidt, A. Stepanov, R. A. Fisher, N. Phillips, and C. Vettier. Magnetism and superconductivity in heavy fermion systems. *Journal of Low Temperature Physics*, 95:145–152, 1994.

[66] H. Suderow, J. P. Brison, A. Huxley, and J. Flouquet. Thermal conductivity and gap structure of the superconducting phases of UPt_3. *Journal of Low Temperature Physics*, 108(1/2):11–30, 1997.

[67] H. Suderow, J. P. Brison, A. Huxley, and J. Flouquet. Scaling and thermal conductivity in unconventional superconductors: The case of UPt_3. *Physical Review Letters*, 80(1):165–168, January 1998.

[68] Qi Li, John Toner, and D. Belitz. Skyrmion versus vortex flux lattices in p-wave superconductors. *Physical Review B*, 79(014517), January 2009.

[69] Yasumasa Tsutsumi, Kazushige Machida, Tetsuo Ohmi, and Masa aki Ozaki. A spin triplet superconductor UPt_3. *Journal of the Physical Society of Japan*, 81(074717), 2012.

[70] D. A. Ivanov. Non-abelian statistics of half-quantum vortices in p-wave superconductors. *Physical Review Letters*, 86(2):268–271, January 2001.

[71] A. Yu. Kitaev. Unpaired majorana fermoins in quantum wires. *Physics-Uspekhi*, 44(171):131–146, 2001.

[72] M. H. Devoret and R. J. Schoelkopf. Superconducting circuits for quantum informaiton: An outlook. *Science*, 339:1169–1174, March 2013.

[73] C. W. J. Beenakker. Search for majorana fermions in superconductors. *Annual Review of Condensed Matter Physics*, 4:113–136, 2013.

[74] Yasumasa Tsutsumi, Masaki Ishikawa, Takuto Kawakami, Takeshi Mizushima, Masatoshi Sato, Masanori Ichioka, and Kazushige Machida. UPt_3 as a topological

crystalline superconductor. *Journal of the Physical Society of Japan*, 82(113707), October 2013.

[75] Youichi Yanase and Ken Shiozaki. Möbius topological superconductivity in UPt_3. *Physical Review B*, 95(224514), June 2017.

[76] M. H. S. Amin and A. Yu. Smirnov. Quasiparticle decoherence in d-wave superconducting qubits. *Physical Review Letters*, 92(1), January 2004.

[77] Thilo Bauch, Tobias Lindström, Francesco Tafuri, Giacomo Rotoli, Per Delsing, Tord Claeson, and Floriana Lombardi. Quantum dynamics of a d-wave josephson junction. *Science*, 311:57–60, 2006.

[78] S. M. Hayden et al. Antiferromagnetic order in upt_3 under pressure: Evidence for a direct coupling to superconductivity. *Physical Review B*, 46(13):8675–8678, October 1992.

[79] B. Lussier, L. Taillefer, W. J. L. Buyers, T. E. Mason, and T. Petersen. Influence of a magnetic field on the antiferromagnetic order in UPt_3. *Physical Review B*, 54(10):R6873 – R6876, September 1996.

[80] N. H. van Dijk, P. Rodière, B. Fåk, A. Huxley, and J. Flouquet. Weak antiferromagnetic order and superconductivity in UPt_3 studied by neutron scattering. *Physica B*, 319:220–232, February 2002.

[81] N. H. van Dijk, B. Fåk, L. P. Regnault, and A. Huxley. Magnetic order of UPt_3 in high magnetic fields. *Physical Review B*, 58(6):3186–3190, August 1998.

[82] Juana Moreno and J. A. Sauls. Magnetic field effects on neutron diffraction in the antiferromagnetic phase of UPt_3. *Physical Review B*, 63(024419), December 2000.

[83] C. Lacroix, B. Canals, and M. D. Núñez-Regueiro. Kondo screening and magnetic ordering in frustrated UNi_4B. *Physical Review Letters*, 77(25):5126–5129, December 1996.

[84] Andreas Amann and Ana Celia Mota. Magnetic properties of UPt_3 in the superconducting state. *Physical Review B*, 57(6):3640–3649, February 1998.

[85] P. A. Midgley, S. M. Hayden, L. Taillefer, B. Bogenberger, and H. V. Löhneysen. Superconductivity and the incommensurate structural modulation in the heavy fermion UPt_3. *Physical Review Letters*, 70(5):678–681, February 1993.

[86] P. H. Frings, J. J. M Franse, F. R. de Boer, and A. Menovsky. Magnetic properties of U_xPt_y compounds. *Journal of Magnetism and Magnetic Materials*, 31-34:240–242, 1983.

[87] G. R. Stewart, Z. Fisk, J. O. Willis, and J. L. Smith. Possibility of coexistence of bulk superconductivity and spin fluctuations in UPt_3. *Physical Review Letters*, 52(8):679–682, February 1984.

[88] L. Taillefer and G. G. Lonzarich. Heavy-fermion quasiparticles in UPt_3. *Physical Review Letters*, 60(15):1570–1573, April 1988.

[89] G J McMullan, P M C Rourke, M R Norman, A D Huxley, N Doiron-Leyraud, J Flouquet, G G Lonzarich, A McCollam, and S R Julian. The fermi surface and f-valence electron count of UPt_3. *New Journal of Physics*, 10(053029), May 2008.

[90] M. P. Allan, F. Massee, D. K. Morr, J. Van Dyke, A. W. Rost, A. P. Mackenzie, C. Petrovic, and J. C. Davis. Imaging cooper pairing of heavy fermions in $CeCoIn_5$. *Nature Physics Letters*, 9:468–473, August 2013.

[91] A. Maldonado, I Giullamon, J. G. Rodrigo, H. Suderow, S. Vieira, D. Aoki, and J. Flouquet. Tunneling spectroscopy of the superconducting state of URu_2Si_2. *Physical Review B*, 85(214512), June 2012.

[92] Edwin Herrera Vasco. Visualizing the influence of the Fermi surface on Superconductivity. *PhD Thesis, Universidad Autónama de Madrid*, November 2016.

[93] V. Ambegaokar, P. G. de Gennes, and D. Rainer. Landau-Ginsburg equations for an anisotropic superfluid. *Physical Review A*, 9(6):2676–2685, June 1974.

[94] D. Rainer, H. Burkhardt, M. Fogelström, and J. A. Sauls. Andreev bound states, surfaces and subdominant pairting in high t_c superconductors. *Journal of Physical Chemistry of Solids*, 59(2040), 1998.

[95] L. J. Buchholtz and G. Zwicknagl. Identification of p-wave superconductors. *Physical Review B*, 23(11):5788–5796, June 1981.

[96] A. R. Schmidt, M. H. Hamidian, P. Wahl, F. Meier, A. V. Balatsky, J. D. Garrett, T. J. Williams, G. M. Luke, and J. C. Davis. Imaging the fano lattice to 'hidden order' transition in URu_2Si_2. *Nature*, 465:570–576, June 2010.

[97] Pegor Aynajian, Eduardo H. da Silva Neto, Colin V. Parker, Yingkai Huang, Abhay Pasupathy, John Mydosh, and Ali Yazdani. Visualizing the formation of the Kondo lattice and the hidden order in URu_2Si_2. *PNAS*, 107(23):10383–10388, June 2010.

[98] T. Ito, H. Kumigashira, Hyeong-Do Kim, and T. Takahashi. High-resolution angle-resolved photoemission study of the heavy-fermion superconductor UPt_3. *Physical Review B*, 59(13):8923–8929, April 1999.

[99] A. J. Arko, J. J. Joyce, A. B. Andrews, J. D. Thompson, J. L. Smith, D. Mandrus, M. F. Hundley, A. L. Cornelius, E. Moshopoulou, Z. Fisk, P. C. Canfield, and Alois Menovsky. Strongly correlated electron systems: Photoemission and the single-impurity model. *Physical Review B*, 56(12):R7041–R7044, September 1997.

[100] G. Aeppli, E. Bucher, and G. Shirane. Direct observation of spin fluctuations in the heavy-fermion system UPt_3. *Physical Review B*, 32(11):7579–7582, December 1985.

[101] H. Brenten, E. Zirngiebl, M. S. Wire, S. Blumenröder, G. Pofahl, G. Güntherodt, and Z. Fisk. Raman scattering from spin fluctuations and phonons in the heavy-fermion superconductor UPt_3. *Solid State Communications*, 62(6):387–390, January 1987.

[102] J. R. Kirtley and D. J. Scalapino. Inelastic-tunneling model for the linear conductance background in the high-T_c superconductors. *Physical Review Letters*, 65(6):798–800, August 1990.

[103] Patrik Hlobil, Jasmin, Jandke, Wulf Wulfhekel, and Jörg Schmalian. Tracing the electronics pairing glue in unconventional superconductors via inelastic scanning tunneling spectroscopy. *Physical Review Letters*, 118(167001), April 2017.

[104] S. L. Cooper, M. V. Klein, Z. Fisk, and J. L. Smith. Polarized light study of UPt_3. *Physical Review B*, 37(4):2251–2253, February 1988.

[105] P. Wachter F. Marabelli and J. J. M. Franse. Electronic structure of UPt_3: A low energy optical study. *Journal of Magnetism and Magnetic Materials*, 62:287–292, 1986.

[106] P. Wachter F. Marabelli, G. Travaglini. Electronic structure of UPt_3 in the vicinity of the fermi energy. *Solid State Communications*, 59(6):381–384, January 1986.

[107] M. Yoshizawa, B. Lüthi, T. Goto, T. Suzuki, B. Renker, A. de Visser, P. Frings, and J. J. M. Franse. Electron-phonon coupling in uranium compounds. *Journal of Magnetism and Magnetic Materials*, 52:413–417, 1985.

[108] S. Raymond, J. Bouchet, G. H. Lander, M. Le Tacon, G. Garbarino, M. Hoesch, J.-P. Rueff, M. Krisch, J. C. Lashley, R. K. Schulze, and R. C. Albers. Understanding the complex phase diagram of uranium: The role of electron-phonon coupling. *Physical Review Letters*, 107(136401), September 2011.

[109] W. P. Crummett, H. G. Smith, R. M. Nicklow, and N. Wakabayashi. Lattice dynamics of α-uranium. *Physical Review B*, 19(12):6028–6037, June 1979.

[110] T. R. Ravindran and A. K. Arora. Study of Raman spectrum of uranium using a surface-enhanced Raman scattering technique. *Journal of Raman Spectroscopy*, 42:885–887, April 2011.

[111] Zhenyu Wang, Daniel Walkup, Phillip Derry, Thomas Scaffidi, Melinda Rak, Sean Vig, Anshul Kogar, Ilija Zeljkovic, Ali Husain, Luiz H. Santos, Yuxuan Wang, Andrea Damascelli, Yoshiteru Maeno, Peter Abbamonte, Eduardo Fradkin, and Vidya Madhavan. Quasiparticle interference and strong electron-mode coupling in the quasi-one-dimensional bands of Sr_2RuO_4. *Nature Physics*, 4107, May 2017.

[112] W. L. McMillan. Transition temperature of strong-coupled superconductors. *Physical Review*, 167(2):331–344, August 1968.

[113] J. J. M. Franse A. de Visser and A. Menovsky. Resistivity of single-crystalline UPt_3 and its pressure dependence; interpretation by a spin-fluctuation model. *Journal of Magnetism and Magnetic Materials*, 43:43–47, January 1984.

[114] N. Grewe. One particle excitation spectrum of the kondo-lattice. *Solid State Communications*, 50(1):19–23, January 1984.

[115] B. H. Brandow. Variational theory of valence fluctuations: Ground states and quasiparticle excitations of the anderson lattice model. *Physical Review B*, 33(1):215–238, January 1986.

[116] John Singleton. *Band Theory and Electronic Properties of Solids*. Oxford University Press, 2001.

[117] N. KImura, R. Settai, Y. Ōnuki, E. Yamamoto, K. Maezawa, H. Aoki, and H. Harima. Fermi surface property of UPt_3 studied by magnetoresistance and dHvA effect. *Physica B*, 223 and 224:181–184, 1996.

[118] Sajedeh Manzeli, Dmitry Ovchinnikov, Diego Pasquier, Oleg V. Yazyev, and Andras Kis. 2D transition metal dichalcogenides. *Nature Reviews: Materials*, 2(17033), June 2017.

[119] J. A. Wilson and A. D. Yoffe. The transition metal dichalcogenides: Discussion and interpretation of the observed optical, electrical and structural properties. *Advances in Physics*, 18(73):193–335, 1969.

[120] D. Biswas, Alex. M Ganose, R. Yano, J. M. Riley, L. Bawden, O. J. Clark, J. Feng, L. Collins-Mcintyre, M. T. Sajjad, W. Meevasana, T. K. Kim, M. Hoesch, J. E. Rault, T. Sasagawa, David O. Scanlon, and P. D. C King. Narrow-band anisotropic electronic structure of ReS_2. *Physical Review B*, 96(085205), August 2017.

[121] Yi Ding, Yanli Wang, Jun Ni, Lin Shi, Siqi Shi, and Weihua Tang. First principles study of structural vibrational and electronic properties of graphene-like MX_2 (M = Mo, Nb, W, Ta; X = S, Se, Te) monolayers. *Physica B*, 406:2254–2260, March 2011.

[122] A. R. Beal, H. P. Hughes, and W. Y. Liang. The reflectivity spectra of some group VA transition metal dichalcogenides. *Journal of Physics C: Solid State Physics*, 8(4236), September 1975.

[123] Qing Hua Wang, Kourosh Kalantar-Zadeh, Andras Kis, Jonathan N. Coleman, and Michael S. Strano. Electronics and optoelectronics of two-dimensional transition metal dichalcogenides. *Nature Nanotechnology*, 7:699–712, November 2012.

[124] Kari Selte Sigrid Furuseth and Arne Kjekshus. Redetermined crystal structures of $NiTe_2$, $PdTe_2$, PtS_2, $PtSe_2$, and $PtTe_2$. *Acta Chemica Scandinavia*, 19(1):257–258, 1965.

[125] Han-Jin Noh, Jinwon Jeong, En-Jin Cho, Kyoo Kim, and Byeong-Gyu Park. Experimental realization of type-ii dirac fermions in a $PdTe_2$ superconductor. *Physical Review Letters*, 119(016401), July 2017.

[126] Gihun Ryu. Superconductivity in Cu-Intercalated CdI_2-Type $PdTe_2$. *Journal of Superconductivity and Novel Magnetism*, 28(11):3275–3280, November 2015.

[127] Manish Chhowalla, Hyeon Suk Shin, Goki Eda, Lain-Jong Li, Kian Ping Loh, and Hua Zhang. The chemistry of two-dimensional layered transition metal dichalcogenide nanosheets. *Nature Chemistry*, 5:263–275, March 2013.

[128] Fucong Fei, Xiangyan Bo, Rui Wang, Bin Wu, Juan Jiang, Dongzhi Fu, Ming Gao, Hao Zheng, Yulin Chen, Xuefeng Wang, Haijun Bu, Fengqi Song, Xiangang

Wan, Baigeng Wang, and Guanghou Wang. Nontrivial Berry phase and type-II Dirac transport in the layered material $PdTe_2$. *Physical Review B*, 96(041201), July 2017.

[129] A. B. Karki, D. A. Browne, S. Stadler, J. Li, and R. Jin. PdTe: a strongly coupled superconductor. *Journal of Physics: Condensed Matter*, 24(055701), January 2012.

[130] M. S. Bahramy, O. J. Clark, B.-J. Yang, J. Feng, L. Bawden, J. M. Riley, I. Marković, F. Mazzola, V. Sunko, D. Biswas, S. P. Cooil, M. Jorge, J. W. Wells, M. Leandersson, T. Balasubramanian, J. Fujii, I. Vobornik, J. Rault, T. K. Kim, M. Hoesch, K. Okawa, M. Asakawa, T. Sasagawa, T. Eknapakul, W. Meevasana, and P. D. C King. Ubiquitous formation of type-II bulk Dirac cones and topological surface states from a single orbital manifold in transition-metal dichalcogenides. *Nature Materials*, 17(21), 2018.

[131] Mingzhe Yan, Huaqing Huang, Kenan Zhang, Eryin Wang, Wei Yao, Ke Deng, Guoliang Wan, Hongyun Zhang, Masashi Arita, Haitao Yang, Zhe Sun, Hong Yao, Yang Wu, Soushan Fan, Wenhui Duan, and Shuyun Zhou. Lorentz-violating type-II Dirac fermions in transition metal dichalcogenide $PtTe_2$. *Nature Communications*, 8(257), August 2017.

[132] Huaqing Huang, Shuyun Zhou, and Wenhui Duan. Type-II Dirac fermions in the $PtSe_2$ class of transition metal dichalcogenides. *Physical Review B*, 94(121117), September 2016.

[133] O. J. Clark, M. J. Neat, K. Okawa, L. Bawden, I. Marković, F. Mazzola, J. Feng, V. Sunko, J. M. Riley, J. Fujii, I. Vobornik, T. K. Kim, M. Hoesch, W. Meevasana, T. Sasagawa, P. Wahl, M. S. Bahramy, and P. D. C King. Fermiology and superconductivity of topological surface states in $PdTe_2$. *Physical Review Letters*, February 2018.

[134] Masatoshi Sato and Yoichi Ando. Topological superconductors: a review. *Reports on Progress in Physics*, 80(076501), May 2017.

[135] Zhixiang Sun, Mostafa Enayat, Ana Maldonado, Calum Lithgow, Ed Yelland, Darren C. Peets, Alexander Yaresko, Andreas P. Schnyder, and Peter Wahl. Dirac surface states and nature of superconductivity in Noncentrosymmetric bipd. *Nature Communications*, 6(7633), March 2015.

[136] Luis Maier, Jeroen B. Oostinga, Daniel Knott, Christoph Brüne, Pauli Virtanen, Grigory Tkachov, Ewelina M. Hankiewicz, Charles Gould, Hartmut Buhmann, and Laurens W. Molenkamp. Induced superconductivity in the three-dimensional topological insulator HgTe. *Physical Review Letters*, 109(186806), November 2012.

[137] R. S. Deacon, J. Wiedenmann, E. Bocquillon, F. Domínguez, T. M. Klapwijk, P. Leubner, C. Brüne, E. M. Hankiewicz, S. Tarucha, K. Ishibashi, H. Buhmann, and L. W. Molenkamp. Josephson radiation from gapless Andreev bound states in HgTe-based topological junctions. *Physical Review X*, 7(021011), April 2017.

[138] Fan Yang, Fanming Qu, Jie Shen, Yue Ding, Jun Chen, Zhongqing Ji, Guangtong Liu, Jie Fan, Changli Yang, Liang Fu, and Li Lu. Proximity-effect-induced superconducting phase in the topological insulator Bi_2Se_3. *Physical Review B*, 86(134504), October 2012.

[139] Parisa Zareapour, Alex Hayat, Shu Yang F. Zhao, Michael Kreshchuk, Achint Jain, Daniel C. Kwok, Nara Lee, Sang-Wook Cheong, Zhijun Xu, Alina Yang, G. D. Gu, Shuang Jia, Robert J. Cava, and Kenneth S. Burch. Proximity-induced high-temperature superconductivity in the topological insulators Bi_2Se_3 and Bi_2Te_3. *Nature Communications*, 3(2042), September 2012.

[140] Eryin Wang, Hao Ding, Alexei F. Federov, Wei Yao, Zhi Li, Yan-Feng Lv, Kun Zhao, Li-Guo Zhang, Zhijun Xu, John Schneeloch, Ruidan Zhong, Shuai-Hua Ji, Lili Wang, Ke He, Xucun Ma, Genda Gu, Hong Yao, Qi-Kun Xue, Xi Chen, and Shuyun Zhou. Fully gapped topological surface states in Bi_2Se_3 films induced by a d-wave high-temperature superconductor. *Nature Physics*, 9(2744):621–625, September 2013.

[141] H. Leng, C. Paulsen, Y. K. Huang, and A. de Visser. Type I superconductivity in the Dirac semimetal $PdTe_2$. *arXiv:1710.03862 [cond-mat.supr-con]*, October 2017.

[142] Noriaki Kimura, Noriyuki Kabeya, Koshuke Saitoh, Kazunori Satoh, Hajime Ogi, Kohki Ohsaki, and Haruyoshi Aoki. Type II/I superconductivity with extremely high H_{c3} in noncentrosymmetric $LaRhSi_3$. *Journal of the Physical Society of Japan*, 85(024715), January 2016.

[143] Drew Jared Rebar. Exploring superconductivity in chiral structured AuBe. *PhD Thesis, Louisiana State University*, December 2015.

[144] Zhongheng Liu, Xiong Yao, Jifeng Shao, Ming Zuo, Li Pi, Shun Tan, and Changjin Zhang. Superconductivity with topological surface state in $Sr_xBi_2Se_3$. *Journal of the American Chemical Society*, 137:10512–10515, 2015.

[145] Shruti, V. K. Maurya, P. Neha, P. Srivastava, and S. Patnaik. Superconductivity by Sr intercalation in the layered topological insulator Bi_2Se_3. *Physical Review B*, 92(020506), July 2015.

[146] Guan Du, Jifeng Shao, Xiong Yang, Zengyi Du, Delong Fang, Jinghui Wang, Kejing Ran, Jinsheng Wen, Changjin Zhang, Huan Yang, Yuheng Zhang, and Hai-Hu Wen. Drive the Dirac electrons into Cooper pairs in $Sr_xBi_2Se_3$. *Nature Communications*, 8(14466), February 2017.

[147] S. H. Pan, E. W. Hudson, A. K. Gupta, K. W. Ng, H. Eisaki, S. Uchida, and J. C. Davis. Stm studies of the electronic structure of vortex cores in $Bi_2Sr_2CaCu_2O_{8+\delta}$. *Physical Review Letters*, 85(7):1536–1539, August 2000.

[148] Zengyi Du, Delong Fang, Zhenyu Wang, Yufeng Li, Guan Du, Huan Yang, Xiyu Zhu, and Hai-Hu Wen. Anisotropic superconducting gap and elongated vortices with Caroli-De Gennes-Matricon states in the new superconductor $Ta_4Pd_3Te_{16}$. *Nature Scientific Reports*, 5(9408), March 2015.

[149] T. Ritschel, J. Trinckauf, K. Koepernik, B. Büchner, M. v. Zimmermann, H. Berger, Y. I. Joe, P. Abbamonte, and J. Geck. Orbital textures and charge density waves in transition metal dichalcogenides. *Nature Physics*, 11(3267):328–331, March 2015.

[150] J. A. Wilson, F. J. Di Salvo, and S. Mahajan. Charge-density waves in metallic, layered, transition-metal dichalcogenides. *Physical Review Letters*, 32(16):882–885, April 1974.

[151] C. Berthier, D. Jerome, and P. Molinie. NMR study on a 2H-$NbSe_2$ single crystal: A microscopic investigation of the charge density waves state. *Journal of Physics C: Solid State Physics*, 11(797), July 1978.

[152] K. Ghoshray, B. Pahari, A. Ghoshray, V. V. Eremenko, V. A. Sirenko, and B. H. Suits. ^{93}Nb NMR study of the charge density wave state in $NbSe_2$. *Journal of Physics: Condensed Matter*, 21(155701), March 2009.

[153] C. J. Arguello, S. P. Chockalingam, E. P. Rosenthal, L. Zhao, C. Gutiérrez, J. H. Kang, W. C. Chung, R. M. Fernandes, S. Jia, A. J. Millis, R. J. Cava, and A. N. Pasupathy. Visualising the charge density wave transition in 2H-$NbSe_2$ in real space. *Physical Review B*, 89(235115), June 2014.

[154] U. Chatterjee, J. Zhao, M. Iavarone, R. Di Capua, J. P. Castellan, G. Karapetrov, C. D. Malliakas, M. G. Kanatzidis, H. Claus, J. P. C. Ruf, F. Weber, J. van Wezel, J. C. Campuzano, R. Osborn, M. Randeria, N. Trivedi, M. R. Norman, and S. Rosenkranz. Emergence of coherence in the charge-density wave state of 2H-$NbSe_2$. *Nature Communications*, 6(7313), February 2015.

[155] Tao Wu, Hadrien Mayaffre, Steffen Krämer, Mladen Hortavić, Claude Berthier, W. N. Hardy, Ruixing Liang, D. A. Bonn, and Marc-Henri Julien. Incipient charge order observed by NMR in the normal state of $YBa_2Cu_3O_y$. *Nature Communications*, 6(7438), March 2015.

[156] Johnpierre Paglione and Richard L. Greene. High-temperature superconductivity in iron-based materials. *Nature Physics*, 6:645–658, August 2010.

[157] G Haegg and A. L Kindstroem. Roentgenuntersuchungen am system eisen - selen. *Kirstallstruktur fuer Physikalische Chemie, Abteilung B: Chemie der Elementarprozesse, Aufbau der Materie*, 22:453–464, 1933.

[158] Fong-Chi Hsu, Jiu-Yong Luo, Kuo-Wei Yeh, Ta-Kun Chen, Tzu-Wen Huang, Phillip M. Wu, Yong-Chi Lee, Yi-Lin Huang, Yan-Yi Chu, Der-Chung Yan, and Maw-Kuen Wu. Superconductivity in the PbO-type structure α-FeSe. *PNAS*, 105(38):14262–14264, September 2008.

[159] J. P. Sun, K. Maysuura, G. Z. Ye, Y. Mizukami, M. Shimozawa, K. Matsubayashi, M. Yamashita, T. Watashige, S. Kasahara, Y. Matsuda, J. Q. Yan, B. C. Sales, Y. Uwatoko, J. G. Cheng, and T. Shibauchi. Dome-shaped magnetic order competing with high-temperature superconductivity at high pressures in FeSe. *Nature Communications*, 7(12146), July 2016.

[160] Yoshikazu Mizuguchi, Fumiaki Tomioka, Shunsuke Tsuda, Takahide Yamaguchi, and Yoshihiko Takano. Superconductivity at 27 K in tetragonal FeSe under high pressure. *Applied Physical Letters*, 93(152505), October 2008.

[161] Wang Qing-Yan, Li Zhi, Zhang Wen-Hao, Zhang Zuo-Cheng, Zhang Jin-Song, Li Wei, Ding Hao, Ou Yun-Bo, Deng Peng, Chang Kai, Wen Jing, Song Can-Li, He Ke, Jia Jin-Feng, Ji Shuai-Hua, Wang Ya-Yu, Wang Li-Li, Chen Xi, Ma Xu-Cun, and Xue Qi-Kun. Interface-induced high-temperature superconductivity in single unit-cell FeSe films on $SrTiO_3$. *Chinese Physical Letters*, 29(3), February 2012.

[162] Jian-Feng Ge, Zhi-Long Liu, Canhua Liu, Chun-Lei Gao, Dong Qian, Qi-Kun Xue, Ying Liu, and Jin-Feng Jia. Superconductivity above 100 K in single-layer FeSe films on doped $SrTiO_3$. *Nature Materials*, (10.1038), November 2014.

[163] T. M. McQueen, A. J. Williams, P. W. Stephens, J. Tao, Y. Yhu, V. Ksenofontov, F. Casper, C. Felser, and R. J. Cava. Tetragonal-to-Orthorhombic struc-

tural phase transition at 90 K in the superconductor $Fe_{1.01}Se$. *Physical Review Letters*, 103(057002), July 2009.

[164] R. M. Fernandes, A. V. Chubukov, and J. Schmalian. What drives nematic order in iron-based superconductors? *Nature Physics*, 10(1038):97–104, January 2014.

[165] Eduardo Fradkin, Steven A. Kivelson, Michael J. Lawler, James P. Eisenstein, and Andrew P. Mackenzie. Nematic Fermi fluids in condensed matter physics. *Annual Review of Condensed Matter Physics*, 1:153–178, May 2010.

[166] Dennis Huang, Tatiana A. Webb, Can-Li Song, Cui-Zu Chang, Jagadeesh S. Moodera, Efthimios Kaxiras, and Jennifer E. Hoffman. Dumbbell defects in FeSe films: A scanning tunneling microscopy and first-principles investigation. *Nano Letters*, 16(7):4224–4229, July 2016.

[167] Can-Li Song, Yi-Lin Wang, Peng Cheng, Ye-Ping Jiang, Wei Li, Tong Zhang, Zhi Li, Ke He, Lili Wang, Jin-Feng Jia, Hsiang-Hsuan Hung, Congjun Wu, Xucun Ma, Xi Chen, and Qi-Kun Xue. Direct observation of nodes and twofold symmetry in FeSe superconductor. *Science*, 332(1410), 2011.

[168] Can-Li Song, Yi-Lin Wang, Ye-Ping Jiang, Zhi Li, Lili Wang, Ke He, Xi Chen, Xu-Cun Ma, and Qi-Kun Xue. Molecular-beam epitaxy and robust superconductivity of stoichiometric FeSe crystalline films on bilayer graphene. *Physical Review B*, 84(020503), July 2011.

[169] Can-Li Song, Yi-Lin Wang, Ye-Ping Jiang, Lili Wang, Ke He, Xi Chen, Jennifer E. Hoffman, Xu-Cun Ma, and Qi-Kun Xue. Suppression of superconductivity by twin boundaries in FeSe. *Physical Review Letters*, 109(137004), September 2012.

[170] T. Watashige, Y. Tsutsumi, T. Hanaguri, Y. Kohsaka, S. Kasahara, A. Furusaki, M. Sigrist, C. Meingast, T. Wolf, H. V. Löhneysen, T. Shibauchi, and Y. Matsuda. Evidence for time-reversal symmetry breaking of the superconducting state near twin-boundary interfaces in FeSe revealed by scanning tuennling spectroscopy. *Physical Review X*, 5(031022), August 2015.

[171] Qisi Wang, Yao Shen, Bingying Pan ad Yiqing Hao, Mingwei Ma, Fang Zhou, P. Steffens, K. Schmalzl, T. R. Forrest, M. Abdel-Hafiez, Xiaojia Chen, D. A. Chareev, A. N. Vasillev, P. Bourges, Y. Sidis, Huibo Cao, and Jun Zhao. Strong interplay between stripe spin fluctuations, nematicity and superconductivity in FeSe. *Nature Materials*, (4492), December 2015.

[172] Shigeru Kasahara, Tatsuya Watashige, Tetsuo Hanaguri, Yuhki Kohsaka, Takuya Yamashita, Yusuke Shimoyama, Yuta Mizukami, Ryota Endo, Hiroaki Ikeda, Kazushi Aoyama, Taichi Terashima, Shinya Uji, Thomas Wolf, Hilbert von Löhneysen, Takasada Shibauchi, and Yuji Matsuda. Field-induced superconducting phase of FeSe in the BCS-BEC cross-over. *PNAS*, 111(46):16309–16313, November 2014.

[173] S. Kasahara, T. Yamashita, A. Shi, R. Kobayashi, Y. Shimoyama, T. Watashige, K. Ishida, T. Terashima, T. Wolf, F. Hardy, C. Meingast, H. V. Löhneysen, A. Levchenko, T. Shibauchi, and Y. Matsuda. Giant superconducting fluctuations in the compensated semimetal FeSe at the bcs-bec crossover. *Nature Communications*, 7(12843), September 2016.

[174] P. Bourgeois-Hope, S. Chi, D. A. Bonn, R. Liang, W. N. Hardy, T. Wolf, C. Meingast, N. Doiron-Leyraud, and Louis Taillefer. Thermal conductivity of the iron-based superconductor FeSe: Nodeless gap with a strong two-band character. *Physical Review Letters*, 117(097003), August 2016.

[175] Lin Jiao, Chien-Lung Huang, Sahana Rößler, Cevriye Koz, Ulrich K. Rößler, Ulrich Schwarz, and Steffan Wirth. Superconducting gap structure of FeSe. *Nature Scientific Reports*, 7(44024), March 2017.

[176] P. O. Sprau, A. Kostin, A. Kreisel, A. E. Böhmer, V. Taufour, P. C. Canfield, S. Mukherjee, P. J. Hirschfeld, B. M. Andersen, and J. C. Séamus Davis. Discovery of orbital-selective Cooper pairing in FeSe. *Science*, 357:75–80, July 2017.

[177] M. H. Hamidian, S. D. Edkins, Sang Hyun Joo, A. Kostin, H. Eisaki, S. Uchida, M. J. Lawler, E. A. Kim, A. P. Mackenzie, K. Fujita, Jinho Lee, and J. C. Davis. Detection of a Cooper-pair density wave in $Bi_2Sr_2CaCu_2O_{8+x}$. *Nature*, 532(17411):343–347, April 2016.

[178] Liang Fu and C. L. Kane. Topological insulators with inversion symmetry. *Physical Review B*, 76(045302), July 2007.

[179] Liang Fu, C. L. Kane, and E. J. Mele. Topological insulators in three dimensions. *Physical Review Letters*, 98(106803), March 2007.

[180] Maxim Dzero, Jing Zia, Victor Galitski, and Piers Coleman. Topological Kondo Insulators. *Annual Review of Condensed Matter Physics*, 7:249–280, January 2016.

[181] J. F. DiTusa, K. Friemelt, E. Bucher, G. Aeppli, and A. P. Ramirez. Metal-insulator transitions in the Kondo insulator FeSi and classic semiconductors are similar. *Physical Review Letters*, 78(14):2831–2834, April 1997.

[182] Z. Schlesinger, Z. Fisk, Hai-Tao Zhang, and M. B. Maple. Is FeSi a Kondo insulator? *Physica B*, 237-238:460–462, 1997.

[183] Shiro Funahashi, Kiyoaki Tanaka, and Fumitoshi Iga. X-ray atomic orbital analysis of 4f and 5d electron configuration of SmB_6 at 100, 165 and 298 K. *Acta Crystallographica Section B: Structural Science*, B66:292–306, March 2010.

[184] M. Neupane, N. Alidoust, S. Y. Xu, T. Kondo, Y. Ishida, D. J. Kim, Chang Liu, I. Belopolski, Y. J. Jo, T. R. Chang, H. T. Jeng, T. Durakiewicz, L. Balicas, H. Lin, A. Bansil, S. Shin, Z. Fisk, and M. Z. Hasan. Surface electronic structure of the topological Kondo-insulator candidate correlated electron system SmB_6. *Nature Communications*, (3991), December 2013.

[185] J. W. Allen, B. Batlogg, and P. Wachter. Large low-temperature Hall effect and resistivity in mixed-valent SmB_6. *Physical Review B*, 20(12):4807–4813, December 1979.

[186] D. J. Kim, S. Thomas, T. Grant, J. Botimer, Z. Fisk, and Jing Xia. Surface Hall effect and nonlocal transport in SmB_6: Evidence for surface conduction. *Nature Scientific Reports*, 3(3150), November 2013.

[187] Jonathan D. Denlinger, James W. Allen, Jeong-Soo Kang, Kai Sun, Byung-Il Min, Dae-Jeong Kim, and Zachary Fisk. SmB_6 photoemission: Past and present. *JPS Conference Proceedings*, 3(017038), 2014.

[188] R. L. Cohen, M. Eibschütz, and K. W. West. Electronic and magnetic structure of SmB_6. *Physical Review Letters*, 24(8):383–386, February 1970.

[189] S. Nozawa, T. Tsukamoto, K. Kanai, T. Haruna, S. Shin, and S. Kunii. Ultrahigh-resolution and angle-resolved photoemission study of SmB_6. *Journal of Physics and Chemistry of Solids*, 63:1223–1226, 2002.

[190] L. Jiao, S. Rößler, D. J. Kim, L. H. Tjeng, Z. Fisk, F. Steglich, and S. Wirth. Additional energy scale in SmB_6 at low-temperature. *Nature Communications*, 7(13762), December 2016.

[191] D. J. Kim, J. Xia, and Z. Fisk. Topological surface state in the Kondo insulator samarium hexaboride. *Nature Materials*, 13(3913):466–470, March 2014.

[192] Masashi Takigawa, Hiroshi Yasuoka, Yoshio Kitaoka, Takaho Tanaka, Hiroshi Nozaki, and Yoshio Ishizawa. NMR stsudy of a valence fluctuating compound SmB_6. *Journal of the Physical Society of Japan*, 50(8):2525–2532, August 1981.

[193] Maxim Dzero, Kai Sun, Victor Galitski, and Piers Coleman. Topological Kondo Insulators. *Physical Review Letters*, 104(106408), March 2010.

[194] N. Xu, P. K. Biswas, J. H. Dil, R. S. Dhaka, G. Landolt, S. Muff, C. E. Matt, X. Shi, N. C. Plumb, M. Radović, E. Pomjakushina, K. Conder, A. Amato, S. V. Borisenko, R. Yu, H. M. Weng, Z. Fang, X. Dai, J. Mesot, H. Ding, and M. Shi. Direct observation of the spin texture in SmB_6 as evidence of the topological Kondo insulator. *Nature Communications*, 5(4566), July 2014.

[195] E. Frantzeskakis, N. de Jong, B. Zwartsenberg, Y. K. Huang, Y. Pan, X. Zhang, J. X. Zhang, F. X. Zhang, L. H. Bao, O. Tegus, A. Varykhalov, A. de Visser, and M. S. Golden. Kondo Hybridisation and the origin of metallic states at the (001) surface of SmB_6. *Physical Review X*, 3(041024), December 2013.

[196] M. Takigawa, H. Yasuoka, T. Tanaka, Y. Ishizawa, M. Kasaya, and T. Kasuya. NMR study of mixed valent compounds SmB_6 with La and Yb substitution and CeB_6. *Journal of Magnetism and Magnetic Materials*, 31-34:391–392, 1983.

[197] O. Peña, M. Lysak, D. E. MacLaughlin, and Z. Fisk. Nuclear spin relaxation, hybridization and low-temperature 4f spin fluctuations in intermediate-valent SmB_6. *Solid State Communications*, 40(5):539–541, July 1981.

[198] Wei Ruan, Cun Ye, Minghua Guo, Fei Chen, Xianhui Chen, Guang-Ming Zhang, and Yayu Wang. Emergence of a coherent in-gap state in the SmB_6 Kondo insulator revealed by scanning tunneling spectroscopy. *Physical Review Letters*, 112(136401), April 2014.

[199] Bitan Roy, Jay D. Sau, Maxim Dzero, and Victor Galitski. Surface theory of a family of topological Kondo insulators. *Physical Review B*, 90(155314), 2014.

[200] Pier Paolo Baruselli and Matthias Vojta. Scanning tunneling spectroscopy and surface quasiparticle interference in models for the strongly correlated topological insulators SmB_6 and PuB_6. *Physical Review B*, 90(201106), November 2014.

[201] Rui Yu, Hongming Weng, Xiao Hu, Zhong Fang, and Xi Dai. Model Hamiltonian for topological Kondo insulator SmB_6. *New Journal of Physics*, 17(023012), February 2015.

[202] Feng Lu, JianZhou Zhao, Hongming Weng, Zhong Fang, and Xi Dai. Correlated topological insulators with mixed valence. *Physical Review Letters*, 110(096401), March 2013.

[203] J. Jiang, S. Li, T. Zhang, Z. Sun, F. Chen, Z. R. Ye, M. Xu, Q. Q. Ge, S. Y. Tan, X. H. Niu, M. Xia, B. P. Xie, Y. F. Li, X. H. Chen, H. H. Wen, and D. L. Feng.

Observation of possible topological in-gap surface states in the Kondo insulator SmB_6 by photoemission. *Nature Communications*, 4(3010), December 2013.

[204] Junwon Kim, Kyoo Kim, Chang-Jong Kang, Sooran Kim, Hong Chul Choi, J. S. Kang, J. D. Denlinger, and B. I. Min. Termination-dependent surface in-gap states in a potential mixed-valent topological insulator: SmB_6. *Physical Review B*, 90(075131), August 2014.

[205] Z. H. Zhu, A. Nicolaou, G. Levy, N. P. Butch, P. Syers, X. F. Wang, J. Paglione, G. A. Sawatzky, I. S. Elfimov, and A. Damascelli. Polarity-driven surface metallicity in SmB_6. *Physical Review Letters*, 111(216402), November 2013.

[206] G. Li, Z. Xiang, F. Yu, T. Asaba, B. Lawson, P. Cai, C. Tinsman, A. Berkley, S. Wolgast, Y. S. Eo, C. Kurdak Dae-Jeong Kim, J. W. Allen, K. Sun, X. H. Chen, Y. Y. Wang, Z. Fisk, and Lu Li. Two-dimensional Fermi surfaces in Kondo insulator SmB_6. *Science*, 346(6214):1208–1212, December 2014.